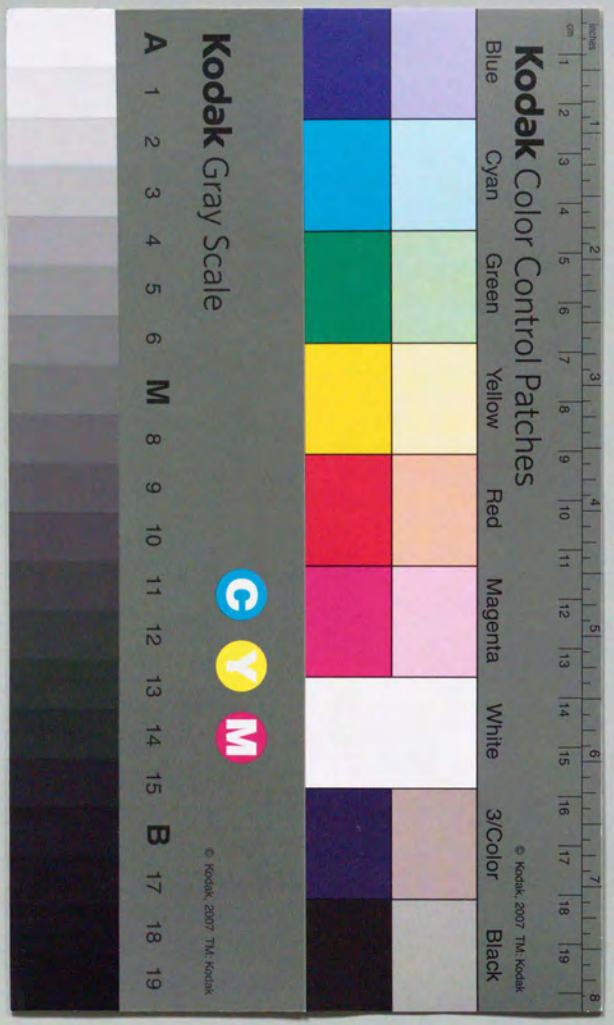

学 位 論 文

Top Quark Pair Production Near Threshold

(Threshold 近傍におけるトップ・クォーク対生成過程)

東京大学大学院理学系研究科

物理学専攻

隅 野 行 成

学 位 論 文

Top Quark Pair Production Near Threshold

（ Threshold 近傍におけるトップ・クォーク対生成過程 ）

東京大学大学院理学系研究科

物理学専攻

隅 野 行 成

Contents

Chapter 1

Introduction

1.1 Motivation

Recent results from the LEP precision experiments suggest that it is quite probable that the top quark exists in the mass range 100 GeV $< m_t <$ 200 GeV[1], which would be within the reach of the next generation e^+e^- colliders. The top quark pair production process in the threshold region is considered as one of the major subjects of the future e^+e^- colliders. It is expected that from the cross sections in the $t\bar{t}$ threshold region one may be able to extract the important physical parameters such as top mass m_t, strong coupling constant α_s, top decay width Γ_t, Higgs mass m_H, and top Yukawa coupling $g_{t\bar{t}H}$.

First quantitative analysis of the total cross section in the $t\bar{t}$ threshold region was performed by Fadin and Khoze in their pioneering papers[2], where they pointed out that the fairly stable theoretical prediction is available regarding the toponium resonance formations near $t\bar{t}$ threshold due to the large mass and the large decay width of top quark. The top quark width grows rapidly as m_t increases[3], and the dominant decay modes of toponium resonances will be almost saturated by the decay process of each constituent, $t \to bW$. Their key observation was that the large decay width of top quark would act as the infra-red cut-off, which prevents the theoretical uncertainties involved in the low energy QCD physics from affecting the theoretical predictions.

It is best illustrated by considering the $t\bar{t}$ pair produced in the e^+e^- annihila-

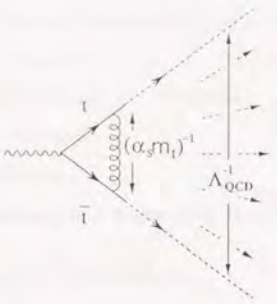

Figure 1.1: Top quark pair production near threshold. Top quark will decay before hadronization occurs.

tion as they spread apart from each other. (Fig. 1.1) Since they are slow near the threshold, they cannot escape even the relatively weak attractive force mediated by the exchange of Coulomb gluons, so that they are bound to form the Coulombic resonances when they reach the distance of Bohr radius $(\alpha_s m_t)^{-1} \sim 0.1$ GeV^{-1}. At this stage, the coupling of top quark to gluon is of the order of $\alpha_s(\mu = \alpha_s m_t) \sim 0.15$. If they could continue to spread apart even further to the distance $\Lambda_{QCD}^{-1} \sim$ a few GeV^{-1}, there would occur the hadronization effect as the coupling becomes really strong[4], since gluons with wave-length $\sim \Lambda_{QCD}^{-1}$ would be able to resolve the color charge of each constituent. For a realistic top quark, however, the $t\bar{t}$ pair will decay at the distance $(m_t\Gamma_t)^{-1/2} \sim 0.1$ GeV^{-1} into energetic b and $\bar{b}$ jets and W's before the hadronization effect becomes important. Here, the toponium can be regarded as the Coulombic resonance state (with reasonably weak coupling) due to the large mass and width of top quark. In this respect, the toponium resonances differ distinctly from the charmonium and bottomonium resonances[1] which have smaller masses as well as narrow widths. Besides, since the toponium resonances decay dominantly via the electroweak interaction, their decay process can also be calculated reliably.

[1]The spectra of charmonium and bottomonium resonances are dictated by the relatively low energy regime of the QCD interaction[5,6,7], and it is known that they can be fitted well by the logarithmic potential[8] phenomenologically.

Theoretically, the physics related to toponium resonance is interesting since this may be the first QCD bound state whose dynamics can be controlled starting from the first principles. Also, there exist remarkable interplays between electroweak and QCD interactions, which makes the study of toponium resonances unique. Experimentally, the $t\bar{t}$ threshold region may become one of the ideal places to extract the information on QCD, especially the strong coupling constant α_s. Moreover, since the effect of QCD interaction is now predictable over the entire threshold region, one may extract even smaller contributions such as Higgs effect. These observations triggered many of the recent works by several authors [9,10,11,12,13,14,15,16].

1.2 Quick Review of Related Works

As m_t becomes larger, the widths of the toponium resonances increase rapidly. The distinct resonance shape of the total cross section that would appear for the narrow resonances gets smeared for a heavy top quark, merging into a broad enhancement of the cross section over the threshold region for $m_t > 120$ GeV. Therefore, one is obliged to study the overall shape of the cross sections in the threshold region instead of applying the spectroscopic method developed at charmonium and bottomonium resonances.

The Green's function method introduced by Fadin and Khoze[2] enables the direct calculation of total cross section over the $t\bar{t}$ threshold region without recourse to the summation over the many resonances[9]. This method was improved by Strassler and Peskin[10], who made the close analyses of the threshold total cross section including the running of coupling constant α_s and also the effect of Higgs exchange. They showed that for a light top quark one may make an accurate measurement of the strong coupling constant α_s, while one may extract the mass and couplings of the Higgs boson for a heavy top quark. It was also argued that a precise measurement of top mass and a measurement of top width are possible for a wide range of m_t, 100 GeV $< m_t <$ 250 GeV.

The main defect in the measurement of the threshold total cross section for a heavy

top quark is that the resonance structures are quite smeared with the rapid growth of top width Γ_t, and that there is a strong correlation in the determination of α_s and m_t; it is difficult to tell whether m_t is small or α_s is large[11]. It was pointed out in Ref.[13] that the measurement of top quark momentum distribution in the threshold region would help determination of both α_s and m_t, since one may extract information on the QCD binding effect independent of that from the total cross section. There, the consistent analyses of total and differential cross sections were given by appropriately incorporating the phase space volume of the final bW's. The differential cross sections near threshold were also studied by Ježabek, Kühn and Teubner[14]. They focused on the energy distributions of W's, which would escape from the interaction region as the color neutral particles. They found that the W's spectra can also be useful in the measurement of α_s and m_t.

Another attempt at the measurement of α_s for a relatively heavy top quark was proposed in Ref.[16], where the effect of $t\bar{t}Z^0$ axial-vector coupling on the $t\bar{t}$ pair production process was studied. P-wave resonance states produced via axial-coupling interfere with the S-wave states due to the large top quark width. This interference gives rise to the forward-backward (FB) asymmetry below threshold which grows as m_t is increased. Its α_s-dependence is magnified simultaneously so that the measurement of FB-asymmetry may help determination of α_s for $m_t > 150$ GeV. The FB-asymmetry 'measures' the degree of overlap of S-wave and P-wave states. The key point here is that the top quark width and the energy differences of the resonance levels have the same order of magnitude.

More realistic studies, based on the above works, have been given in the thorough analyses of the cross sections near $t\bar{t}$ threshold, as one of the major subjects in the next generation e^+e^- linear collider projects[15,17,18]. It has been confirmed by the recent analyses, on the basis of Monte Carlo simulations including experimental parameters[18], that indeed there is a strong possibility for the accurate measurements of the basic parameters (α_s, m_t, Γ_t,...) in the real life experiments using the total and differential

cross sections as well as the FB-asymmetry near $t\bar{t}$ threshold.

1.3 Aim of the Thesis

In this thesis, we report the studies of the cross sections and the underlying physics for the $t\bar{t}$ pair production process at e^+e^- collision in the threshold region. Here, we constrain ourselves within the studies based on the Standard Model. We include all the QCD corrections up to the next-to-leading order in our analyses, and develop the necessary theoretical framework for the calculations. These are the studies done by the present author (with co-workers), part of which is completely new, while other parts are the re-analyses of his previous works[13,16] by including the full next-to-leading order corrections.

To provide reliable theoretical predictions of the total and differential cross sections in the threshold region, it is desirable to include next-to-leading order corrections to the cross sections. Some of them are already included in the preceding analyses. The leading order terms near threshold are identified with the Coulomb singularities (threshold singularities), where all the order $(\alpha_s/\beta)^n$ are summed up[19,5], with $\beta \simeq |\mathrm{p}_t|/m_t$. The next-to-leading order corrections are the terms α_s^{n+1}/β^n, which can be regarded as the $O(\alpha_s)$, or equivalently, $O(\beta)$ corrections to the leading order terms, since $\alpha_s^{n+1}/\beta^n = \alpha_s(\alpha_s/\beta)^n = \beta(\alpha_s/\beta)^{n+1}$. Thus, the next-to-leading order corrections are expected to give order 10% corrections to the cross sections, and it is important to establish the full theoretical prediction to this order with regard to the future experiments.

The following respects of the present thesis are new. We provide a solid theoretical framework necessary for the $O(\alpha_s)$ calculations of the threshold cross sections in detail. Accoding to the formalism, we include in the cross sections the contributions from the final state interaction diagrams as the new corrections at $O(\alpha_s)$. We find that these corrections give non-trivial modifications to the top quark differential cross sections. It turns out, however, that the corrections from the final state interaction diagrams cancel out altogether in the total cross section at the next-to-leading order. This result justifies

the previous analyses of the total cross section given in Ref.[15] up to this order, which included the $O(\alpha_s)$ corrections to the top quark width Γ_t and to the QCD potential $V_{QCD}(r)$ as well as the hard gluon correction to the $t\bar{t}V$ ($V = \gamma$ or Z^0) vertex.

This thesis also includes the re-analyses of the cross sections and the related physics, which were performed by the present author with co-workers in Refs.[13,16], by incorporating the full next-to-leading order corrections. These results, together with the necessary theoretical framework, are now in preparation for the publication in collaboration with K. Hikasa and S. Ishihara.

The main achievements of the present author (with collaborators), which are contained in this thesis, can be summarized as follows:

(1) We provided the consistent analyses of total and differential cross section near $t\bar{t}$ threshold region, in which the phase space volume of the final bW's are appropriately taken into account. We found that the measurement of the differential cross section would be useful in the determination of α_s and m_t; in Ref.[13].

(2) We found that there appears measurable forward-backward asymmetry[2] even below threshold for a relatively heavy top quark, due to the interference of the S-wave and P-wave resonances with the rapid growth of top quark width. The sensitivity to α_s increases with m_t so that the measurement of FB-asymmetry may help determination of α_s for a relatively heavy top quark; in Ref.[16]

(3) We re-calculate the total and differential cross sections as well as forward-backward asymmetry including the full next-to-leading order corrections. It is found that the corrections from the final state interaction diagrams modifies the shape of differential cross sections non-trivially at $O(\alpha_s)$, while these contributions cancel out in the total cross section. Also, we provide a solid theoretical framework necessary for the calculations; in collaboration with K. Hikasa and S. Ishihara.

[2]This is another $O(\alpha_s) = O(\beta)$ correction to the $t\bar{t}$ threshold cross section first introduced by the present author.

1.4 Organization of the Thesis

In the following chapters, we pay special attention to the two specific points. Namely, (1)we make efforts to understand the underlying physics that governs the main structures of the cross sections; it helps to identify the observables that allow determination of the basic parameters of Standard Model, α_s and m_t, and (2)we try to provide a solid theoretical basis necessary for the calculations of the full next-to-leading order corrections in the threshold region, where the naive perturbation theory breaks down.

In Chapter 2, we start with an intuitive illustration of the space-time evolution of the $t\bar{t}$ pair produced in the threshold region, which subsequently decay into bW's. We provide the theoretical framework for including the $O(\alpha_s)$ corrections in Chapter 3. The first part (Section 3.1) of this chapter prepares the introductory theoretical concept for treating the threshold resonance states. We identify the presence of the gauge-invariant threshold singularities in the Feynman diagrams up to all orders in α_s, and clarify the relevant kinematical configurations of the top-pair plus gluons in the formation of toponium resonances. It is also demonstrated explicitly that the large top quark width acts as the infra-red cut-off of the momentum carried by the gluon. The second part (Section 3.2) concerns the determination of the S-matrix element as well as the differential cross sections for the process $e^+e^- \to bW^+\bar{b}W^-(g)$ including the next-to-leading order corrections. This is achieved step by step on the basis of the general formalism of the heavy threshold bound states.

In Chapter 4, the cross sections in the threshold region are examined in detail. We elucidate the underlying physics in order to identify the observables that can be extracted from the cross sections. We first summarize the necessary formulas of the cross sections in Section 4.1. The total cross section and the top quark momentum distribution are examined in Section 4.2. We find that both cross sections are sensitive to α_s. We investigate the asymmetric distribution of top quark, proportional to $\cos\theta$, and the forward-backward asymmetry in Section 4.3. It is argued that the measurement of the forward-backward asymmetry may help determination of α_s for a relatively heavy

top quark.

We study the effects of the $O(\alpha_s)$ corrections in Chapter 5. The contribution from the each source of $O(\alpha_s)$ correction is examined separately. We see that the final state interactions give non-trivial corrections to the differential cross sections. It is found, however, the correction vanishes in the total cross section.

The discussion is given in Chapter 6. We estimate the corrections to the cross sections which have not been included in this work (Section 6.1). Also, we discuss a possible source of the modification to the QCD potential used in our analyses (Section 6.2). The concluding remarks are given in Chapter 7.

The details of the theoretical ingredients are contained in the Appendices. We present the general framework of the threshold bound states in Appendix A. The power counting method, which proves to be an important tool for identifying the singularities in the diagrams, is explained fully in Appendix B. In Appendix C, we give the details of the two-loop improved QCD potential used in our numerical studies. An example of explicit calculation of absorptive potential is presented in Appendix D.

Chapter 2

Physical Picture

In this chapter we present an intuitive picture of the physics in the $t\bar{t}$ threshold region. We give a qualitative description of the space-time evolution of the toponium system using the uncertainty relation. It is emphasized that this system probes the perturbative regime of QCD interaction due to the large mass and width of the top quark.

We are concerned with the process where t and $\bar{t}$ are pair created and subsequently decay into bW's (see Fig. 2.1):

$$e^+e^- \to \gamma, Z \to t\bar{t}(\text{“}\Theta\text{”}) \to (bW^+)(\bar{b}W^-). \tag{2.0.1}$$

Annihilation of the $t\bar{t}$ pair is found to be negligible for $m_t \gtrsim 100$ GeV [20,21]. We would like to treat the production and decays of $t\bar{t}$ in the lowest order of the electroweak theory while keeping the QCD interactions between the $t\bar{t}$ state. This is achieved formally by splitting the Lagrangean into two parts

$$\mathcal{L} = \mathcal{L}_0 + \mathcal{L}_{\rm EW}, \tag{2.0.2}$$

where $\mathcal{L}_0$ contains the strong interaction, and by treating the electroweak interactions $\mathcal{L}_{\rm EW}$ perturbatively.

The non-trivial and interesting part of the process is contained in the three-point Green's function

$$K_{\alpha\beta\gamma\delta}(x,y,z) \;=\; \langle 0 \,|\, T\,\psi_\alpha(x)\,\bar{\psi}_\beta(y) : \bar{\psi}_\gamma(z)\psi_\delta(z) : |\, 0 \,\rangle\,, \tag{2.0.3}$$

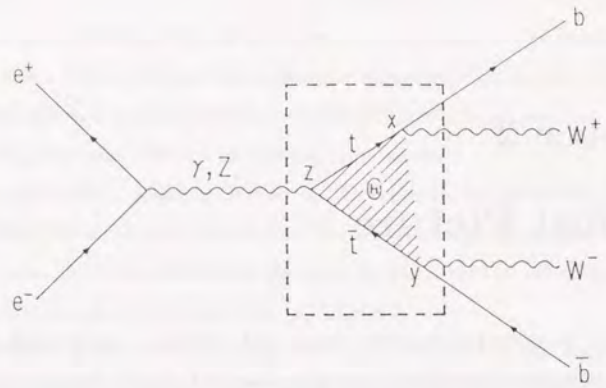

Figure 2.1: The diagram for the $t\bar{t}$ pair production process and their subsequent decays into bW's. The box with the dashed line shows the three-point function $K(x,y,z)$ that carries the information of the toponium resonances.

which expresses the amplitude where a $t\bar{t}$ pair is created at a space-time point z and the t ($\bar{t}$) quark decays at another point x (y), see Fig. 2.1. This three-point function contains the effect of full QCD interactions, in the absence of which it reduces to the product of t and $\bar{t}$ free propagators. Since the created t and $\bar{t}$ will have small velocities near the threshold, the system related to this Green's function is regarded as a non-relativistic t and $\bar{t}$ system which is bound by the static potential $V(|\mathbf{r}_1-\mathbf{r}_2|)$ to form the toponium resonances. We can then use the non-relativistic Schrödinger equation to estimate the effect of the non-perturbative strong interactions. (See Section 3.1 for the theoretical foundation.) It is expected that the process probes the short distance behavior of the potential due to the large t-quark mass.

The main contribution to the potential $V(r)$ comes from the QCD interaction. At short distances $r \ll \Lambda_{QCD}^{-1}$, the perturbative picture of one-gluon exchange becomes

valid, and hence $V(r)$ behaves like the Coulomb potential near the origin:

$$V(r) \sim -C_F \frac{\alpha_s}{r}, \tag{2.0.4}$$

with the color factor $C_F = 4/3$. We note therefore that there are 3 typical time scales in this system, namely

$$\Gamma_\Theta^{-1} \qquad \text{toponium lifetime,} \tag{2.0.5}$$

$$a_0 = (\alpha_s m_t)^{-1} \qquad \text{Bohr radius,} \tag{2.0.6}$$

$$a_0/\alpha_s \qquad (\text{Coulomb level})^{-1}. \tag{2.0.7}$$

Here, according to the Standard Model, the decay widths of resonances, Γ_Θ, are almost saturated by the widths of t and $\bar{t}$, so that $\Gamma_\Theta \simeq 2\Gamma_t$[2,10].

Let us first examine the time evolution of the system in the case where $\Gamma_\Theta^{-1} \gg a_0/\alpha_s \gg a_0$. Suppose that at $t = 0$, a $t\bar{t}$ pair is created at the space point $\mathbf{x} = 0$ (see Fig. 2.2). At this moment, the wave packet of the $t\bar{t}$ system is like a δ function (with the size of $\sim 1/m_t$) at the origin, which is the superposition of all plane waves with an equal weight:

$$\psi(\mathbf{x})\Big|_{t=0} \simeq \delta^3(\mathbf{x}) = \int \frac{d^3\mathbf{p}}{(2\pi)^3}\, e^{i\mathbf{p}\cdot\mathbf{x}-iEt}\Big|_{t=0}. \tag{2.0.8}$$

All the plane waves quickly spread outwards from the origin $\mathbf{x} = 0$. Each plane wave spreads until it reaches the potential barrier at a distance of the Bohr radius. It is then bounced back and starts oscillating within the potential wall. The fastest wave (we are concerned with the group velocity here) will reach the barrier at the time $t = a_0$ ($|\mathbf{p}| = \infty$). Lower momentum waves will reach there successively. It is from the time $t \sim a_0/\alpha_s$, when the typical waves related to the bound states reach the barrier, that the concept of various resonance states becomes meaningful. We may then say that the toponium is formed. The velocity of the typical wave is equal to α_s, which is a familiar picture for the Coulomb potential problem. These resonance states will remain until the t or $\bar{t}$ quark decays at the time scale Γ_Θ^{-1}. The waves that have momentum less than Γ_Θ/α_s will never reach the potential wall.

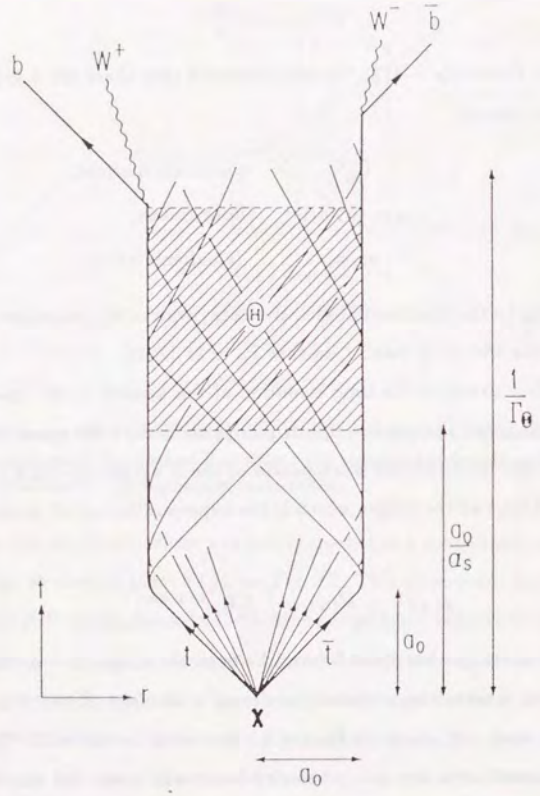

Figure 2.2: A figure that shows the time evolution of the non-relativistic $t\bar{t}$ system.

More realistically, the attractive potential between t and $\bar{t}$ deviates from the Coulombic potential due to the running of the coupling constant α_s. Roughly, the QCD potential is given by the Coulomb potential with running coupling constant evaluated at momentum scale $\mu \sim 1/r$:

$$V(r) \sim -C_F \frac{\alpha_s(1/r)}{r}. \tag{2.0.9}$$

The toponium resonances feel the attractive force corresponding to the coupling $\alpha_s(\mu)$ evaluated at the size of their wave functions, typically $\mu \sim \alpha_s m_t \sim$ (Bohr radius)$^{-1}$. As top is heavy, its typical kinetic energy inside the bound state far exceeds that of quarks inside the lighter quarkonia. Therefore, top quark can probe the deep region of the QCD potential.

For the current theoretical expectation of the top mass, $m_t \sim 100$ to 200 GeV, the lifetime of toponium and the time scale for resonance formation are of the same order of magnitude,

$$\Gamma_\Theta^{-1} \sim a_0/\alpha_s \sim O(1\,\mathrm{GeV}). \tag{2.0.10}$$

It is then expected from the above picture that this system will probe the QCD potential since

$$\Gamma_\Theta^{-1} \gg a_0, \tag{2.0.11}$$

so that the waves oscillate a considerable number of times within the potential barrier before the decay occurs. Also, because

$$\Gamma_\Theta^{-1} \lesssim \Lambda_{QCD}^{-1}, \tag{2.0.12}$$

t and $\bar{t}$ quarks decay via the electroweak interaction before the hadronization effect becomes significant [22,23]. Lower momentum waves with $|\mathbf{p}| \lesssim \Gamma_\Theta/\alpha_s$ do not feel the QCD potential. Thus, we are free from the uncertainties coming from non-perturbative QCD at long distances. We have confirmed the observation[10] that indeed the total cross section is quite insensitive to the long distance behavior of $V(r)$ near the threshold. See Section 4.2.

The characteristic features may be summarized as follows. High momentum waves with $|\mathbf{p}| > \Gamma_\Theta/\alpha_s \sim 1/a_0$ reach the potential wall before the top decay, and the $t\bar{t}$ production cross section will be affected by the toponium resonance formation. On the other hand, the lower momentum waves with $|\mathbf{p}| < \Gamma_\Theta/\alpha_s$ do not reach the potential wall, and the details of the multiple resonance structure that is predicted for the stable top quark will be smeared out. We are no longer able to resort to the spectroscopy to determine the form of $V(r)$ but rather we are concerned with the overall shape of the cross sections in the threshold region. It is necessary therefore to consider the interplay among the various resonance states.

Chapter 3

Theory

It has long been a challenge to describe the dynamics of QCD bound states from the first principles. Toponium resonance states may become the first such candidates due to their unique charateristics. The resonances can be understood as the bound system of $t\bar{t}$ pair plus gluons where the typical momenta of gluons are relatively large. We try to provide a solid theoretical basis to deal with the toponium resonances that serves for the quantitative studies given in the following chapters. In section 3.1 we review the introductory theoretical concept regarding the toponium resonances. Then we determine the S-matrix element and the cross sections for the process $e^+e^- \to bW^+\bar{b}W^-(g)$ including the full $O(\alpha_s)$ corrections near threshold in Section 3.2.

3.1 Basic Concept

In this section we explain the basic concept underlying the present work. Fairly stable theoretical prediction is available regarding the toponium resonances due to the large mass and large decay width of top quark, and also because the resonance formation involves the spacelike region of gluon momentum. Here, we will translate the physical intuition into the theoretical language. Characteristic properties of toponium states will be clarified by the explicit reference to the relevant kinematical configuration of top-pair plus gluon system in the formation of resonances.

3.1.a Leading Threshold Singularities

It is well-known that near the threshold of quark-antiquark ($q\bar{q}$) pair production, the naive perturbation theory breaks down due to the formation of bound states [24,5], and the strong interaction is enhanced accordingly. Intuitively, this is because the produced q and $\bar{q}$ have small velocities so that they are trapped by the attractive force mediated by the exchange of gluons. We will briefly review this property near $t\bar{t}$ threshold. We demonstrate explicitly that the ladder diagrams exhibit the gauge invariant leading singularities. In this subsection, we neglect the decay of t and $\bar{t}$, and treat them as stable particles. The effect of their decay widths will be considered in the next subsection.

Let us consider the amplitude where a virtual photon decays into t and $\bar{t}$, $\gamma^* \to t\bar{t}$, just above the threshold of $t\bar{t}$ pair production. As we will see below, the ladder diagram for this process where uncrossed gluons are exchanged n times between t and $\bar{t}$ has the behavior $\sim (\alpha_s/\beta)^n$, see Fig. 3.1. Here, β is the velocity of t or $\bar{t}$ in the c.m. frame,

$$\beta = \sqrt{1 - \frac{4m_t^2}{s}}. \tag{3.1.1}$$

Hence, the contribution of the n-th ladder diagram will not be small even for large n if $\beta \lesssim \alpha_s$. That is, the higher order terms in α_s remain unsuppressed in the threshold region. The singularities which appear at this specific kinematical configuration is known as "threshold singularities".[1]

We may observe the appearance of $\sim (\alpha_s/\beta)^n$ in the n-th ladder diagram as follows.

First, consider the one-loop diagram. Its *imaginary* part can be estimated using the Cutkosky rule (cut-diagram method), see Fig. 3.2. Namely, the imaginary part is given by the phase space integration of the product of the tree diagrams. The intermediate $t\bar{t}$ phase space is proportional to β as

$$d\Phi_2(t\bar{t}) = \frac{\beta}{16\pi}\, d\cos\theta, \tag{3.1.2}$$

[1]This singularity stems from the fact that, for a particular assignment of the loop momenta, all the internal particles can become very nearly on-shell simultaneously as $\beta \to 0$.

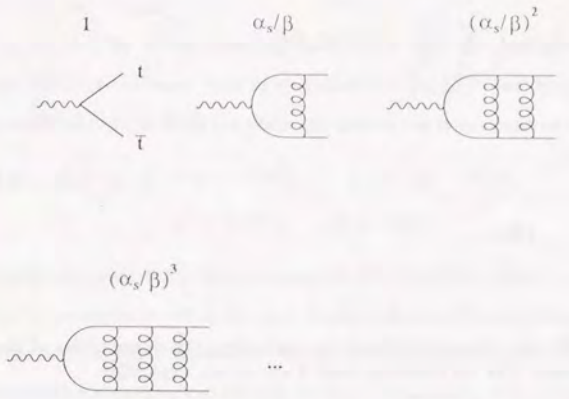

Figure 3.1: The ladder diagrams for the process $\gamma^* \to t\bar{t}$. The diagram where n uncrossed gluons are exchanged has the behavior $\sim (\alpha_s/\beta)^n$ near threshold.

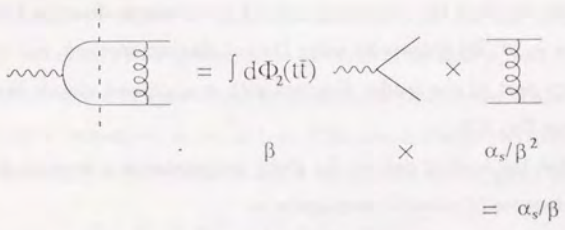

Figure 3.2: The Cutkosky rule for evaluating the imaginary part of the 1-loop diagram. The factors in α_s and β are shown explicitly.

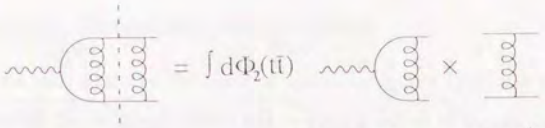

Figure 3.3: The cut-diagram method for evaluating the singularities of the higher order ladder diagrams. The factors in α_s and β are shown explicitly.

where θ is the angle between the momenta of the intermediate top quark and the final top quark in the c.m. frame. Meanwhile the $t\bar{t}$ scattering diagram with t-channel gluon exchange contributes the factor $\sim \alpha_s/\beta^2$ since the gluon propagator is proportional to $1/\beta^2$. In fact the propagator denominator is given by

$$k^2 = -\mathbf{k}^2 = -\frac{s\beta^2}{2}(1-\cos\theta), \tag{3.1.3}$$

where k denotes the gluon momentum.

Thus, we see that the imaginary part of the one-loop diagram has the behavior $\sim \beta \cdot \alpha_s/\beta^2 = \alpha_s/\beta$. By repeatedly using the cut-diagram method, one can induce that the imaginary part of the ladder diagram with n uncrossed gluons has the behavior $\sim (\alpha_s/\beta)^n$, see Fig. 3.3.

Note that the leading part of the gluon propagator in powers of β (in R_ξ-gauge) is the instantaneous (Coulomb) propagator as

$$\bar{u}_f\gamma^\mu u_I \frac{-i}{k^2+i\epsilon}\left[g_{\mu\nu}-(1-\xi)\frac{k_\mu k_\nu}{k^2}\right]\bar{v}_I\gamma^\nu v_f$$
$$\rightarrow \bar{u}_f\gamma^0 u_I \frac{-i}{-\mathbf{k}^2+i\epsilon}\bar{v}_I\gamma^0 v_f. \tag{3.1.4}$$

Here, the subscripts f and I stand for the final state and the intermediate state, respectively. We used the fact that the space components of the currents, $\bar{u}_f\gamma^\mu u_I$ and $\bar{v}_I\gamma^\nu v_f$,

are order β in the c.m. frame.[2]

It can be checked by power counting method[25] that the *real* part of the n-th ladder diagram exhibits the same type of singularity, $\sim (\alpha_s/\beta)^n$, see Appendix B. The relevant loop momenta in the loop integrals are also in the non-relativistic regime:

$$p_t^0 - m_t,\ \bar{p}_t^0 - m_t \sim O(\beta^2), \qquad \mathbf{p}_t = -\bar{\mathbf{p}}_t \sim O(\beta), \tag{3.1.5}$$
$$k^0 \sim O(\beta^2), \qquad \mathbf{k} \sim O(\beta). \tag{3.1.6}$$

Here, p_t, $\bar{p}_t$ and k represent the internal momenta of t, $\bar{t}$ and the gluon, respectively, in the c.m. frame. It is easy to see that, for such configurations, $t(\bar{t})$ and gluon propagators are counted as $\sim 1/\beta^2$, and the measure for the each loop integration $d^4k/(2\pi)^4$ as $\sim \beta^5$.[3]

Thus, the ladder diagrams exhibit the leading singularities $\sim (\alpha_s/\beta)^n$. As shown in Appendix B, other diagrams, including crossed gluon diagrams, do not exhibit the leading singularities, but contribute to the non-leading singularities $\sim \alpha_s^{n+l}/\beta^n$ $(l \geq 1)$.

One may worry about the gauge invariance of the amplitude if we take only the ladder diagrams. Let us write the amplitude for the process $e^+e^- \rightarrow t\bar{t}$ with full QCD corrections near threshold as

$$M^{(full)}(\alpha_s,\beta) = \sum_n c_n(\alpha_s/\beta)^n + (\text{non-leading terms}). \tag{3.1.7}$$

Then the coefficients c_n's should be gauge-independent since the full QCD amplitude $M^{(full)}$ is gauge invariant. (We suppressed the variables other than α_s and β.) Explicitly, the gauge-independence of c_n's is ensured by the gauge-independence of the leading part $\sim 1/\beta^2$ of the gluon propagator in eq. (3.1.4). This also holds for the momenta (3.1.5) and (3.1.6) if we note that the off-shell t and $\bar{t}$ wave functions are given by

$$\not{p}_t + m_t = m_t(1+\gamma^0) - p_t^i\gamma^i + O(\beta^2), \tag{3.1.8}$$

[2]Dirac representation of the γ-matrices is most useful in understanding the power count, where γ^0 is diagonal and γ^i's are off-diagonal. The t-quark spinor wave function has the upper two components with order of unity and the lower two components suppressed by β, and vice versa for the $\bar{t}$-quark.

[3]In general, in counting the powers of β of a loop integral, the singularity of the integrand will be increased if one assigns large powers of β to the propagator denominators of the internal particles, but, at the same time, the integration measure will be more suppressed. The optimal assignment of the order in β to each internal momentum which exhibits the most singular part is given in eqs. (3.1.5) and (3.1.6).

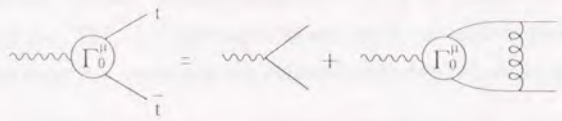

Figure 3.4: The self-consistent equation satisfied by the leading singularities of the $t\bar{t}\gamma$ vertex Γ_0^μ. One should take only the leading part $\sim (\alpha_s/\beta)^n$ on both sides of the equation.

$$-\not{p}_t + m_t = m_t(1-\gamma^0) + \not{p}_t^i\gamma^i + O(\beta^2). \tag{3.1.9}$$

As the higher order terms in α_s can no longer be neglected near threshold, we are led to sum over the leading threshold singularities. Let us denote by Γ_0^μ the leading singularities of the vertex $\gamma^* \to t\bar{t}$, which satisfies the self-consistent equation as depicted in Fig. 3.4. By taking only the leading part $\sim (\alpha_s/\beta)^n$ on both sides of the equation, one obtains[10] the vertex Γ_0^μ as

$$\Gamma_0^\mu = -\left(\frac{1+\gamma^0}{2}\gamma^\mu\frac{1-\gamma^0}{2}\right)(E - \mathrm{p}_t^2/m_t)\,\tilde{G}_0(\mathrm{p}_t; E), \tag{3.1.10}$$

where $E = \sqrt{s} - 2m_t$ is the energy measured from the threshold. $\tilde{G}_0(\mathrm{p}; E)$ is the S-wave Green's function of the non-relativistic Schrödinger equation with Coulomb potential:

$$\left[\left(-\frac{\nabla^2}{m_t} + V(r)\right) - (E + i\epsilon)\right] G_0(\mathrm{x}; E) = \delta^3(\mathrm{x}), \tag{3.1.11}$$

$$\tilde{G}_0(\mathrm{p}; E) = \int d^3\mathrm{x}\, e^{-i\mathrm{p}\cdot\mathrm{x}}\, G_0(\mathrm{x}; E), \tag{3.1.12}$$

$$V(r) = -C_F\frac{\alpha_s}{r}, \tag{3.1.13}$$

where $C_F = 4/3$ is the color factor. The analytic expression of the total cross section evaluated with $G_0(\mathrm{x}; E)$ is available (see, for example, Ref.[2] for the toponium), which includes the resonance spectra below threshold, $E < 0$. Explicitly, we may write

$$\tilde{G}_0(\mathrm{p}; E) = -\sum_n \frac{\phi_n(\mathrm{p})\psi_n^*(\mathbf{0})}{E - E_n + i\epsilon}, \tag{3.1.14}$$

where $\phi_n(\mathrm{p})$ and $\psi_n(\mathrm{x})$ are the Coulomb wave functions in momentum space and coordinate space, respectively. Here, n includes the bound states, $E_n = -(C_F\alpha_s)^2 m_t/4n^2$, and continuum states for $E_n > 0$. Only the S-wave states contribute to the leading vertex as seen from the appearance of $\psi_n(\mathbf{0})$.[4]

As for the amplitude for $e^+e^- \to t\bar{t}$ near threshold, one may take the leading singularities $\Gamma_0^\mu = \sum c_n^{(0)}(\alpha_s^n/\beta^n)$ as the zeroth order of the new perturbative expansion,[5] and consider $\Gamma_1^\mu = \sum c_n^{(1)}(\alpha_s^{n+1}/\beta^n)$, $\Gamma_2^\mu = \sum c_n^{(2)}(\alpha_s^{n+2}/\beta^n)$, ..., as the higher order corrections. They are gauge invariant at each order. One may regard Γ_1^μ as $O(\alpha_s)$ or $O(\beta)$ correction to the zeroth order Γ_0^μ, since $\alpha_s^{n+1}/\beta^n = \alpha_s(\alpha_s/\beta)^n = \beta(\alpha_s/\beta)^{n+1}$. Note that the expansion parameter β is guaranteed to be small if α_s is small, since we are interested in the summation of the leading singularities only in the kinematical region where the naive perturbation theory breaks down ($\beta \lesssim \alpha_s$).

Near the $t\bar{t}$ threshold, α_s will be order 10% , and the above new expansion will be justifiable. It is important to include the $O(\alpha_s) = O(\beta)$ corrections to the cross sections for practical purposes.

Matching of the total cross section calculated using $\Gamma_0^\mu + \Gamma_1^\mu$ (valid near threshold) and that calculated using the one-loop perturbative QCD (valid at $\beta \gg \alpha_s$) in the intermediate region $\beta \sim \alpha_s$ has been examined [9,15].

3.1.b Top Quark Width as the Infra-red Cut-Off

The discussion of the leading threshold singularities in the previous subsection is identical to that of QED bound states such as positronium. In QCD, however, one would expect additional non-perturbative effects arising from the infra-red region along with the formation of bound states[5]. Fadin and Khoze pointed out[2] that, in contrast to charmonium and bottomonium, the large decay widths of toponium resonances would act as the infra-red cut-off, which prevent the theoretical ambiguities connected with the infra-red region from coming into play. We see in this subsection that the gluon

[4] To see that $(E - \mathrm{p}^2/m_t)\tilde{G}_0(\mathrm{p}; E)$ is a function of α_s/β, one should identify $E \to m_t\beta^2$ and $|\mathrm{p}| \to m_t\beta$ in the leading order.

[5] At the zeroth order no ultra-violet divergence is involved.

momentum is effectively cut off well above the hadronization scale.

Intuitively, the $t\bar{t}$ pair created at some space-time point feels the interaction potential between t and $\bar{t}$ as they spread apart, but decay via the electroweak process before searching the long distance behavior of the potential [13], or, before the hadronization effects become significant. The b-quarks produced in the decay are very energetic, and we may apply perturbative QCD for the decay process[4,26].

Let us first state the problem of low energy QCD that would emerge for a stable top quark. As seen in eq. (3.1.3), the typical gluon momentum scale involved in the formation of bound states is $k^2 \sim -2m_t^2\beta^2$. It may even become zero at the threshold, $s = 4m_t^2$. One may infer the catastrophe in the calculation of the amplitude. Although counted as sub-leading in terms of threshold singularities, higher order contributions such as $\sim [\alpha_s \log(-k^2/\mu^2)]^n$, which typically originate from the gluon vacuum polarization diagrams, would sum up to give the amplitude behavior

$$\frac{1}{\log(-k^2/\Lambda_{QCD}^2)} \sim \frac{1}{\log(2m_t^2\beta^2/\Lambda_{QCD}^2)}. \tag{3.1.15}$$

The above expression will be valid for $-k^2 \gg \Lambda_{QCD}^2$, while the singular behavior in the region $-k^2 \lesssim \Lambda_{QCD}^2$ is the sign of breakdown of the theoretical prediction. No rigid theoretical control is available in this region up to today.

Now we are in place to examine the effect of top quark width Γ_t. Again consider the one-loop diagram in Fig. 3.5:

$$\mathcal{M}^\mu = -iC_F \int \frac{d^4q}{(2\pi)^4} \gamma^\alpha S_F(P/2+q)\gamma^\mu S_F(-P/2+q)\gamma_\alpha \frac{4\pi\alpha_s((q-p)^2)}{(q-p)^2+i\epsilon} \tag{3.1.16}$$

Here, S_F denotes the top quark propagator. In order to include the higher order contributions effectively, we used the running coupling constant $\alpha_s(k^2)$ at the $t\bar{t}g$ vertex. It is understood that t and $\bar{t}$ finally decay into bW's. Had we used the free top quark propagator for S_F, we would have

$$\mathcal{M}_{free}^\mu(m_t^2, m_t^2) \sim \frac{\alpha_s(-2m_t^2\beta^2)}{\beta} \sim \frac{1}{\beta \log(2m_t^2\beta^2/\Lambda_{QCD}^2)}. \tag{3.1.17}$$

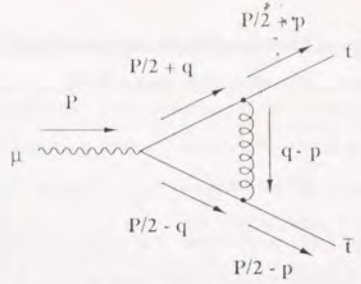

Figure 3.5: The one-loop ladder diagram for $\gamma^* \to t\bar{t}$. It is understood that the t and $\bar{t}$ subsequently decay into bW's. In order to include the higher order contributions effectively, we use the running coupling constant $\alpha_s(k^2)$ at the $t\bar{t}g$ vertex.

The formulation including unstable particles was developed by Veltman [27]. We follow his prescription and use the full propagator for S_F, which has the spectral representation

$$S_F(p) = \int_0^\infty d\mu^2 \left[\rho_1(\mu^2)\,\not{p} + \rho_2(\mu^2)\mu\right] \frac{i}{p^2 - \mu^2 + i\epsilon}. \tag{3.1.18}$$

(We neglect the parity odd interaction, for simplicity.) Near the top quark pole, $\mu^2 \simeq m_t^2$, the spectral functions have the Breit-Wigner shape as

$$\begin{aligned}\rho_1(\mu^2), \rho_2(\mu^2) &\simeq \frac{1}{\pi} \frac{m_t\Gamma_t}{(\mu^2 - m_t^2)^2 + m_t^2\Gamma_t^2} \\ &= \frac{1}{2\pi i}\left[\frac{1}{\mu^2 - m_t^2 - im_t\Gamma_t} - \frac{1}{\mu^2 - m_t^2 + im_t\Gamma_t}\right].\end{aligned} \tag{3.1.19}$$

Substituting (3.1.18) and (3.1.19) into (3.1.16), we have

$$\begin{aligned}\mathcal{M}^\mu \simeq \int_0^\infty d\mu^2 \int_0^\infty d\bar{\mu}^2 \, \frac{1}{\pi} \frac{m_t\Gamma_t}{(\mu^2 - m_t^2)^2 + m_t^2\Gamma_t^2} \cdot \frac{1}{\pi} \frac{m_t\Gamma_t}{(\bar{\mu}^2 - m_t^2)^2 + m_t^2\Gamma_t^2} \\ \times \mathcal{M}_{free}^\mu(\mu^2, \bar{\mu}^2).\end{aligned} \tag{3.1.20}$$

Since integrations $\int_0^\infty d\mu^2 \int_0^\infty d\bar{\mu}^2$ are essentially the Cauchy integral, the result is merely to replace μ^2 and $\bar{\mu}^2$ by $m_t^2 - im_t\Gamma_t$:

$$\mathcal{M}^\mu \simeq \mathcal{M}_{free}^\mu(m_t^2 - im_t\Gamma_t, m_t^2 - im_t\Gamma_t). \tag{3.1.21}$$

This results in effectively changing β to a complex variable in eq. (3.1.1). In particular, now β never crosses zero for any value of s. One sees that the gluon momentum scale is cut off as

$$|k^2| \gtrsim 2m_t\Gamma_t, \tag{3.1.22}$$

and the singular behavior in (3.1.17) is avoided. For instance, $\sqrt{2m_t\Gamma_t} \simeq 4$ GeV for $m_t = 100$ GeV, and $\sqrt{2m_t\Gamma_t} \simeq 30$ GeV for $m_t = 200$ GeV. This is just about the inverse of the distance t-quark travels before it decays.

The above discussion parallels closely that by Poggio, Quinn and Weinberg[28]. It has been checked numerically that indeed theoretical predictions are quite insensitive to the long distance behavior of the QCD potential $V(r)$ [10,13,15,16]. We will demonstrate it explicitly in Chapter 4 in the threshold total cross section.

Similarly, one may argue that the gluon momentum scale in the top quark self-energy diagrams is also cut off, $|k^2| \gtrsim m_t\Gamma_t$. Writing the full top propagator as

$$S_F(p) = \frac{i}{\not{p} - m_t - \Sigma_t(p)}, \tag{3.1.23}$$

the self-energy $\Sigma_t(p)$ would behave as

$$\Sigma_t(p) \sim \frac{1}{\log[(p^2 - m_t^2)/\Lambda_{QCD}^2]} \tag{3.1.24}$$

near on-shell, $p^2 \simeq m_t^2$. Again according to Veltman[27] we should use the full propagator in the evaluation of self-energy diagrams $\Sigma_t(p)$ self-consistently, which corresponds to the shift of mass, $m_t^2 \to m_t^2 - im_t\Gamma_t$, in the above expression.

This may be interpreted reasonably. As the pair-created t and $\bar{t}$ spread apart, they will decay before the color-flux-tube surround them and the hadronization occurs at the space-time scale Λ_{QCD}^{-1}. We may then discuss the 'propagation' of top quark disregarding the effect of quark confinement[4]. Hence, we will freely use the top propagator in the following context.

3.2 Formulation to Include $O(\alpha_s)$ Corrections

Inspired by the qualitative understanding of the toponium system given above, we will include the next-to-leading order corrections to the $t\bar{t}$ pair production amplitude. This section is concerned with the determination of the S-matrix element including $O(\alpha_s)$ corrections for the process $e^+e^- \to bW^+\bar{b}W^-$ near $t\bar{t}$ threshold. Also we present the formulas of the top quark 3-momentum distribution, $d\sigma/d|\mathbf{p}_t|d\cos\theta$, up to $O(\alpha_s)$. These are achieved in the following steps.

In subsection 3.2.a, we summarize the basic strategy for the determination of the S-matrix element, S_{fi}. As the non-trivial building blocks of S_{fi}, the $t\bar{t}V$ ($V = \gamma$ or Z^0) vertices are derived in 3.2.b, which are given in terms of the Green's functions of the non-relativistic Schrödinger equation. The explicit form of the S-matrix element including $O(\alpha_s)$ corrections is presented in 3.2.c. In 3.2.d, we discuss the potential that appears in the non-relativistic Schrödinger equation. In particular, we concentrate on the absorptive part of the potential which is closely connected with the differential cross section to be presented in the following subsection. In 3.2.e, we derive the formulas for the top quark 3-momentum distribution including $O(\alpha_s)$ corrections.

The details of the general framework for the perturbative expansion near threshold are given in Appendix A. We develop a method for the power counting of the diagrams in Appendix B as an important tool for identifying the $O(\alpha_s)$ corrections to the S-matrix element. We present the QCD potential to be used in the numerical analyses in Appendix C. An explicit calculation of the absorptive potential is given in Appendix D.

The formulas for the cross sections will be summarized in the next chapter.

3.2.a Strategy

In this subsection, we state the basic strategy for evaluating the $O(\alpha_s)$ corrections to the S-matrix element for the process $e^+e^- \to bW^+\bar{b}W^-$ near $t\bar{t}$ threshold.

First, we make an important comment regarding the expansion parameter of the perturbation. There appear two independent expansion parameters, α_s and α_W, in

the program of perturbative expansion in our problem. In principle, we may perform the expansion independently for each parameter. Meanwhile, as stated in Chapter 2, important and interesting physical consequences come out from the prediction that the top width Γ_t and the resonance level structure $\sim \alpha_s^2 m_t$ are of the same order of magnitude. Indeed there appear interplays between QCD interaction and electroweak interaction in various aspects[13,16]. (See Section 4.3, for example.) Therefore, we perform the perturbative expansion by treating α_s^2 and α_W as of the same order of magnitude in the subsequent analyses.

Let us consider which diagram will contribute to the $O(\alpha_s)$ correction to the S-matrix element. If we switch off the QCD interaction, only the diagram with $t\bar{t}$ intermediate state will be enhanced above threshold among all the tree diagrams for $e^+e^- \to bW^+\bar{b}W^-$; t and $\bar{t}$ propagators are enhanced for $p_t^2 - m_t^2$, $\bar{p}_t^2 - m_t^2 \sim m_t\Gamma_t$. Other diagrams are suppressed at least by $\alpha_W \sim \alpha_s^2$. Taking into account of the QCD interaction, again only the diagram with $t\bar{t}$ intermediate state will be enhanced near threshold; the threshold singularities enhance the amplitude for $p_t^2 - m_t^2$, $\bar{p}_t^2 - m_t^2 \sim O(\alpha_s^2)$.

So, one needs to consider the QCD corrections to the diagram $e^+e^- \to t\bar{t} \to bW^+\bar{b}W^-$. They can be classified into three components. Namely, (1)$t\bar{t}V$-vertex ($V = \gamma$ or Z^0) including the $O(\alpha_s)$ correction, (2)tbW-vertex including $O(\alpha_s)$ correction, and (3)Diagrams corresponding to the final state interactions. (one-gluon-exchange between t and $\bar{b}$ ($\bar{t}$ and b) and between b and $\bar{b}$ after the decay of the toponium resonances)

In order to determine the above components of the S-matrix element, it is necessary to know the $t\bar{t}$ 4-point function,

$$\mathcal{G}(x_1, x_2, x_3, x_4) = \langle 0 \,|\, T\, \psi(x_1)\bar{\psi}(x_2)\bar{\psi}(x_3)\psi(x_4) \,|\, 0 \rangle\,, \tag{3.2.1}$$

up to $O(\alpha_s)$, which contains the information of the toponium resonances. This is derived in Appendix A, and is given in terms of the Green's function of the non-relativistic Schrödinger equation. To identify the $O(\alpha_s)$ corrections properly, it is not sufficient just to apply the power counting method in terms of α_s and β for the determination

of the S-matrix element, or, specifically the 4-point function $\mathcal{G}$. One should take into account the analytic structure of the S-matrix element near the resonance poles and reorganize the perturbative expansion[29]. In brief, if the S-matrix element has the pole structure

$$S_{fi} = \frac{R}{s - s_P} + C(s), \tag{3.2.2}$$

one should include the $O(\alpha_s)$ corrections to the pole position s_P, the residue R, and the regular part $C(s)$, respectively. We explain in Appendix A the method of the reorganized perturbative expansion and its application to the practical calculation of the amplitude in detail.

In Subsections 3.2.b-3.2.e, we will determine the S-matrix elemtent as well as top quark 3-momentum distribution step by step using the 4-point function $\mathcal{G}$. Necessary setups for the calculations to be presented there are as follows.

Momentum Assignment

We will often use the momentum of the center of gravity, P, and the relative momentum, p, in describing the $t\bar{t}$ system. With these variables, the momenta of t and $\bar{t}$ are given by

$$p_t = P/2 + p, \tag{3.2.3}$$

$$\bar{p}_t = P/2 - p. \tag{3.2.4}$$

We fix the frame to the c.m. frame, and denote the components of each momentum as

$$P = (2m_t + E, \mathbf{0}) \quad \text{and} \quad p = (p^0, \mathbf{p}). \tag{3.2.5}$$

Here, $E = \sqrt{s} - 2m_t$ is the energy measured from the threshold. For the kinematical configuration of our interest, E, $p^0 \sim O(\alpha_s^2)$ and the top quark 3-momentum, $\mathbf{p} \sim O(\alpha_s)$.

Top Width

The top quark on-shell decay width including $O(\alpha_s)$ correction is given by[30,31,32]

$$\Gamma_t = \Gamma_t^0 \left\{ 1 - \frac{C_F \alpha_s}{2\pi}\, h(r) \right\} \tag{3.2.6}$$

with

$$\Gamma_t^0 = \frac{G_F}{\sqrt{2}} \frac{m_t^3}{8\pi} (1+2r)(1-r)^2, \tag{3.2.7}$$

$$h(r) = \pi^2 + 2\mathrm{Li}_2(r) - 2\mathrm{Li}_2(1-r) + [2(5+4r)(1-r)^2 \log(1-r) + 4(1+r)(1-2r)r\log r - (1-r)(5+9r-6r^2)]/[2(1-r)^2(1+2r)], \tag{3.2.8}$$

and

$$r = \frac{m_W^2}{m_t^2}, \tag{3.2.9}$$

and the color factor $C_F = 4/3$. We neglect the b-quark mass throughout this paper for simplicity.

Gauge Choice

It is well-known that Coulomb gauge is best suited to the calculation of bound state problems. This is because this gauge clearly separates the part that contributes at the leading order and that contributes at the subleading order; see Subsection 3.1.a. Consequently, the power counting of the diagrams becomes easy, where the soft transverse gluon attached to non-relativistic $t(\bar{t})$ or to other soft gluons is associated with a trivial suppression factor. It is known[33] that many cancellations occur in other gauges. Hence, we stick to the Coulomb gauge throughout this paper in the calculation of $O(\alpha_s)$ corrections.

3.2.b $t\bar{t}V$ Vertex

We determine the $t\bar{t}V$ vector vertex ($V = \gamma$ or Z^0) and $t\bar{t}Z^0$ axial-vector vertex defined by

$$\Lambda_V^i = \langle 0 \,|\, T\,\psi(x)\bar{\psi}(y) : \bar{\psi}(z)\gamma^i\psi(z) : |\, 0 \,\rangle, \tag{3.2.10}$$

$$\Lambda_A^i = \langle 0 \,|\, T\,\psi(x)\bar{\psi}(y) : \bar{\psi}(z)\gamma^i\gamma_5\psi(z) : |\, 0 \,\rangle. \tag{3.2.11}$$

As these vertices are contracted with the wave function of virtual γ or Z^0 produced by e^+e^- annihilation, only the space components of the vertices are relevant. Here and hereafter, the Latin indices refer to the space components.

***$t\bar{t}V$* Vector Vertex**

One may derive the vector vertex Λ_V^i using the $t\bar{t}$ 4-point function $\mathcal{G}^1(p,q,P)$ derived in Appendix A, eq. (A.50). One should contract the initial $t\bar{t}$ lines of the 4-point function and perform the loop integration over the relative momentum q, and obtains the vector vertex in momentum space as

$$\Lambda_V^i = \left(1 - \frac{2C_F\alpha_s}{\pi}\right) \tilde{\Lambda}_V^i, \tag{3.2.12}$$

$$\tilde{\Lambda}_V^i = S(P/2+p)\,\Gamma^i\,S(-P/2+p) + \int \tfrac{d^4q}{(2\pi)^4} \tfrac{d^4q'}{(2\pi)^4}\, \mathcal{G}_b^1(p,q,P)\,\Delta K(q,q',P)\,[S(P/2+q')\Gamma^i S(-P/2+q')], \tag{3.2.13}$$

$$\Gamma^i = -\gamma^i \times (E - \mathrm{p}^2/m_t + i\Gamma_t)\,\tilde{G}(\mathrm{p};E). \tag{3.2.14}$$

Here, the factor $(1 - 2C_F\alpha_s/\pi)$ with $C_F = 4/3$ in the first line, which is normally referred to as the hard gluon correction, stems from the loop integration over the relativistic region together with the renormalization of the QED $t\bar{t}\gamma$ vertex. Derivation of this factor is given in Ref.[34]. The same factor is associated with the $t\bar{t}Z^0$ vector vertex.

The loop integration of $\mathcal{G}^1$ over the non-relativistic region gives the vertex $\tilde{\Lambda}_V^i$ in eq. (3.2.13). Here, the top quark propagator is given by

$$S(p_t) = \frac{i(\not{p}_t + m_t)}{p_t^2 - m_t^2 + im_t\Gamma_t}. \tag{3.2.15}$$

See Appendix B for the spinor structure of $\tilde{\Lambda}_V^i$. The second term on the right-hand-side stems from a part of the $O(\alpha_s)$ corrections to the residues of the resonance poles. $\mathcal{G}_b^1$ is defined in Appendix A, eq. (A.52). The Bethe-Salpeter kernel ΔK which survives the integration is only the non-instantaneous kernel since $\mathcal{G}_b^1$ vanishes upon integration over the time variable:

$$\int \tfrac{dp^0}{(2\pi)}\, \mathcal{G}_b^1(p,q,P) = \int \tfrac{dq^0}{(2\pi)}\, \mathcal{G}_b^1(p,q,P) = 0. \tag{3.2.16}$$

The non-instantaneous kernel at the desired order is contained only in the absorptive part, and will be found in Subsection 3.2.d. Also, due to eq. (3.2.16) the second term in $\tilde{\Lambda}^i_V$ does not contribute to the top quark 3-momentum distribution, $d\sigma/d^3\mathbf{p}$.

The amputated vertex Γ^i in eq. (3.2.14) contains the S-wave Green's function, $\tilde{G}(\mathbf{p};E)$, which includes the spectra of the toponium resonances. It is obtained as the Fourier transform of $G(\mathbf{x};E)$, which satisfies the time-independent inhomogeneous Schrödinger equation in the presence of QCD potential:

$$\left[-\frac{\nabla^2}{m_t}+V_{QCD}(r)-(E+i\Gamma_t)\right]G(\mathbf{x};E)=\delta^3(\mathbf{x}), \tag{3.2.17}$$

$$\tilde{G}(\mathbf{p};E)=\int d^3\mathbf{x}\,e^{-i\mathbf{p}\cdot\mathbf{x}}\,G(\mathbf{x};E). \tag{3.2.18}$$

$t\bar{t}Z^0$ Axial-Vector Vertex

The axial-vector vertex Λ^i_A is the next-to-leading order quantity in itself as it is proportional to β near threshold.[1] This may be seen from the spinor structure of the axial-vertex:

$$\begin{aligned}&(\not{P}/2+\not{p}+m_t)\,\gamma^i\gamma_5\,(-\not{P}/2+\not{p}+m_t)\\&\quad=-im_t\,(1+\gamma^0)\,\sigma^{ij}\gamma_5 p^j\,(1-\gamma^0)+O(\beta^2)\end{aligned} \tag{3.2.19}$$

with

$$\sigma^{ij}=\frac{i}{2}[\gamma^i,\gamma^j]. \tag{3.2.20}$$

Keeping this in mind, we may obtain the axial-vector vertex from the 4-point function $\mathcal{G}^1(p,q,P)$. After contracting the initial $t\bar{t}$ lines and integrating over q, we find

$$\Lambda^i_A=-S(P/2+p)\,\gamma^i\gamma_5\,S(-P/2+p)\times(E-\mathbf{p}^2/m_t+i\Gamma_t)\,\tilde{F}(\mathbf{p};E), \tag{3.2.21}$$

where the P-wave Green's function $\tilde{F}(\mathbf{p};E)$ is defined by

$$\left[-\frac{\nabla^2}{m_t}+V_{QCD}(r)-(E+i\Gamma_t)\right]F^i(\mathbf{x};E)=-i\partial^i\delta^3(\mathbf{x}), \tag{3.2.22}$$

$$p^i\,\tilde{F}(\mathbf{p};E)=\int d^3\mathbf{x}\,e^{-i\mathbf{p}\cdot\mathbf{x}}\,F^i(\mathbf{x};E). \tag{3.2.23}$$

[1] We mean by the next-to-leading order ($O(\alpha_s)$) quantity that the residues and the regular part which contribute to the S-matrix element in (3.2.2) are $O(\alpha_s)$ as compared to the leading structure.

The axial-vector vertex is given in terms of the P-wave Green's function, which may be written as

$$F^i(\mathbf{x};E)=i\frac{\partial}{\partial x'^i}\sum_n\frac{\psi_n(\mathbf{x})\psi_n^*(\mathbf{x}')}{E-E_n+i\Gamma_t}\bigg|_{\mathbf{x}'=\mathbf{0}}. \tag{3.2.24}$$

The wave functions ψ_n's are the solutions to the homogeneous Schrödinger equation with the QCD potential

$$\left[-\frac{\nabla^2}{m_t}+V_{QCD}(r)\right]\psi_n(\mathbf{x})=E_n\,\psi_n(\mathbf{x}). \tag{3.2.25}$$

Eq. (3.2.24) clearly shows that only P-wave states contribute to $F^i(\mathbf{x};E)$. (cf. eq. (3.1.14).) We have neglected the higher order corrections to Λ^i_A in (3.2.21), such as relativistic corrections, since these are $O(\alpha_s^2)$ corrections as compared to the leading S-wave contribution. For the details of the axial-vector vertex, the readers are referred to Ref.[16].

3.2.c S-Matrix Element

Using the vertices obtained in the previous subsection, one may construct the S-matrix element for the process $e^+e^-\to bW^+\bar{b}W^-$ including $O(\alpha_s)$ corrections as follows:

$$S_{fi} = i\,(2\pi)^4\delta^4(P_f-P_i)\,T_{fi}, \tag{3.2.26}$$

$$iT_{fi} = \sum_{\substack{X=\gamma,Z^0\\ a,a'=V,A}}(i\,\tilde{g}_a^{tX}\,J^\mu_{f,a})\,\frac{-ig_{\mu\nu}}{s-m_X^2+im_X\Gamma_X}\,(i\,\tilde{g}_{a'}^{eX}\,J^\nu_{i,a'}), \tag{3.2.27}$$

where $\tilde{g}_V^{eX}(\tilde{g}_A^{eX})$ and $\tilde{g}_V^{tX}(\tilde{g}_A^{tX})$ represent the vector (axial-vector) couplings of e^- and t to X, respectively. The currents associated with $e^+e^-\to X$ ($X=\gamma$ or Z^0) are given by

$$J^\nu_{i,V} = \bar{v}_e\gamma^\nu u_e, \tag{3.2.28}$$

$$J^\nu_{i,A} = \bar{v}_e\gamma^\nu\gamma_5 u_e. \tag{3.2.29}$$

One may split the currents associated with $X\to t\bar{t}\to bW^+\bar{b}W^-$ into two parts:

$$J^\mu_{f,a}=J^{\mu[1]}_{f,a}+J^{\mu[2]}_{f,a}. \tag{3.2.30}$$

$J^{\mu[1]}_{f,a}$

The first part of $J^{\mu}_{f,a}$ is given by connecting the $t\bar{t}X$ vertex to the vertices for $t \to bW^+$ and $\bar{t} \to \bar{b}W^-$:

$$J^{\mu[1]}_{f,a} = \bar{u}_b \, \epsilon^*_{W+\alpha} \, \Gamma^{\alpha}_{tbW}(P/2+p) \cdot \Lambda^{\mu}_a \cdot \bar{\Gamma}^{\beta}_{tbW}(P/2-p) \, \epsilon^*_{W-\beta} \, v_{\bar{b}}. \tag{3.2.31}$$

The $t\bar{t}X$ vertices Λ^{μ}_V and Λ^{μ}_A are defined in (3.2.12) and (3.2.21), respectively.

The tbW-vertices including $O(\alpha_s)$ corrections are calculated to be

$$\Gamma^{\alpha}_{tbW}(p_t) = i\frac{g_W}{\sqrt{2}} \frac{1+\gamma_5}{2} \left[\gamma^{\alpha} + \frac{C_F \alpha_s}{4\pi} \left(h_1 \gamma^{\alpha} + h_2 \frac{p_t^{\alpha}}{m_t} \right) \right], \tag{3.2.32}$$

$$\bar{\Gamma}^{\beta}_{tbW}(\bar{p}_t) = i\frac{g_W}{\sqrt{2}} \left[\gamma^{\beta} + \frac{C_F \alpha_s}{4\pi} \left(h_1 \gamma^{\beta} - h_2 \frac{\bar{p}_t^{\beta}}{m_t} \right) \right] \frac{1-\gamma_5}{2} \tag{3.2.33}$$

with

$$\begin{aligned} h_1 &= -\frac{1}{2}\log^2 \epsilon_g + 2\log\epsilon_g \log(1-r) - \frac{5}{2}\log\epsilon_g \\ &\quad -2\mathrm{Li}_2(r) - 2\log^2(1-r) - \frac{1-3r}{4}\log(1-r) - \frac{15}{4} - \frac{\pi^2}{2}, \end{aligned} \tag{3.2.34}$$

$$h_2 = \frac{2}{r}\log(1-r) \tag{3.2.35}$$

and

$$r = \frac{m_W^2}{m_t^2}, \qquad \epsilon_g = \frac{m_g^2}{m_t^2}. \tag{3.2.36}$$

The $O(\alpha_s)$ corrections are evaluated for the on-shell top quark. This is justified since the effect of off-shellness of top quark is only $O(\alpha_s^2)$. The infra-red divergences are regularized by giving the gluon a small mass m_g, where the divergent terms as $m_g \to 0$ get canceled by adding to the cross section the corresponding terms of the cross section for the real gluon emission, $e^+e^- \to bW^+\bar{b}W^-g$; see Subsection 3.2.e.

$J^{\mu[2]}_{f,a}$

The second part of $J^{\mu}_{f,a}$ is given by the sum of diagrams corresponding to the final state interactions. It is obtained as the loop integral including the $t\bar{t}V$ vector vertex.[2] This loop integral is convergent in the ultra-violet region, and we need no

[2]The final state interaction diagrams with $t\bar{t}Z^0$ axial-vector vertex are $O(\alpha_s^2)$, and they will not be considered here.

renormalization. According to the power counting in Appendix B, $J^{\mu[2]}_{f,V}$ is an $O(\alpha_s)$ quantity in itself as compared to the leading contribution, and the relevant kinematical region is only where the exchanged gluon is soft. We list the relevant diagrams in Fig. 3.6, and write the contributions from these diagrams explicitly as

$$\begin{aligned} J^{\mu[2]}_{f,V} &= i\,C_F \cdot 4\pi\alpha_s \cdot \left(\frac{g_W}{\sqrt{2}}\right)^2 \\ &\quad \times \left(\bar{u}_b \, \not{\epsilon}^*_{W+} \frac{1-\gamma_5}{2} \frac{1+\gamma^0}{2} \gamma^{\mu} \frac{1-\gamma^0}{2} \not{\epsilon}^*_{W-} \frac{1-\gamma_5}{2} v_{\bar{b}} \right) \\ &\quad \times \int \frac{d^4q}{(2\pi)^4} \tilde{G}(\mathrm{q}; E) \, B(q,P) \, [\mathcal{M}_{(\mathrm{i})} + \mathcal{M}_{(\mathrm{ii})} + \mathcal{M}_{(\mathrm{iii})} + \mathcal{M}_{(\mathrm{iv})}]. \end{aligned} \tag{3.2.37}$$

with

$$B(q,P) = \frac{1}{E/2 + q^0 - \mathrm{q}^2/2m_t + i\Gamma_t/2} + \frac{1}{E/2 - q^0 - \mathrm{q}^2/2m_t + i\Gamma_t/2}. \tag{3.2.38}$$

The common structures to all diagrams are factored out, where we took advantage of the fact that only the soft region of the exchanged gluon is relevant and made appropriate approximations; see eq. (B.13). The remaining propagators of the diagrams (i)∼(iv) in Fig. 3.6 are given by

$$\mathcal{M}_{(\mathrm{i})} = \frac{1}{E/2 - p^0 - \mathrm{p}^2/2m_t + i\Gamma_t/2} \cdot \frac{1}{k^0 - \mathrm{n}_b \cdot \mathrm{k} + i\epsilon} \cdot \frac{1}{|\mathrm{k}|^2}, \tag{3.2.39}$$

$$\mathcal{M}_{(\mathrm{ii})} = \frac{1}{E/2 + p^0 - \mathrm{p}^2/2m_t + i\Gamma_t/2} \cdot \frac{1}{-k^0 + \bar{\mathrm{n}}_b \cdot \mathrm{k} + i\epsilon} \cdot \frac{1}{|\mathrm{k}|^2}, \tag{3.2.40}$$

$$\mathcal{M}_{(\mathrm{iii})} = \frac{1}{k^0 - \mathrm{n}_b \cdot \mathrm{k} + i\epsilon} \cdot \frac{1}{-k^0 + \bar{\mathrm{n}}_b \cdot \mathrm{k} + i\epsilon} \cdot \frac{1}{|\mathrm{k}|^2}, \tag{3.2.41}$$

$$\mathcal{M}_{(\mathrm{iv})} = \frac{1}{k^0 - \mathrm{n}_b \cdot \mathrm{k} + i\epsilon} \cdot \frac{1}{-k^0 + \bar{\mathrm{n}}_b \cdot \mathrm{k} + i\epsilon} \cdot \frac{1}{k^2 + i\epsilon} \times (\mathrm{n}_b \cdot \bar{\mathrm{n}}_b)_T. \tag{3.2.42}$$

Here, n_b and $\bar{\mathrm{n}}_b$ represent the unit vectors in the directions of b-quark and $\bar{b}$-quark 3-momenta, respectively, and $k = q - p$ denotes the gluon momentum:

$$\mathrm{n}_b = \frac{\mathrm{p}_b}{|\mathrm{p}_b|}, \qquad \bar{\mathrm{n}}_b = \frac{\bar{\mathrm{p}}_b}{|\bar{\mathrm{p}}_b|}, \tag{3.2.43}$$

and

$$(\mathrm{n}_b \cdot \bar{\mathrm{n}}_b)_T = \mathrm{n}_b \cdot \bar{\mathrm{n}}_b - \frac{(\mathrm{n}_b \cdot \mathrm{k})(\bar{\mathrm{n}}_b \cdot \mathrm{k})}{|\mathrm{k}|^2}. \tag{3.2.44}$$

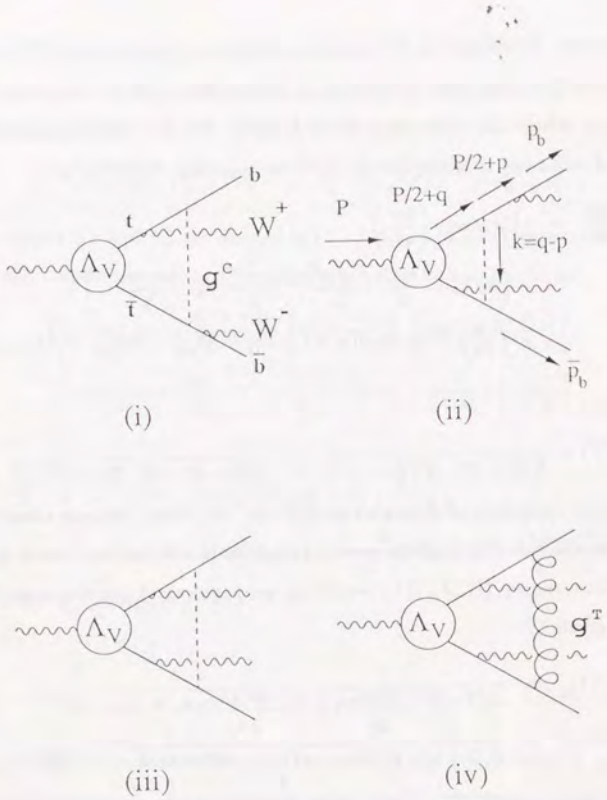

Figure 3.6: The final state interaction diagrams corresponding to $J^{\mu[2]}_{f,V}$. The dashed line represents the Coulmob gluon, while the curly line is for the transverse gluon.

One may perform the time integration, $\int \frac{dq^0}{(2\pi)}$, and the angular integration, $\int d\Omega_{\mathbf{q}}$, analytically in eq. (3.2.37) noting that the S-wave Green's function $\tilde{G}(\mathbf{q};E)$ depends only on $|\mathbf{q}|$. The angular integration can be performed straightforwardly as the diagrams (i)~(iv) are free from the collinear singularities. The remaining one-parameter integration $\int_0^\infty d|\mathbf{q}|$ may be attained numerically. The part of this integration corresponding to the diagram (iv) contains the soft-gluon singularity, which gets canceled when the cross section is added to that of the real gluon emission process.

3.2.d Absorptive Potential

The $t\bar{t}V$ vertices derived in 3.2.b are given in terms of the Green's functions of the inhomogeneous Schrödinger equations, $\tilde{G}(\mathbf{p};E)$ and $\tilde{F}(\mathbf{p};E)$. As shown in Appendices A and B, these Green's functions are obtained by solving the Schrödinger equations in the presence of the potential V, which is essentially the Bethe-Salpeter kernel K integrated over the relative time variables. This potential is calculated and given by the sum of the QCD potential and the absorptive part which is just the top quark width Γ_t:

$$V(\mathbf{p},\mathbf{q};E) = V_{QCD}(|\mathbf{p}-\mathbf{q}|) - i\Gamma_t(2\pi)^3\delta^3(\mathbf{p}-\mathbf{q}), \tag{3.2.45}$$

or, in coordinate space,

$$V(r) = V_{QCD}(r) - i\Gamma_t. \tag{3.2.46}$$

It turns out that up to $O(\alpha_s)$, $V(\mathbf{p},\mathbf{q};E)$ is energy- and spin-independent in the subspace represented by $(\frac{1+\gamma^0}{2}\otimes\frac{1-\gamma^0}{2})$, and depends only on $|\mathbf{p}-\mathbf{q}|$. The result is simple, but there exist remarkable cancellations in the absorptive part of the potential. We focus on the absorptive part of the potential in this subsection. In particular we calculate the contribution of the final state interaction diagrams to the absorptive potential, which turns out to vanish up to $O(\alpha_s)$. These calculations will be utilized in the derivation of differential cross sections in the next subsection. An explicit calculation of the absorptive potential is given in Appendix D.

The potential V is defined in Appendix A, eq. (A.49), which is given in terms of the Bethe-Salpeter kernel:

$$V = \left(-C_F \frac{4\pi\alpha_s}{|\mathbf{p}-\mathbf{q}|^2} - i\Gamma_t^0 (2\pi)^3 \delta^3(\mathbf{p}-\mathbf{q})\right) \left(\frac{1+\gamma^0}{2} \otimes \frac{1-\gamma^0}{2}\right) + \Delta V, \quad (3.2.47)$$

$$\Delta V(\mathbf{p},\mathbf{q};E) = \left(\frac{1+\gamma^0}{2} \otimes \frac{1-\gamma^0}{2}\right) \times \int \frac{dp^0}{(2\pi)} \frac{dq^0}{(2\pi)} [-iB(p,P)\Delta K(p,q,P)B(q,P)] \left(\frac{1+\gamma^0}{2} \otimes \frac{1-\gamma^0}{2}\right) \quad (3.2.48)$$

with

$$B(p,P) = \frac{1}{E/2 + p^0 - \mathbf{p}^2/2m_t + i\Gamma_t} + \frac{1}{E/2 - p^0 - \mathbf{p}^2/2m_t + i\Gamma_t}, \quad (3.2.49)$$

where ΔK is the perturbative kernel[3] which contribute to the $O(\alpha_s)$ correction; see eqs. (A.30), (A.31) and (A.34).

The diagrams which give rise to the $O(\alpha_s)$ corrections to the potential V can be identified by the power counting method as described in Appendix B. One may split the potential into two parts as

$$V = V_{QCD} + V_{abs}, \quad (3.2.50)$$

where V_{QCD} is the QCD potential and V_{abs} is the absorptive part of the potential that stems from the decay of resonances.

There have been a number of calculations of V_{QCD} at various levels. On the basis of earlier works[6,35,36,37], more realistic potentials have been proposed and used in the calculations of $t\bar{t}$ production cross sections[10,13,15]. Here, we quote the one-loop QCD potential[36] including massless quark loops, which is given by

$$V_{QCD}^{(1-loop)} = -C_F \frac{4\pi\alpha_s}{|\mathbf{k}|^2} \left[1 + \frac{\alpha_s}{4\pi}\left[C_A \left\{\frac{11}{3}\log\left(\frac{\mu^2}{\mathbf{k}^2}\right) + \frac{31}{9}\right\} - n_f \left\{\frac{2}{3}\log\left(\frac{\mu^2}{\mathbf{k}^2}\right) + \frac{10}{9}\right\}\right]\right] \quad (3.2.51)$$

in terms of $\alpha_s(\mu^2)$ defined in $\overline{\rm MS}$ renormalization scheme, with $\mathbf{k} = \mathbf{q}-\mathbf{p}$ and $C_F = 4/3$, $C_A = 3$. (cf. eq. (B.25)). (See, however, the discussion in Section 6.2.) The QCD

[3]Besides the diagrams belonging to the Bethe-Salpeter kernel K, ΔK includes the product of one-particle self-energies where no momentum is transferred between t and $\bar{t}$.

potential V_{QCD} used in our numerical studies presented in Chapters 4 and 5 is the two-loop improved potential[13], which is described in detail in Appendix C.

The absorptive potential V_{abs} is given in terms of the absorptive part of the Bethe-Salpeter kernel, and can be calculated from the decay process of the $t\bar{t}$ system. V_{abs} is directly related to the total cross section via the unitarity relation, and it determines the imaginary part of the resonance poles[13]. Cut-diagrams which contribute to V_{abs} up to $O(\alpha_s)$ are shown in Figs. 3.7 and 3.8. These are classified into two classes, Class (a) and Class (b), and we split the absorptive potential correspondingly:

$$V_{abs} = V_{abs}^{(a)} + V_{abs}^{(b)}. \quad (3.2.52)$$

The diagrams in Class (a) are those without momentum transfer between t and $\bar{t}$, and hence $V_{abs}^{(a)}$ becomes diagonal in momentum space. We have

$$V_{abs}^{(a)} = -i\Gamma_t (2\pi)^3 \delta^3(\mathbf{p}-\mathbf{q}). \quad (3.2.53)$$

Up to $O(\alpha_s)$, only the on-shell top width contributes to $V_{abs}^{(a)}$ as the effect of the running of top quark width starts at $\mathbf{p}^2/m_t^2 \sim O(\alpha_s^2)$.[13]

Now we present the contribution from the each cut-diagram in Class (b), which includes the momentum transfer between t and $\bar{t}$, to $V_{abs}^{(b)}$. These diagrams represent the final state interactions. Quite remarkably, it turns out that the total contribution vanishes up to $O(\alpha_s)$, while each diagram gives contribution at this order. Nevertheless, we list up the contributions from all diagrams anticipating that they will be utilized in the calculation of differential cross sections in the next subsection. In fact the final state interactions add non-trivial $O(\alpha_s)$ corrections to the differential cross sections. Vanishing of $V_{abs}^{(b)}$ suggests that the $O(\alpha_s)$ corrections from the final state interaction diagrams to the total cross section cancel out altogether; see Subsection 4.1.b.

We denote the sum of the contributions from the cut-diagrams (i)-(v) in Class (2) as $iQ(\mathbf{p},\mathbf{q};E)$ and that from the Dirac conjugate diagrams as $i\bar{Q}(\mathbf{p},\mathbf{q};E)$. Namely,

$$V_{abs}^{(b)}(\mathbf{p},\mathbf{q};E) = iQ(\mathbf{p},\mathbf{q};E) + i\bar{Q}(\mathbf{p},\mathbf{q};E) \quad (3.2.54)$$

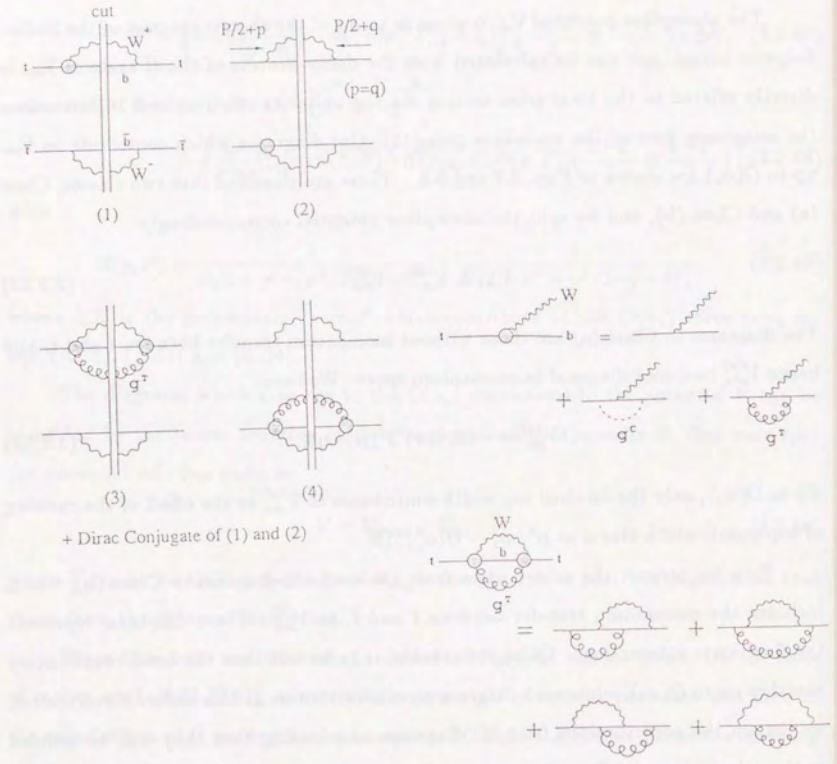

Figure 3.7: Class (a) diagrams of the cut-diagrams that contribute to the absorptive potential V_{abs} up to the next-to-leading order.

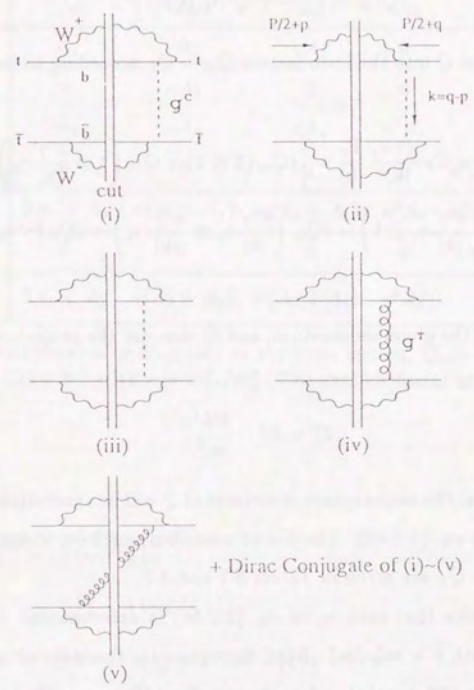

Figure 3.8: Class (b) diagrams of the cut-diagrams that contribute to the absorptive potential V_{abs} at the next-to-leading order.

with

$$\bar{Q}(\mathbf{p},\mathbf{q};E) = \gamma^0\, Q^\dagger(\mathbf{q},\mathbf{p};E)\,\gamma^0. \tag{3.2.55}$$

Then we decompose Q into the form factors $Q_{00} \sim Q_T$ according to its spinor structures as

$$Q(\mathbf{p},\mathbf{q};E) = C_F\,\frac{4\pi\alpha_s}{|\mathbf{k}|^2}\,\frac{\Gamma_t}{|\mathbf{k}|} \times \left[iQ_{00}\,(\mathbf{1}\otimes\mathbf{1}) + Q_{05}\left(\mathbf{1}\otimes\frac{k^i\gamma^i}{|\mathbf{k}|}\gamma_5\right) \right.$$
$$\left. + Q_{50}\left(\frac{k^i\gamma^i}{|\mathbf{k}|}\gamma_5\otimes\mathbf{1}\right) + iQ_{55}\left(\frac{k^i\gamma^i}{|\mathbf{k}|}\gamma_5\otimes\frac{k^j\gamma^j}{|\mathbf{k}|}\gamma_5\right) + iQ_T\,(\gamma^i\gamma_5\otimes\gamma^j\gamma_5)\,\delta_T^{ij}\right], \tag{3.2.56}$$

where $\mathbf{k} = \mathbf{q}-\mathbf{p}$ is the gluon momentum, and δ_T^{ij} denotes the projector to the transverse directions:

$$\delta_T^{ij} = \delta^{ij} - \frac{k^i k^j}{|\mathbf{k}|^2}. \tag{3.2.57}$$

It is understood that the above spinor structures of Q will be sandwitched by $\left(\frac{1+\gamma^0}{2}\otimes\frac{1-\gamma^0}{2}\right)$ on both sides. See eq. (3.2.48). The list of contributions from diagrams (i)-(v) to the form factors $Q_{00} \sim Q_T$ are given in Tables 3.1 and 3.2.

One may notice that each γ_5 in eq. (3.2.56) is accompanied by the factor $\kappa = (1-2r)/(1+2r)$ with $r = m_W^2/m_t^2$. Here, $2r$ represents the ratio of contributions from transverse W boson (W_T) and that from longitudinal W boson (W_L) to the decay width of top quark. As b-quark is doomed to be left-handed, W_T and W_L project the different spin orientations of parent top quark with respect to the direction of b-quark momentum. Thus, $W_L + W_T$ combination acts as if it were vector-like coupling associated with the spinor structure of $Q(\mathbf{p},\mathbf{q};E)$, while W_L–W_T combination acts as if it were axial-vector-like coupling. (The $W_L + W_T$ combination is contained in the top width Γ_t as can be seen in eq. (3.2.7).)

Noting that the form factors $Q_{00} \sim Q_T$ are real, we find

$$V_{abs}^{(b)} = i\,[Q + \bar{Q}] = 0. \tag{3.2.58}$$

Form Factors	Q_{00}	Q_{05}	Q_{50}	Q_{55}	Q_T
Diagram (i)	A_1	0	κA_2	0	0
Diagram (ii)	A_1	κA_2	0	0	0
Diagram (iii)	A_3	κA_4	κA_4	$\kappa^2 A_5$	0
Diagram (iv)	0	0	0	0	$\kappa^2(A_6 - iA_7)$
Sum of (i)-(iv)	$2A_1 + A_3$	$\kappa(A_2 + A_4)$	$\kappa(A_2 + A_4)$	$\kappa^2 A_5$	$\kappa^2(A_6 - iA_7)$
Diagram (v)	0	0	0	0	$i\kappa^2 A_7$
Total	$2A_1 + A_3$	$\kappa(A_2 + A_4)$	$\kappa(A_2 + A_4)$	$\kappa^2 A_5$	$\kappa^2 A_6$

Table 3.1: The contribution of diagrams to the form factors, $Q_{00} \sim Q_T$, of $Q(\mathbf{p},\mathbf{q};E)$. Here, $\kappa = (1-2r)/(1+2r)$ with $r = m_W^2/m_t^2$. The explicit forms of $A_1 \sim A_7$ are given in Table 3.2.

$$\begin{aligned}
A_1 &= \tfrac{1}{2}\tan^{-1}\left(\tfrac{1}{\lambda}\right) \\
A_2 &= \tfrac{1}{2}\left[1 - \lambda\tan^{-1}\left(\tfrac{1}{\lambda}\right)\right] \\
A_3 &= \tfrac{1}{2}\lambda\tan^{-1}\left(\tfrac{1}{\lambda}\right)\left[\pi - \tan^{-1}\left(\tfrac{1}{\lambda}\right)\right] \\
A_4 &= \tfrac{1}{2}\lambda\tan^{-1}\left(\tfrac{1}{\lambda}\right) \\
A_5 &= -\tfrac{1}{2}\lambda\left[1 - \lambda\tan^{-1}\left(\tfrac{1}{\lambda}\right)\right]\left[\pi\lambda + 1 - \lambda\tan^{-1}\left(\tfrac{1}{\lambda}\right)\right] \\
A_6 &= \tfrac{1}{8}\left(A_3 + A_5 + \tfrac{\lambda}{1+\lambda^2}\right) \\
A_7 &= \tfrac{1}{8}\tfrac{\lambda^2}{1+\lambda^2}
\end{aligned}$$

Table 3.2: The coefficients that appear in the form factors of $Q(\mathbf{p},\mathbf{q};E)$ given in Table 3.1. Here, $\lambda = \Gamma_t/|\mathbf{k}|$.

We may estimate the order of magnitude of the coefficients, $A_1 \sim A_7$, which represent the contributions of the diagrams to the form factors $Q_{00} \sim Q_T$; see Tables 3.1 and 3.2. As shown by power counting in Appendix B, there are two kinematical regions of the gluon momentum k which give rise to the $O(\alpha_s)$ corrections to the absorptive potential depending on the diagrams. For each region, the orders of $A_1 \sim A_7$ are estimated to be

$$\begin{aligned}
&\text{region (I)} \quad : \quad \mathrm{k} \sim O(\alpha_s), \\
&\qquad \lambda \sim O(\alpha_s) \quad \text{and} \quad A_1,\, A_2 \;\sim\; O(1), \\
&\qquad\qquad\qquad\qquad\quad A_3 \sim A_6 \;\sim\; O(\alpha_s), \\
&\qquad\qquad\qquad\qquad\quad\; A_7 \;\sim\; O(\alpha_s^2), \\
&\text{region (II)} \quad : \quad \mathrm{k} \sim O(\alpha_s^2), \\
&\qquad \lambda \sim O(1) \quad \text{and} \quad A_1 \sim A_7 \;\sim\; O(1)
\end{aligned} \tag{3.2.59}$$

with $\lambda = \Gamma_t/|\mathrm{k}|$.

3.2.e Differential Cross Sections

One may now calculate the 3-momentum distribution of top quark,

$$\frac{d\sigma}{d|\mathrm{p}|d\cos\theta}, \tag{3.2.60}$$

including $O(\alpha_s)$ corrections by using the S-matrix element obtained in 3.2.c. There are two processes that contribute to the distribution, namely, the process $e^+e^- \to bW^+\bar{b}W^-$, and the infra-red part of the process $e^+e^- \to bW^+\bar{b}W^-g$, where the gluon jet is indistinguishable from the b and/or $\bar{b}$ jet. We present the cross section for each of these processes in succession. The sum of the two cross sections as well as the total cross section will be given in the next Chapter.

1. $e^+e^- \to bW^+\bar{b}W^-$

The top quark 3-momentum distribution can be calculated from the absolute square of the amplitude given in eq. (3.2.27) and integrating over the bW^+ and $\bar{b}W^-$ phase space by fixing the top quark 3-momentum p. Let us parametrize the cross section

as

$$\frac{d\sigma_{t\bar{t}}}{d|\mathrm{p}|d\cos\theta} = \frac{3\alpha^2\Gamma_t}{2m_t^4}\,|\mathrm{p}|^2\,(T_0^{t\bar{t}} + T_1^{t\bar{t}}\cos\theta). \tag{3.2.61}$$

Here, θ represents the polar angle of top quark 3-momentum measured from the electron beam direction. $T_0^{t\bar{t}}$ includes the leading S-wave contribution, while $T_1^{t\bar{t}}$ is $O(\alpha_s)$ in itself. These can be separated as

$$T_0^{t\bar{t}} = T_0^{(VV)} + T_0^{(FI)}, \tag{3.2.62}$$

$$T_1^{t\bar{t}} = T_1^{(VA)} + T_1^{(FI)}, \tag{3.2.63}$$

according to their orgins.

Vector-Vector Term

The vector-vector interference of the $J^{\mu[1]}_{f,V}$ part of the S-matrix element gives contribution to the spherically symmetric distribution of top quark as

$$\begin{aligned}
T_0^{(VV)} &= \left[\left(-\frac{2}{3} + \chi g_V^t g_V^e\right)^2 + \chi^2 (g_V^t)^2 (g_A^e)^2\right] \\
&\quad \times \left\{1 - \frac{4C_F\alpha_s}{\pi} - \frac{C_F\alpha_s}{2\pi}\cdot 2h_{bWg}(\epsilon;r)\right\} |\tilde{G}(\mathrm{p};E)|^2.
\end{aligned} \tag{3.2.64}$$

This contribution is represented by the cut-diagrams (1) and (2) in Class (a) in Fig. 3.7 contracted with the $t\bar{t}V$ vector vertices on both sides.

In eq. (3.2.64), $C_F = 4/3$ is the color factor. The couplings associated with $e^+e^-Z^0$ and $t\bar{t}Z^0$ vertices are given by

$$g_V^e = -\tfrac{1}{2} + 2\sin^2\theta_W, \quad g_A^e = -\tfrac{1}{2}, \tag{3.2.65}$$

$$g_V^t = \tfrac{1}{2} - \tfrac{4}{3}\sin^2\theta_W, \quad g_A^t = \tfrac{1}{2}, \tag{3.2.66}$$

while the ratio of photon and Z^0 propagators with an appropriate normalization factor is defined as

$$\chi = \frac{1}{4\sin^2\theta_W\cos^2\theta_W}\,\frac{s}{s - m_Z^2}\Big|_{s=4m_t^2}. \tag{3.2.67}$$

The S-wave Green's function $\tilde{G}(\mathrm{p};E)$ is defined in eqs. (3.2.17) and (3.2.18).

We have regularized the infra-red singularities by adding to the cross section the very soft part of the real gluon emission cross section, $(p_b+p_g)^2 < \epsilon m_t^2$ and $(\bar{p}_b+p_g)^2 < \epsilon m_t^2$. The partial decay width of top quark into bWg_{vis} is denoted as

$$\Gamma[t \to bWg_{vis}]_{(p_b+p_g)^2>m_t^2 y} = \Gamma_t^0 \times \frac{C_F\alpha_s}{2\pi}\, h_{bWg}(y;r), \tag{3.2.68}$$

where the visible gluon is defined by the cut $(p_b+p_g)^2 > m_t^2 y$. Γ_t^0 is given in (3.2.7). The explicit form of the function $h_{bWg}(y;r)$ will be given in the latter half of this subsection; see eq. (3.2.85).

Vector-Axial-Vector Term

The vector-axial-vector interference of the $J_{f,A}^{\mu[1]}$ part of the S-matrix element gives a term to the cross section proportional to $\cos\theta$ as

$$T_1^{(VA)} = \left(-\frac{2}{3}\chi g_A^e g_A^t + 2\chi^2 g_A^e g_V^e g_A^t g_V^t\right)\cdot\frac{|\mathbf{p}|}{m_t}\cdot 2\mathrm{Re}[\tilde{F}^*(\mathbf{p};E)\,\tilde{G}(\mathbf{p};E)]. \tag{3.2.69}$$

This is represented by the cut-diagrams (1) and (2) in Class (a) in Fig. 3.7 contracted with the $t\bar{t}V$ vector and axial-vector vertices on both sides. $T_1^{(VA)}$ stems from the interference of the S-wave and P-wave resonance states as described in detail in Subsection 4.3.a. The P-wave Green's function $\tilde{F}(\mathbf{p};E)$ is defined in eqs. (3.2.22) and (3.2.23).

Final State Interaction Terms

Here, we concentrate on the contributions to the cross section which stem from the interferences of final state interaction diagrams and the leading S-wave amplitude. This corresponds to the cut-diagrams (i)-(iv) in Class (b) in Fig. 3.8 contracted with the $t\bar{t}V$ vector vertices on both sides. For the rest of this subsection, we use the abbreviated notations

$$\mathcal{R} \equiv \mathrm{Re}[\tilde{G}^*(\mathbf{q};E)\,\tilde{G}(\mathbf{p};E)], \tag{3.2.70}$$

$$\mathcal{I} \equiv \mathrm{Im}[\tilde{G}^*(\mathbf{q};E)\,\tilde{G}(\mathbf{p};E)], \tag{3.2.71}$$

which express the interferences of the toponium resonance states within the loop integral and those in the $J_{f,V}^{\mu[1]}$ part of the S-matrix element.

We may utilize the cut-diagram contribution to the absorptive potential, $Q(\mathbf{p},\mathbf{q};E)$, derived in Subsection 3.2.d in performing the bW^+ and $\bar{b}W^-$ phase space integrations for a fixed top quark 3-momentum. Then it is straightforward to obtain

$$T_0^{(FI)} = \left[\left(-\frac{2}{3}+\chi g_V^t g_V^e\right)^2 + \chi^2 (g_V^t)^2 (g_A^e)^2\right]\cdot C_F\cdot 4\pi\alpha_s \times\int\frac{d^3\mathbf{q}}{(2\pi)^3}\frac{1}{|\mathbf{k}|^3}\left[2\mathcal{I}(Q_{00}+Q_{55})-\frac{2}{3}P_0\{2\mathcal{I}(Q_{55}-Q_T^r)+2\mathcal{R}Q_T^i\}\right] \tag{3.2.72}$$

$$T_1^{(FI)} = 2\chi g_A^e g_V^t\left(-\frac{2}{3}+\chi g_V^e g_V^t\right)\cdot C_F\cdot 4\pi\alpha_s \times\int\frac{d^3\mathbf{q}}{(2\pi)^3}\frac{1}{|\mathbf{k}|^3}P_1\cdot 2\mathcal{R}(Q_{05}+Q_{50}) \tag{3.2.73}$$

where

$$P_0 = 1, \quad P_1 = x \quad \text{with} \quad x = \frac{\mathbf{p}\cdot\mathbf{k}}{|\mathbf{p}|\,|\mathbf{k}|}. \tag{3.2.74}$$

The gluon momentum is denoted as $\mathbf{k} = \mathbf{q} - \mathbf{p}$. $Q_{00} \sim Q_T$ represent the form factors of $Q(\mathbf{p},\mathbf{q};E)$, and we set $Q_T^r = \kappa^2 A_6$, $Q_T^i = \kappa^2 A_7$; see Tables 3.1 and 3.2 in the previous subsection.

One may develop the power counting of $\mathcal{R}$ and $\mathcal{I}$, defined in (3.2.70) and (3.2.71), corresponding to the two different kinematical regions of the gluon momentum as

$$\begin{aligned}&\text{region (I)} \;:\; \mathbf{k}\sim O(\alpha_s),\;\; \mathcal{R}\sim O(\alpha_s^{-4}),\;\; \mathcal{I}\sim O(\alpha_s^{-4}),\\ &\text{region (II)} \;:\; \mathbf{k}\sim O(\alpha_s^2),\;\; \mathcal{R}\sim O(\alpha_s^{-4}),\;\; \mathcal{I}\sim O(\alpha_s^{-3}),\end{aligned} \tag{3.2.75}$$

see Appendix B. We may combine this with the power counting of the form factors given in eq. (3.2.59). Then, up to the desired order, the contributions of the final state interaction diagrams simplify to

$$T_0^{(FI)} = \left[\left(-\frac{2}{3}+\chi g_V^t g_V^e\right)^2 + \chi^2 (g_V^t)^2 (g_A^e)^2\right]\cdot C_F\cdot 4\pi\alpha_s \times\int\frac{d^3\mathbf{q}}{(2\pi)^3}\frac{1}{|\mathbf{k}|^3}\left(2\mathcal{I}Q_{00}-\frac{2}{3}P_0\cdot 2\mathcal{R}Q_T^i\right) \tag{3.2.76}$$

$$T_1^{(FI)} = 2\chi g_A^e g_V^t\left(-\frac{2}{3}+\chi g_V^e g_V^t\right)\cdot C_F\cdot 4\pi\alpha_s \times\int\frac{d^3\mathbf{q}}{(2\pi)^3}\frac{1}{|\mathbf{k}|^3}P_1\cdot 2\mathcal{R}(Q_{05}+Q_{50}) \tag{3.2.77}$$

with

$$Q_{00} \to \frac{\pi}{2}. \tag{3.2.78}$$

Here, one sees the presence of the soft-gluon singularity in the $\mathcal{R}$-term of $T_0^{(FI)}$, which cancels against the real gluon emission cross section; see eq. (3.2.83) below. The $\mathcal{I}$-term of $T_0^{(FI)}$ is infra-red safe since $\mathcal{I} \to 0$ as $\mathrm{k} \to 0$. Seemingly divergent behavior in the soft-gluon region of the loop integration in $T_1^{(FI)}$ is avoided by taking the principal value of the integration, since $T_1^{(FI)}$ comes solely from the exchange of Coulomb gluon, see Appendix D.

The final state interaction diagrams contribute to the top quark momentum distribution the terms that is spherically symmetric (T_0) and that is proportional to $\cos\theta$ (T_1), corresponding to the even and odd number of the axial-vector vertices of the tbW vertices contained in the diagram, respectively. This can be seen from the spinor structure of $Q(\mathrm{p}, \mathrm{q}; E)$ in eq. (3.2.56).

One may even think that the form factors Q_{55} and Q_T defined in eq. (3.2.56) would contribute to the angular distribution of top quark proportional to $(3\cos^2\theta - 1)/2$, since they are associated with the spinor structure

$$\left(\frac{k^i\gamma^i}{|\mathrm{k}|}\gamma_5 \otimes \frac{k^j\gamma^j}{|\mathrm{k}|}\gamma_5\right). \tag{3.2.79}$$

It can be shown, however, that this part vanishes at the desired order.

2. $e^+e^- \to bW^+\bar{b}W^-g$

The cross section for the real gluon emission process, $e^+e^- \to bW^+\bar{b}W^-g$, also gives contribution to the $O(\alpha_s)$ correction to the leading cross section. Here, we are concerned only with the kinematical configurations which look like $bW^+\bar{b}W^-$ final state as we are interested in the momentum distribution of top quark. We introduce the cuts on the bg and $\bar{b}g$ invariant masses, and calculate the cross section for the configurations which satisfy either of the conditions,

$$(p_b + p_g)^2 < m_t^2 y \quad \text{or} \quad (\bar{p}_b + p_g)^2 < m_t^2 y. \tag{3.2.80}$$

We assume

$$y \gtrsim O(\alpha_s) \tag{3.2.81}$$

in the following formulas.

Such kinematical configurations can be divided into 3 regions:

$$\text{Region (X)}: \quad (p_b + p_g)^2 < m_t^2 y, \quad (\bar{p}_b + p_g)^2 > m_t^2 y,$$
$$\text{Region (Y)}: \quad (p_b + p_g)^2 > m_t^2 y, \quad (\bar{p}_b + p_g)^2 < m_t^2 y,$$
$$\text{Region (Z)}: \quad (p_b + p_g)^2 < m_t^2 y, \quad (\bar{p}_b + p_g)^2 < m_t^2 y,$$

and we define the "top" momentum in each region as follows.

In region (X), where the b-jet and the gluon jet tend to be indistinguishable, the "top" momentum is defined as $p_t \equiv p_b + p_W + p_g$ if and only if $(p_b + p_W + p_g)^2 - m_t^2 \lesssim O(\alpha_s^2)$.[4] Namely, we integrate over the phase space region only for $(p_b + p_W + p_g)^2 - m_t^2 \lesssim O(\alpha_s^2)$. The similar definition of the "top" momentum is employed in region (Y).

In region (Z), again we define the "top" momentum as $p_t \equiv p_b + p_W + p_g$ if $(p_b + p_W + p_g)^2 - m_t^2 \lesssim O(\alpha_s^2)$, *or*, as $p_t \equiv p_b + p_W$ if $(p_b + p_W)^2 - m_t^2 \lesssim O(\alpha_s^2)$. If the both conditions on the bW invariant masses are met simultaneously, we calculate the differential cross section corresponding to the each assignment of "top" momentum, and take the average of the two cross sections.

We skip the derivation, and only present the results. The differential cross section of top quark from the real gluon emission process, $e^+e^- \to bW^+\bar{b}W^-g$, is given by

$$\frac{d\sigma_{t\bar{t}g}}{d|\mathrm{p}|d\cos\theta} = \frac{3\alpha^2\Gamma_t}{2m_t^4}|\mathrm{p}|^2\, T_0^{(RE)} \tag{3.2.82}$$

with

$$T_0^{(RE)} = \left[\left(-\frac{2}{3} + \chi g_V^t g_V^e\right)^2 + \chi^2 (g_V^t)^2 (g_A^e)^2\right]$$

[4] We assume that the cuts on the bW invariant masses are wide enough such that they include all the kinematical region enhanced by the top quark propagators, but not *too* wide, where they should not extend over the wider region $m_{bW}^2 - m_t^2 \sim O(\alpha_s)$. This assumption is taken advantage of in the power counting for estimating the magnitude of the diagrams. The dependence of the cross section on the value of the cuts (on the bW invariant masses) is only higher order corrections as long as the above assumption is satisfied.

$$\times \left[\frac{C_F \alpha_s}{2\pi} \cdot 2\{h_{bWg}(\epsilon; r) - h_{bWg}(y; r)\} \, |\tilde{G}(\mathrm{p}; E)|^2 \right.$$
$$\left. + C_F \cdot 4\pi\alpha_s \int \frac{d^3\mathrm{q}}{(2\pi)^3} \frac{1}{|\mathrm{k}|^3} \frac{2}{3} P_0 \cdot 2\mathcal{R} Q_T^i \right]. \qquad (3.2.83)$$

We have regularized the infra-red singularities by restricting the phase space integral in the region $(p_b + p_g)^2 > \epsilon m_t^2$ and $(\bar{p}_b + p_g)^2 > \epsilon m_t^2$.

Here, the partial decay width of top quark for $t \to bWg_{vis}$ is denoted as

$$\Gamma[t \to bWg_{vis}]_{(p_b+p_g)^2>y} = \Gamma_t^0 \times \frac{C_F \alpha_s}{2\pi} h_{bWg}(y; r) \qquad (3.2.84)$$

with

$$h_{bWg}(y; r) = 2\left[\mathrm{Li}_2(x_+) - \mathrm{Li}_2(x_-) - \mathrm{Li}_2\left(\tfrac{x_+}{1-r}\right) + \mathrm{Li}_2\left(\tfrac{x_-}{1-r}\right) - \tfrac{1}{2}\log\tfrac{y}{(1-r)^2}\log\tfrac{x_+}{x_-} \right]$$
$$+ \Big[-2r(1+r)(1-2r)\log\tfrac{1-x_+}{1-x_-} + (x_+ - x_-)(5 + 7r - 8r^2 + y)$$
$$- \tfrac{1}{2}(1+2r)\{7(1-r)^2 + 4(1-r)y + y^2\}\log\tfrac{x_+}{x_-} \Big] / \{(1-r)^2(1+2r)\}, \qquad (3.2.85)$$

and Γ_t^0 given in (3.2.7). The visible gluon (g_{vis}) is the gluon which can be seen as a separate jet, and is defined by the cut $(p_b + p_g)^2 > y$. In eq. (3.2.85), x_+ and x_- ($x_+ > x_-$) are defined as the two solutions to the quadratic equation, $x^2 - (1 - r + y)x + y = 0$.

Perhaps one may wish to relax the cuts imposed on the bW invariant masses, $m_{bW^+}^2 - m_t^2, m_{bW^-}^2 - m_t^2 \lesssim O(\alpha_s^2)$, to see the contributions from other kinematical region. In fact the real gluon emission cross section, whose kinematical configuration looks like $bW^+\bar{b}W^-$ final state, has a wider support over the phase space of bW invariant masses, $m_{bW^+}^2 - m_t^2, m_{bW^-}^2 - m_t^2 \sim O(\alpha_s)$, due to the presence of the "wrongly assigned diagram". Fig. 3.9 shows the contribution of this diagram. Consider the kinematical configuration $(p_b + p_g)^2 < m_t^2 y$ and $\mathrm{p}_g \sim O(\alpha_s)$, where the "top" momentum will be assigned as $p_t = p_b + p_W + p_g$. While the second diagram is enhanced for $p_t^2 - m_t^2 \sim O(\alpha_s^2)$, the "wrongly assigned diagram" is enhanced for $(p_b + p_W)^2 - m_t^2 \sim O(\alpha_s^2)$, which corresponds to $p_t^2 - m_t^2 \sim O(\alpha_s)$.

If the cuts on the bW invariant masses were removed, one would obtain the addi-

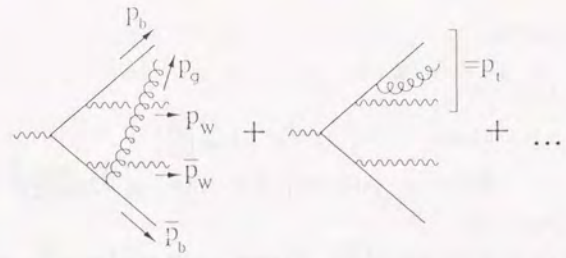

"Wrongly Assigned Diagram"

Figure 3.9: The amplitude for $\gamma^* \to bW^+\bar{b}W^-g$. The first term represents the "wrongly assigned diagram" for the kinematical configuration $(p_b + p_g)^2 < m_t^2 y$ and $\mathrm{p}_g \sim O(\alpha_s)$.

tional contribution to the cross section presented in (3.2.82) and (3.2.83). One finds

$$\frac{d\sigma_{tig}^{(WA)}}{d|\mathrm{p}|d\cos\theta} = \frac{3\alpha^2\Gamma_t}{2m_t^4} |\mathrm{p}|^2 \left[T_0^{(WA)} + T_2^{(WA)} \frac{3\cos\theta^2 - 1}{2} \right] \qquad (3.2.86)$$

with

$$T_0^{(WA)} = \left[\left(-\frac{2}{3} + \chi g_V^t g_V^e \right)^2 + \chi^2 (g_V^t)^2 (g_A^e)^2 \right] \cdot C_F \cdot 4\pi\alpha_s \cdot \int \frac{d^3\mathrm{q}}{(2\pi)^3} \frac{1}{|\mathrm{k}|^3}$$
$$\times |\tilde{G}(\mathrm{q}; E)|^2 \left\{ \Phi_{00}(y_0) - \kappa^2 \Phi_{55}(y_0) + \frac{2}{3} P_0 \cdot \kappa^2 \Phi_{55}(y_0) \right\}, \qquad (3.2.87)$$

$$T_2^{(WA)} = \left[\left(-\frac{2}{3} + \chi g_V^t g_V^e \right)^2 + \chi^2 (g_V^t)^2 (g_A^e)^2 \right] \cdot C_F \cdot 4\pi\alpha_s$$
$$\times \int \frac{d^3\mathrm{q}}{(2\pi)^3} \frac{1}{|\mathrm{k}|^3} |\tilde{G}(\mathrm{q}; E)|^2 \left(-\frac{2}{3} P_2 \right) \kappa^2 \Phi_{55}(y_0). \qquad (3.2.88)$$

Here,

$$P_0 = 1, \quad P_2 = \frac{3x^2 - 1}{2} \quad \text{with} \quad x = \frac{\mathrm{p} \cdot \mathrm{k}}{|\mathrm{p}|\,|\mathrm{k}|}, \qquad (3.2.89)$$

and

$$y_0 = \frac{2}{1-r} \frac{m_t}{|\mathrm{k}|} y, \qquad r = \frac{m_W^2}{m_t^2}. \qquad (3.2.90)$$

The gluon momentum is denoted as $\mathrm{k}(= \mathrm{p}_g) = \mathrm{q} - \mathrm{p}$. The bW phase space integrations of the "wrongly assigned diagram" are expressed by the appropriately normalized

functions Φ_{00} and Φ_{55}:

For $\eta < 2$:

$$\Phi_{00}(\eta) = \tfrac{1}{4}\eta\left[-(2-\eta) + 2\log\left(\tfrac{2}{\eta}\right)\right] \quad (3.2.91)$$

$$\Phi_{55}(\eta) = \tfrac{1}{8}\eta(2-\eta)\left[-\tfrac{1}{2}(2-\eta)(4-\eta) + 2\log\left(\tfrac{2}{\eta}\right)\right] \quad (3.2.92)$$

For $\eta > 2$:

$$\Phi_{00}(\eta) = \Phi_{55}(\eta) = 0. \quad (3.2.93)$$

The contribution of $d\sigma_{t\bar{t}g}^{(WA)}$ may be of interest in estimating the magnitude of the $O(\alpha_s)$ corrections. We come back to this contribution in Chapter 5, where all the $O(\alpha_s)$ corrections are examined. However, we do not include $d\sigma_{t\bar{t}g}^{(WA)}$ in the analyses of the cross sections presented in Chapter 4, since the cuts on the bW invariant masses $m_{bW}^2 - m_t^2 \lesssim O(\alpha_s^2)$ will be imposed practically.

Chapter 4

Cross Sections and Physics Involved

It is expected that one may extract various physical parameters in the $t\bar{t}$ pair production process near the threshold in e^+e^- collisions. Here, we present the numerical analyses of the cross sections including the full next-to-leading order corrections together with the elucidation of the underlying physics. We focus on the dependences of the cross sections on the parameters m_t and α_s, which determine the main shape of the cross sections over the threshold region.

We will first summarize the formulas of the cross sections in Section 4.1 to be used in the analyses in the following two sections. The total cross section and the momentum distribution of top quark are examined in Section 4.2. Then we turn to the FB-asymmetry and the $\cos\theta$ distribution of top quark in Section 4.3, which are $O(\alpha_s)$ quantities, but provide an interesting physics.

4.1 Formulas of the Cross Sections

In this section we summarize the formulas of the $t\bar{t}$ production cross sections near the threshold in e^+e^- collisions including all the $O(\alpha_s)$ corrections. We present the formula of the top quark 3-momentum distribution $d\sigma/d|\mathbf{p}_t|d\cos\theta$ in 4.1.a and the formula of the total cross section $\sigma_{tot}(e^+e^- \to t\bar{t})$ in 4.1.b. These are calculated from the differential cross sections for the processes $e^+e^- \to bW^+\bar{b}W^-$ and $e^+e^- \to bW^+\bar{b}W^-g$ obtained in Chapter 3 on the basis of the perturbation theory including heavy threshold resonances,

and are summarized in concise forms that serve for the direct use in the analyses of the cross sections presented in Sections 4.2 and 4.3. We neglect the b-quark mass in all formulas for simplicity, except in the QCD potential through which the cross sections would be most sensitive to m_t.

In addition to all the $O(\alpha_s)$ corrections, we include a part of the $O(\alpha_s^2)$ corrections to the cross sections given below. These are (1)Two-loop corrections to the QCD potential $V_{QCD}(r)$, and (2)Running of the toponium width $\Gamma_\Theta(E, \mathbf{p})$:

(1) We use the two-loop improved QCD potential $V_{QCD}(r)$ in the Schrödinger equations for the Green's functions, $G(\mathbf{x}; E)$ and $F^i(\mathbf{x}; E)$, which determine the overall structures of cross sections in the threshold region. This QCD potential is determined from the two-loop perturbative QCD (improved by renormalization group) in the short-distance part, while the long-distance part is determined phenomenologically. The overall form of the potential is determined by fitting to charmonium and bottomonium data. The explicit formula and the detailed description of the potential are given in Appendix C.

(2) Also we include the phase space suppression effect to the widths of the toponium resonances, which is achieved by replacing the top quark width by the running toponium width,

$$\Gamma_t \to \frac{\Gamma_\Theta(E, \mathbf{p})}{2}, \tag{4.1.1}$$

in the Schrödinger equations for the non-relativistic Green's functions, and also by including the $O(\beta^2)$ terms of the phase space volume of bW's; see cross section formulas below. This prescription takes into account of the phase space suppression for the decay of the deeply bound states, and found to be important in preserving the unitarity relation between the total cross section obtained from summing the final states and that calculated using the optical theorem. The running toponium width reduces the top quark differential cross section in the highly off-shell region as compared to the constant width approximation, while enhances the total cross section at the resonance peak which is proportional to the inverse of the resonance width. The readers may consult Ref.[13] for the details.

4.1.a Top Quark 3-Momentum Distribution

In this subsection we present the formula for the top quark 3-momentum distribution including all the $O(\alpha_s)$ corrections. There are two processes which contribute to the $t\bar{t}$ production cross section up to $O(\alpha_s)$ in the threshold region, namely, $e^+e^- \to bW^+\bar{b}W^-$ and $e^+e^- \to bW^+\bar{b}W^-g$. The top quark 3-momentum distribution is calculated as the sum of the $bW^+\bar{b}W^-$ cross section and the infra-red part of the real gluon emission cross section. The latter is calculated for the kinematical configurations where the gluon jet is indistinguishable from the b and/or $\bar{b}$ jet by appropriately defining the "top" momentum. The definition of the "top" momentum and the relevant cuts imposed are explained in the second half of Subsection 3.2.e.

Thus, the top quark 3-momentum distribution up to the next-to-leading order is given by

$$\mathcal{D}_t(E, |\mathbf{p}|, \cos\theta; y) = \frac{d\sigma_{t\bar{t}}}{d|\mathbf{p}|d\cos\theta} + \frac{d\sigma_{t\bar{t}g}}{d|\mathbf{p}|d\cos\theta} \tag{4.1.2}$$

$$= \frac{3\alpha^2}{2m_t^4}\frac{\Gamma_\Theta(E, \mathbf{p})}{2} \cdot |\mathbf{p}|^2(T_0 + T_1\cos\theta). \tag{4.1.3}$$

The distribution is a function of E, $|\mathbf{p}|$, $\cos\theta$, and y. Here, $E = \sqrt{s} - 2m_t$ is the c.m. energy measured from the threshold; $\mathbf{p}$ denotes the 3-momentum of top quark and θ represents the polar angle of top momentum $\mathbf{p}$ measured from the electron beam direction; y is the cut imposed on the bg and $\bar{b}g$ invariant masses normalized by m_t. (See subsection 3.2.e.)

In eq. (4.1.3), we have parametrized the spherically symmetric distribution and the $\cos\theta$ distribution as T_0 and T_1, respectively. The phase space volume $|\mathbf{p}|^2\Gamma_\Theta(E, \mathbf{p})$ together with an appropriate coefficient is factored out explicitly, where the running toponium width $\Gamma_\Theta(E, \mathbf{p})$ is given in terms of the top quark width Γ_t:

$$\frac{\Gamma_\Theta(E, \mathbf{p})}{2} = \Gamma_t\left[1 + \tilde{\eta}_1\left(\frac{E}{m_t}\right) - \tilde{\eta}_2\left(\frac{\mathbf{p}^2}{m_t^2}\right)\right] \tag{4.1.4}$$

with

$$\tilde{\eta}_1 = 3 \cdot \frac{1+r+2r^2}{1+r-2r^2}, \quad \tilde{\eta}_2 = \frac{1}{6} \cdot \frac{13+13r+46r^2}{1+r-2r^2}, \tag{4.1.5}$$

and

$$r = \frac{m_W^2}{m_t^2}. \tag{4.1.6}$$

Here, the top quark width including $O(\alpha_s)$ corrections is given by[30,31,32]

$$\Gamma_t = \Gamma_t^0 \left\{ 1 - \frac{C_F \alpha_s}{2\pi} h(r) \right\} \tag{4.1.7}$$

with

$$\Gamma_t^0 = \frac{G_F}{\sqrt{2}} \frac{m_t^3}{8\pi} (1+2r)(1-r)^2, \tag{4.1.8}$$

$$\begin{aligned} h(r) = {} & \pi^2 + 2\mathrm{Li}_2(r) - 2\mathrm{Li}_2(1-r) \\ & + [2(5+4r)(1-r)^2 \log(1-r) + 4(1+r)(1-2r) r \log r \\ & - (1-r)(5+9r-6r^2)] / [2(1-r)^2(1+2r)], \end{aligned} \tag{4.1.9}$$

and the color factor $C_F = 4/3$. The distributions T_0 and T_1 are obtained from the corresponding terms given in Subsection 3.2.e, which can be summarized as follows.

Spherically Symmetric Term

The spherically symmetric term T_0 is obtained as the sum of $T_0^{(VV)}$, $T_0^{(FI)}$, and $T_0^{(RE)}$:

$$\begin{aligned} T_0 = {} & \left[\left(-\frac{2}{3} + \chi g_V^t g_V^e \right)^2 + \chi^2 (g_V^t)^2 (g_A^e)^2 \right] \\ & \times \left[\left\{ 1 - \frac{4C_F\alpha_s}{\pi} - \frac{C_F\alpha_s}{2\pi} \cdot 2h_{bW_g}(y;r) \right\} |\tilde{G}(\mathbf{p};E)|^2 \right. \\ & \left. + C_F \cdot 4\pi\alpha_s \int \frac{d^3\mathbf{q}}{(2\pi)^3} \frac{1}{|\mathbf{k}|^3} 2\,\mathrm{Im}[\tilde{G}^*(\mathbf{q};E)\,\tilde{G}(\mathbf{p};E)] \cdot \frac{\pi}{2} \right]. \end{aligned} \tag{4.1.10}$$

$\cos\theta$ Term

The term proportional to $\cos\theta$, T_1, is obtained as the sum of $T_1^{(VA)}$ and $T_1^{(FI)}$:

$$\begin{aligned} T_1 = {} & \left(-\frac{2}{3} \chi g_A^e g_A^t + 2\chi^2 g_A^e g_V^e g_A^t g_V^t \right) \cdot \frac{|\mathbf{p}|}{m_t} \cdot 2\mathrm{Re}[\tilde{F}^*(\mathbf{p};E)\,\tilde{G}(\mathbf{p};E)] \\ & + 2\chi g_A^e g_V^t \left(-\frac{2}{3} + \chi g_V^e g_V^t \right) \cdot \kappa \cdot C_F \cdot 4\pi\alpha_s \\ & \times \int \frac{d^3\mathbf{q}}{(2\pi)^3} \frac{1}{|\mathbf{k}|^3} \frac{\mathbf{p}\cdot\mathbf{k}}{|\mathbf{p}|\,|\mathbf{k}|} 2\,\mathrm{Re}[\tilde{G}^*(\mathbf{q};E)\,\tilde{G}(\mathbf{p};E)]. \end{aligned} \tag{4.1.11}$$

In the above expressions, $\mathbf{k} = \mathbf{q} - \mathbf{p}$. It is understood that the principal value is taken in the loop integral in the second term of (4.1.11) as $\mathbf{q} \to \mathbf{p}$. $C_F = 4/3$ is the color factor, and $\kappa = (1-2r)/(1+2r)$ with $r = m_W^2/m_t^2$. The couplings associated with $e^+e^-Z^0$ and $t\bar{t}Z^0$ vertices are given by

$$g_V^e = -\tfrac{1}{2} + 2\sin^2\theta_W, \quad g_A^e = -\tfrac{1}{2}, \tag{4.1.12}$$

$$g_V^t = \tfrac{1}{2} - \tfrac{4}{3}\sin^2\theta_W, \quad g_A^t = \tfrac{1}{2}, \tag{4.1.13}$$

while the ratio of photon and Z^0 propagators with an appropriate normalization factor is defined as

$$\chi = \frac{1}{4\sin^2\theta_W \cos^2\theta_W} \frac{s}{s - m_Z^2}\bigg|_{s=4m_t^2}. \tag{4.1.14}$$

The S-wave and P-wave Green's functions, $\tilde{G}(\mathbf{p};E)$ and $\tilde{F}(\mathbf{p};E)$, are determined by solving the inhomogeneous Schrödinger equation in the coordinate space, and then taking their Fourier transforms[1]:

$$\left[-\frac{\nabla^2}{m_t} + V_{QCD}(r) - \left(E + i\frac{\Gamma_\Theta}{2} \right) \right] G(\mathbf{x};E) = \delta^3(\mathbf{x}), \tag{4.1.15}$$

$$\tilde{G}(\mathbf{p};E) = \int d^3\mathbf{x}\, e^{-i\mathbf{p}\cdot\mathbf{x}} G(\mathbf{x};E), \tag{4.1.16}$$

and

$$\left[-\frac{\nabla^2}{m_t} + V_{QCD}(r) - \left(E + i\frac{\Gamma_\Theta}{2} \right) \right] F^k(\mathbf{x};E) = -i\partial^k \delta^3(\mathbf{x}), \tag{4.1.17}$$

$$p^k\, \tilde{F}(\mathbf{p};E) = \int d^3\mathbf{x}\, e^{-i\mathbf{p}\cdot\mathbf{x}} F^k(\mathbf{x};E). \tag{4.1.18}$$

[1]The method to obtain $\tilde{G}(\mathbf{p};E)$ directly by solving the Schrödinger equation in momentum space has also been developed.[14]

We use the two-loop improved QCD potential given in Appendix C for $V_{QCD}(r)$. The technical details of the method for finding Green's functions are given in Refs.[10,13,16].

The partial decay width of top quark for $t \to bWg_{vis}$ is denoted as

$$\Gamma[t \to bWg_{vis}]_{(p_b+p_g)^2>m_t^2 y} = \Gamma_t^0 \times \frac{C_F \alpha_s}{2\pi} h_{bWg}(y;r) \tag{4.1.19}$$

with

$$\begin{aligned} h_{bWg}(y;r) = 2\Big[&\mathrm{Li}_2(x_+) - \mathrm{Li}_2(x_-) - \mathrm{Li}_2\left(\tfrac{x_+}{1-r}\right) + \mathrm{Li}_2\left(\tfrac{x_-}{1-r}\right) - \tfrac{1}{2}\log\tfrac{y}{(1-r)^2}\log\tfrac{x_+}{x_-}\Big] \\ &+\Big[-2r(1+r)(1-2r)\log\tfrac{1-x_+}{1-x_-} + (x_+ - x_-)(5+7r-8r^2+y) \\ &-\tfrac{1}{2}(1+2r)\{7(1-r)^2 + 4(1-r)y + y^2\}\log\tfrac{x_+}{x_-}\Big] / \{(1-r)^2(1+2r)\}. \end{aligned} \tag{4.1.20}$$

The visible gluon (g_{vis}) is the gluon which can be seen as a separate jet, and is defined by the cut $(p_b + p_g)^2 > m_t^2 y$. In (4.1.20), x_+ and x_- ($x_+ > x_-$) are defined as the two solutions to the quadratic equation, $x^2 - (1 - r + y)x + y = 0$.

Noting that the S-wave Green's function $\tilde{G}(\mathbf{q}; E)$ is only dependent on $|\mathbf{q}|$, the angular part of the loop integrations $\int \frac{d^3\mathbf{q}}{(2\pi)^3}$ can be performed analytically in the formulas for T_0 and T_1, and they may be reduced to the one-parameter integrals using the following formulas:

$$\int \frac{d^3\mathbf{q}}{(2\pi)^3} \frac{1}{|\mathbf{k}|^3} f(q) = \frac{1}{4\pi^2 p}\int_0^\infty dq\; w_0(q/p)\, f(q), \tag{4.1.21}$$

$$\int \frac{d^3\mathbf{q}}{(2\pi)^3} \frac{1}{|\mathbf{k}|^3} \frac{\mathbf{p}\cdot\mathbf{k}}{|\mathbf{p}|\,|\mathbf{k}|} f(q) = \frac{1}{4\pi^2 p}\int_0^\infty dq\; w_1(q/p)\, f(q), \tag{4.1.22}$$

with

$$w_0(x) = x\left[\frac{1}{|x-1|} - \frac{1}{x+1}\right], \tag{4.1.23}$$

$$w_1(x) = \frac{1}{2}\left[\mathrm{Pr.}\frac{1}{x-1} + \frac{2x+1}{x+1} - x\log\left|\frac{x+1}{x-1}\right|\right], \tag{4.1.24}$$

for any function $f(q)$ and $q = |\mathbf{q}|$, $p = |\mathbf{p}|$.

4.1.b Total Cross Section

The total cross section can be obtained from the differential cross sections given in the previous subsection by integrating over the top momentum after setting[2] $y = y_{max} = (1-\sqrt{r})^2$. Then, noting that $h_{bWg}(y_{max}; r) = 0$, one finds

$$\sigma_{tot} = \frac{3\alpha^2}{2m_t^4}\int_0^\infty d|\mathbf{p}|\;\Gamma_\Theta(E,\mathbf{p})\;|\mathbf{p}|^2 T_0 \tag{4.1.25}$$

$$\simeq \frac{3\pi^2\alpha^2}{m_t^4}\left[\left(-\frac{2}{3} + \chi g_V^t g_V^e\right)^2 + \chi^2 (g_V^t)^2 (g_A^e)^2\right] \times\left(1 - \frac{4C_F\alpha_s}{\pi}\right)\int\tfrac{d^3\mathbf{p}}{(2\pi)^3}\,|\tilde{G}(\mathbf{p};E)|^2\,\Gamma_\Theta(E,\mathbf{p}). \tag{4.1.26}$$

The contribution from the final state interaction diagrams canceled out altogether as expected in Subsection 3.2.d.

Using the unitarity relation between the Green's functions defined by eqs. (4.1.15) and (4.1.16),

$$2\,Im\,G(\mathbf{x}=0;E) = \int \tfrac{d^3\mathbf{p}}{(2\pi)^3}\,|\tilde{G}(\mathbf{p};E)|^2\,\Gamma_\Theta(E,\mathbf{p}), \tag{4.1.27}$$

one obtains the formula for the total cross section,

$$\sigma_{tot}(e^+e^- \to t\bar{t}) = \frac{6\pi^2\alpha^2}{m_t^4}\left[\left(-\frac{2}{3} + \chi g_V^t g_V^e\right)^2 + \chi^2 (g_V^t)^2 (g_A^e)^2\right] \times\left(1 - \frac{4C_F\alpha_s}{\pi}\right)\mathrm{Im}\,G(\mathbf{x}=0; E=\sqrt{s}-2m_t). \tag{4.1.28}$$

Therefore, the total cross section is obtained from the imaginary part of the Green's function at the origin, $\mathrm{Im}\,G(\mathbf{x}=0; E=\sqrt{s}-2m_t)$. The above formula has the identical form as that proposed by Fadin and Khoze[2], and later improved in Refs.[10,13], which were derived via the optical theorem. Here, the main reason we obtained the same simple form is because of the vanishing of the contributions from the final state interaction diagrams.

[2] This corresponds to the maximum invariant mass of bg from the t-quark at rest. Incidentally, the cross section from other kinematical region, $d\sigma_{t\bar{t}g}^{(WA)}$, swiftly reduces as $y \to y_{max}$; see (3.2.86).

The unitarity relation between the Green's functions, eq. (4.1.27), can be shown directly using the definition

$$G(\mathrm{x};E) = \langle \mathrm{x} | \frac{-1}{E - H + i\Gamma_\Theta/2} | \mathrm{x}' = 0 \rangle , \tag{4.1.29}$$

and the operator identity

$$2Im\frac{-1}{E - H + i\Gamma_\Theta/2} = \frac{-1}{E - H - i\Gamma_\Theta/2} \cdot \Gamma_\Theta \cdot \frac{-1}{E - H + i\Gamma_\Theta/2} . \tag{4.1.30}$$

The relation (4.1.27) then follows by taking the $\mathrm{x} = \mathrm{x}' = 0$ matrix element and by inserting the complete set of the momentum eigenstates. It should be noted that the identity (4.1.27) holds exactly even when Γ_Θ depends on E and $\mathrm{p} = -i\nabla$. We see the explicit appearance of the toponium width Γ_Θ on the right-hand-side of (4.1.27), rather than just in the denominator of $\tilde{G}(\mathrm{p};E)$. This is related to the phase space volume in the differential cross section formula eq. (4.1.26). It is, therefore, important to keep the order p^2/m_t^2 terms in Γ_Θ in the evaluation of $Im\, G(0;E)$. (See discussion in Chapter 6.)

4.2 Total Cross Section and Momentum Distribution

Using the formulas obtained in the previous section, we calculate both total cross section and differential cross sections in the threshold region including full next-to-leading order corrections. In Subsection 4.2.a, we discuss the dependence of the total cross section σ_{tot} on the physical parameters of the Standard Model, m_t, and $\alpha_s(m_Z)_{\overline{\mathrm{MS}}}$. In Subsection 4.2.b we study the top quark momentum distribution $d\sigma/d|\mathrm{p}|$. The main structures of the cross sections are determined by the leading Coulombic enhancement, and hence they exhibit strong dependences on both m_t and α_s. The asymmetric distribution of top quark will be closely investigated in the next section. The same value of $\alpha_s = \alpha_s(m_Z)$ is used for all the next-to-leading order corrections except for the QCD potential. (hard gluon correction, QCD correction to Γ_t, and final state interaction) We set $\alpha = 1/128$, $\sin^2\theta_W = 0.23$, $m_Z = 91.2$ GeV and $m_W = 80.6$ GeV in our numerical examples. We note that all figures presented in this section are based on the calculation of essentially

one diagram for $e^+e^- \to t\bar{t} \to bW^+\bar{b}W^-$ including non-trivial QCD corrections up to the next-to-leading order. (See Subsection 3.2.a.) Other electroweak diagrams which contribute to the process $e^+e^- \to bW^+\bar{b}W^-$ may be added later as small backgrounds. We give discussion on this point in Chapter 6. In order to make our theoretical predictions clear, we do not take account of initial state radiation effects. Studies including both initial state radiation and beamstrahlung effects have been presented elsewhere [17,18].

4.2.a Total Cross Section

We calculate the total cross section using the formula given in (4.1.28). The essential part is contained in the imaginary part of the Green's function, which may be written as

$$\mathrm{Im}\, G(\mathrm{x}=0; E = \sqrt{s} - 2m_t) \simeq -\mathrm{Im} \sum_n \frac{|\psi_n(0)|^2}{E - E_n + i\Gamma_n/2}. \tag{4.2.1}$$

Here, $E = \sqrt{s} - 2m_t$ is the energy measured from the threshold. $\psi_n(\mathrm{x})$ is the wave function of the n-th resonance state, and E_n and Γ_n denote its energy level and width, respectively. One sees the presence of the resonance structure in the energy dependence of the Green's function.

In Figs. 4.1(a), (b), (c) are shown the total cross sections near threshold for $m_t =$ 100, 150, 200 GeV, respectively, for three values of $\alpha_s(m_Z)_{\overline{\mathrm{MS}}}$; 0.11, 0.12, and 0.13. As m_t increases, the resonance structure is smeared out, since the top quark width Γ_t increases rapidly. ($\Gamma_t = 0.085, 0.80, 2.2$ GeV, respectively for $m_t = 100, 150, 200$ GeV). Also, the peak height decreases as it is proportional to Γ_t^{-1}. As top quark becomes short-lived, the resonances acquire less enhancement by the exchange of gluons before they decay. In each figure, we find that the resonance peaks shift to lower energies and its height is increased for larger α_s. This is because the resonance levels are lowered by the larger binding energy, and the wave functions of the resonance states at the origin, $\psi_n(0)$, grow at the same time.

In order to examine the sensitivity of the threshold cross section to the short

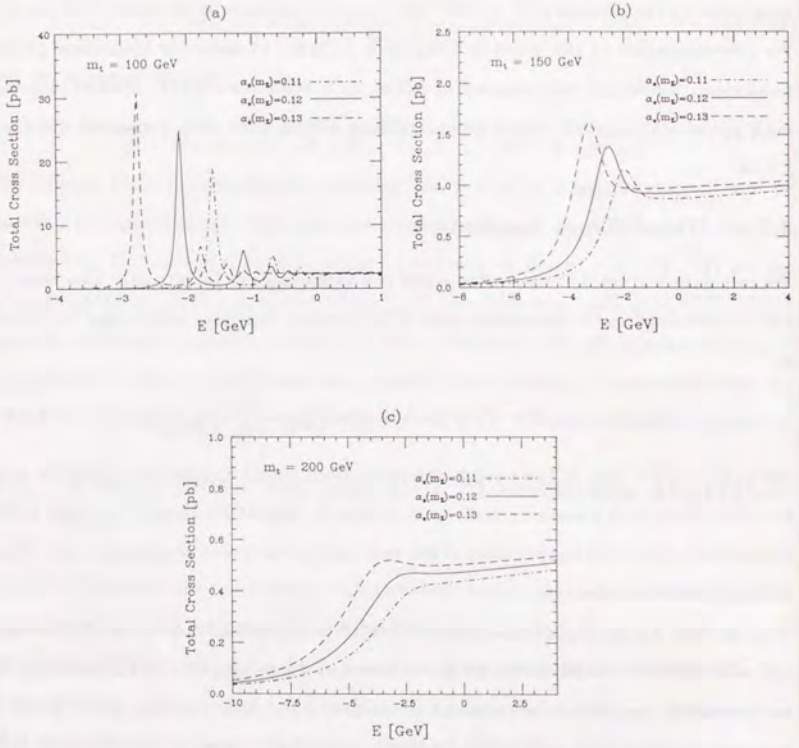

Figure 4.1: (a) The total cross sections versus energy, $E = \sqrt{s} - 2m_t$, for $m_t = 100$ GeV. $\alpha_s(m_Z)_{\overline{\rm MS}} = 0.11, 0.12, 0.13$ for the dotdashed, solid, and dashed lines, respectively. (b) The same as (a) but for $m_t = 150$ GeV. (c) The same as (a) but for $m_t = 200$ GeV.

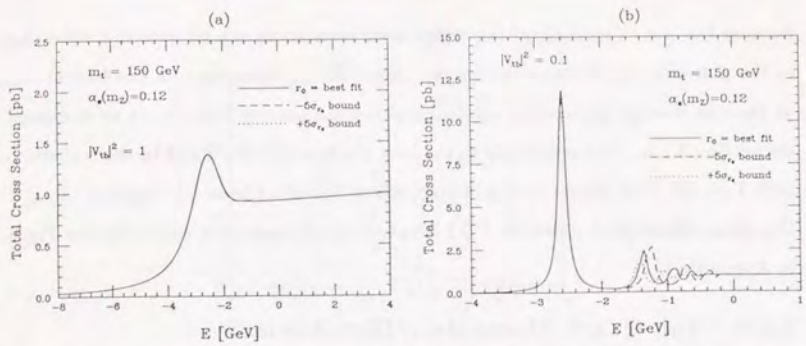

Figure 4.2: (a) The solid line is the prediction of the QCD potential with the best fit parameters. The dotted and dashed lines are obtained by shifting the parameter r_0 by five standard deviations upwards and downwards, respectively. (b) The same as (a) but for $|V_{tb}|^2 = 0.1$.

distance part of the potential, we show in Fig. 4.2(a) the total cross section for $m_t = 150$ GeV with our QCD potential at $\alpha_s(m_Z)_{\overline{\rm MS}} = 0.12$ by a solid line. Also shown by dashed and dotted lines are the predictions of the potentials with the same short distance behavior but with their intermediate distance part modified by shifting the parameter r_0 by five standard deviations away from its optimal value. The parameter r_0 determines the shape of the potential in the intermediate region which is constrained by the charmonium and bottomonium data.[3] The near degeneracy of the two curves demonstrates well that the short distant part of the potential essentially determines the threshold cross section. This is exactly what has been predicted by Fadin and Khoze [2], as a consequence of the large top quark decay width.

In order to study the effect of the top quark decay width, we show in Fig. 4.2(b) the same total cross section curves for $m_t = 150$ GeV, but with an artificially reduced top quark decay width ($\Gamma_t = 0.08$ GeV) by setting $|V_{tb}|^2 = 0.1$. The predictions of the three potentials with a common short distance behavior still agree well for the lowest resonance structure but they start deviating significantly for higher levels. It is

[3] See Appendix C where the dashed lines in Fig. C.2 show the range of the potential covered by the above change of the parameter r_0. The three potentials differ significantly at $r \gtrsim 0.5\text{GeV}^{-1}$.

because the wave functions of the higher level resonances extend over the wider region in the potential, or, because the momentum of the exchanged gluon can become small as the c.m. energy approaches the threshold in the narrow width limit as discussed in Subsection 3.1.b. This sensitivity to the long distance physics is lost in the realistic case with $\Gamma_t = 0.8$ GeV shown in Fig. 4.2(a), where the effect from the region $r \cdot \Gamma_t \gtrsim 1$ of the phenomenological potential $V(r)$ is cut off by the smearing effect[28]; see Fig. C.2 in Appendix C.

4.2.b Top Quark Momentum Distribution

Differential cross sections for the top quark pair production process may be calculated using the formula

$$d\sigma(e^+e^- \to t\bar{t} \to bW^+\bar{b}W^-) = \frac{1}{2s}\overline{\Sigma}\int d\Phi_4(bW^+\bar{b}W^-)|T_{fi}|^2\,, \tag{4.2.2}$$

where the matrix element T_{fi} is given in eq. (3.2.27), and also by adding to the above cross section the infra-red part of the cross sections for the real gluon emission process. There may be several choices for which differential cross sections one would investigate in order to extract the information on QCD interaction. We first identify the quantity which is most sensitive to the QCD interaction in the differential cross sections.

We note that the information on the leading QCD binding effects in the $t\bar{t}$ system is contained in the S-wave Green's function $\tilde{G}(\mathrm{p}; E)$ that appears in the $t\bar{t}V$ vector vertex; see eq. (3.2.12). Writing

$$\tilde{G}(\mathrm{p}; E) \simeq -\sum_n \frac{\phi_n(\mathrm{p})\psi_n^*(0)}{E - E_n + i\Gamma_n/2}\,, \tag{4.2.3}$$

where $\psi_n(\mathrm{x})$ is the wave function of the n-th resonance state, and $\phi_n(\mathrm{p})$ is its Fourier transform, we see that the energy (E) dependence of $\tilde{G}(\mathrm{p}; E)$ is essentially the same as for the total cross section, which is proportional to $Im\, G(0; E)$. On the other hand, its p-dependence is given by $\phi_n(\mathrm{p})$, the wave functions of the resonance states in momentum space. Thus, the scale of the E-dependence of $\tilde{G}(\mathrm{p}; E)$ is set by $\Delta E \sim \alpha_s^2 m_t$ and Γ_t, while that of the p-dependence is set by $\Delta|\mathrm{p}| \sim \alpha_s m_t$. Therefore, it is best to

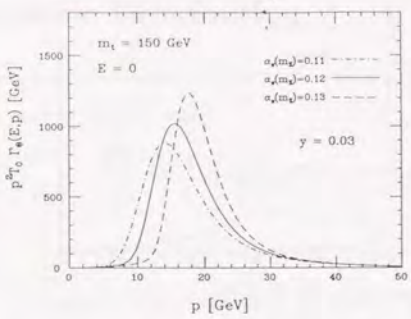

Figure 4.3: $\mathrm{p}^2 T_0 \Gamma_\Theta(E, \mathrm{p})$ versus $|\mathrm{p}|$ for $m_t = 150\,\mathrm{GeV}$ and $E = \sqrt{s} - 2m_t = 0$. $\alpha_s(m_Z)_{\overline{\mathrm{MS}}} = 0.11$, 0.12, and 0.13 for the dotdashed, solid, and dashed lines, respectively.

look directly at the p-dependence of $\tilde{G}(\mathrm{p}; E)$, since this provides us with information independent of that from the total cross section, and also because its dependence on the strong binding effects extends over a wide range of the momentum $\sim \alpha_s m_t$. $t\bar{t}$ distribution is spherical in the leading order since only the S-wave states contribute. As the differential cross section contains $|\tilde{G}(\mathrm{p}; E)|^2$, it is possible to observe directly the $|\mathrm{p}|$-dependence of $|\tilde{G}(\mathrm{p}; E)|^2$ at a fixed energy $\sqrt{s} = 2m_t + E$: the leading $|\mathrm{p}|$-dependence of the cross section is easily obtained from the differential cross sections formulas (4.1.3) and (4.1.10) as

$$\frac{d\sigma}{d|\mathrm{p}|} = \frac{3\alpha^2}{m_t^4}\frac{\Gamma_\Theta(E, \mathrm{p})}{2} \cdot |\mathrm{p}|^2 T_0 \tag{4.2.4}$$

$$= \frac{3\alpha^2\Gamma_t}{m_t^4}\left[\left(-\frac{2}{3} + \chi g_V^t g_V^e\right)^2 + \chi^2 (g_V^t)^2 (g_A^e)^2\right] \cdot \mathrm{p}^2 |\tilde{G}(\mathrm{p}; E)|^2 \Gamma_\Theta(E, \mathrm{p})$$
$$+ (\text{next-to-leading order corrections}). \tag{4.2.5}$$

Fig. 4.3 shows the $|\mathrm{p}|$-dependence of T_0 multiplied by the phase space factor $\mathrm{p}^2\,\Gamma_\Theta(E, \mathrm{p})$ for $m_t = 150\,\mathrm{GeV}$ and $E = 0$. We use $y = 0.03$ for the cuts on the bg and $\bar{b}g$ invariant masses in all the calculations of top quark momentum distribution. The peak shifts to larger $|\mathrm{p}|$ as α_s increases. This is due to the increase of the binding

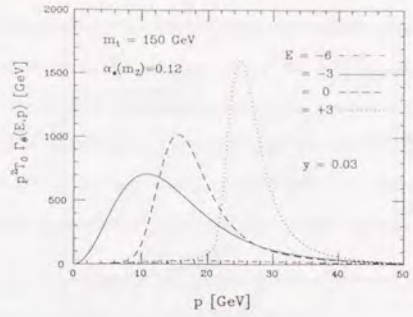

Figure 4.4: $\mathrm{p}^2 T_0 \Gamma_\Theta(E,\mathrm{p})$ versus $|\mathrm{p}|$ for $m_t = 150\,\mathrm{GeV}$ and $\alpha_s(m_Z)_{\overline{\mathrm{MS}}} = 0.12$. $E = \sqrt{s} - 2m_t = -6, -3, 0$, and $+3\,\mathrm{GeV}$ for the dotdashed, solid, dashed, and dotted lines, respectively.

energy, which contributes to the kinetic energy of the $t\bar{t}$ system. Also the peak height increases with growing α_s, because of the increase of $|\psi_n(0)|$ as in the case of the total cross section.

In Fig. 4.4, we show the $|\mathrm{p}|$-dependence of $\mathrm{p}^2 T_0 \Gamma_\Theta(E,\mathrm{p})$ at several energies. The distributions are given at four energies $E = \sqrt{s} - 2m_t = -6, -3, 0, +3$ GeV for $m_t =$ 150 GeV and $\alpha_s(m_Z)_{\overline{\mathrm{MS}}} = 0.12$. There is no resonance enhancement at $E = -6$ GeV, and the factor $\mathrm{p}^2 T_0 \Gamma_\Theta(E,\mathrm{p})$ is essentially flat there. A clear broad peak appears in the distribution at larger energies. The peak position shifts to larger $|\mathrm{p}|$ as the energy increases.

Thus, we see that the measurement of top quark momentum distribution would be useful in the determination of α_s. An accurate measurement of the $|\mathrm{p}|$ distribution would require a low beamstrahlung collider, a high resolution detector, and a good theoretical understanding of jet physics. This is certainly a challenge which is a worthy endeavor.

4.3 Asymmetric Distribution

One sees that the top quark 3-momentum distribution derived in 4.1.a exhibits the $\cos\theta$ distribution at the next-to-leading order:

$$\frac{d\sigma_{t\bar{t}}^{(asym)}}{d|\mathrm{p}|d\cos\theta} = \frac{3\alpha^2}{2m_t^4}\,\frac{\Gamma_\Theta(E,p)}{2}\,|\mathrm{p}|^2\,(T_1^{(VA)} + T_1^{(FI)})\,\cos\theta \tag{4.3.1}$$

with

$$T_1^{(VA)} = \left(-\frac{2}{3}\chi g_A^e g_A^t + 2\chi^2 g_A^e g_V^e g_A^t g_V^t\right)\cdot\frac{|\mathrm{p}|}{m_t}\cdot 2\mathrm{Re}[\tilde{F}^*(\mathrm{p};E)\,\tilde{G}(\mathrm{p};E)], \tag{4.3.2}$$

$$T_1^{(FI)} = 2\chi g_A^e g_V^t\left(-\frac{2}{3} + \chi g_V^e g_V^t\right)\cdot\kappa\cdot C_F\cdot 4\pi\alpha_s \times\int\frac{d^3\mathrm{q}}{(2\pi)^3}\,\frac{1}{|\mathrm{k}|^3}\,\frac{\mathrm{p}\cdot\mathrm{k}}{|\mathrm{p}|\,|\mathrm{k}|}\,2\,\mathrm{Re}[\tilde{G}^*(\mathrm{q};E)\,\tilde{G}(\mathrm{p};E)]. \tag{4.3.3}$$

Hence there appears forward-backward (FB) asymmetry in the top quark distribution near threshold at $O(\alpha_s)$. In this section we are concerned with the analyses of the FB-asymmetry and asymmetric top momentum distribution. It will be shown that the FB-asymmetry increases and becomes more sensitive to α_s for larger m_t. It is in contrast to the total cross section, which loses sensitivity to α_s due to the smearing effect by the large top quark width as m_t grows. Thus, the measurement of FB-asymmetry may allow an efficient cross-check to the measurement of α_s for a relatively heavy top quark. In Subsection 4.3.a, we discuss the origin of the asymmetric distribution. It is emphasized that the large widths of resonances give rise to the interference of the S-wave and P-wave states. Then we present the numerical analyses of the FB-asymmetry and momentum distribution in Subsection 4.3.b. One sees that there exists an interesting interplay between QCD and electroweak interactions, which gives rise to the FB-asymmetry even in the threshold region.

4.3.a Physical Origin

There are two terms, $T_1^{(VA)}$ and $T_1^{(FI)}$, which contribute to the asymmetric distribution of top quark as given in (4.3.2) and (4.3.3). See Fig. 4.5. These are the next-to-

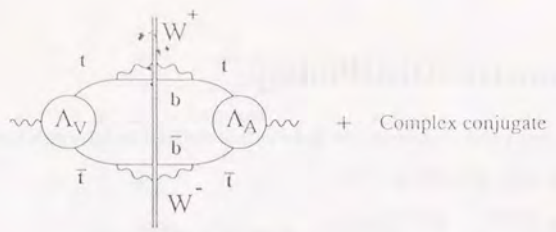

(a)

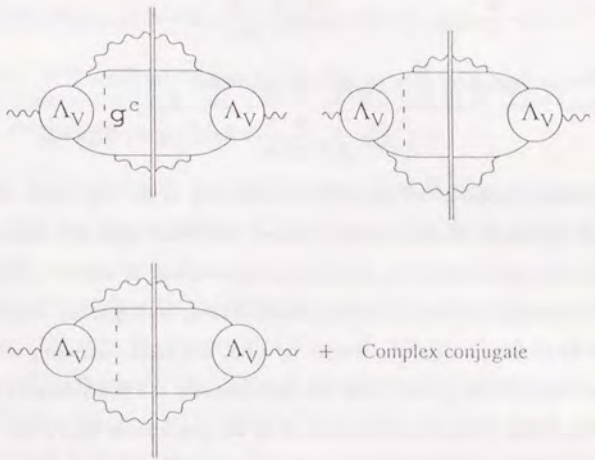

(b)

Figure 4.5: Diagrams which contribute to the asymmetric distributions, (a)for the VA term, and (b)for the FI term. Initial electron currents are omitted. $\Lambda_V(\Lambda_A)$ denotes the $t\bar{t}V$ vector (axial-vector) vertex, and dashed lines represent the Coulomb gluons.

leading order quantities themselves. The first term originates from the interference of the vector and axial-vector $t\bar{t}V$ vertices (VA term). In contrast to the charmonium and bottomonium resonances, the P-wave resonance states produced via $t\bar{t}Z^0$ axial coupling interfere with S-wave states due to the large top quark width, which gives rise to the FB-asymmetry. The second term stems from the interference of the leading S-wave amplitude and the final state interaction diagrams (FI term). The final state interaction diagrams which contribute to the FB-asymmetry are those with the one-Coulomb-gluon-exchange between t and $\bar{b}$ ($\bar{t}$ and b), and between b and $\bar{b}$, where b and $\bar{b}$ are the decay products of the $t\bar{t}$ pair produced via $t\bar{t}V$ *vector* coupling. Because the decay $t \to bW$ occurs via the $V-A$ interaction, it contributes to the FB-asymmetry. It turns out that, in most cases, the main contribution to the FB-asymmetry comes from the VA term ($0 \sim 10\%$), which exhibits non-trivial energy dependence, while the contribution from the FI term is typically small ($0 \sim 1\%$) and the energy dependence is weak. Therefore, it is important to understand the behavior of the VA term in order to understand the overall structures of the FB-asymmetry in the threshold region. We will first concentrate on the physical origin of the contribution from the VA term. Later we will briefly discuss the effect of FI term as a small correction to the former contribution.

1. The Effect of $t\bar{t}Z^0$ Axial-Vector Coupling

We briefly discuss the effect of the $t\bar{t}Z^0$ axial-vector coupling of top quark at the $t\bar{t}$ threshold region. It is emphasized that the large top quark width allows the interference between S-wave and P-wave resonance states, giving rise to the forward-backward asymmetry even in the threshold region.

In the $e^+e^- \to t\bar{t}$ process, the $t\bar{t}$-pair produced via $t\bar{t}V$ ($V = \gamma, Z^0$) vector vertex has spin-parity $J^P = 1^-$, whereas that produced via $t\bar{t}Z^0$ axial-vector vertex has $J^P = 1^+$ in the massless electron limit. Thus, the vector vertex is associated with S and D-wave resonance states, and the axial-vector vertex with P-wave states.

The axial-vector coupling is suppressed by a power of β near threshold as can be

seen from the non-relativistic form of the coupling

$$\bar{t}\gamma^k\gamma_5 t Z^k \simeq \frac{1}{m_t}\epsilon^{ijk}\chi_1^\dagger\sigma^i\chi_2 p^j Z^k + O(p^2), \tag{4.3.4}$$

where χ_1 and χ_2 denote two-component spin wave functions of t and $\bar{t}$, respectively, and 2p is the relative 3-momentum between t and $\bar{t}$. Compare this with the VA term, eq. (4.3.2), where the factor $|\mathrm{p}|/m_t \simeq \beta$ is explicitly factored out.

In general, S-wave resonance states and P-wave resonance states have different energy spectra. However, the widths of resonances grow rapidly as m_t increases, and they become so large that S-wave and P-wave resonance states start to interfere for $m_t \gtrsim 100$ GeV.

Let us state it more explicitly. At the lowest order, it is expected that the toponium resonances exhibit the Coulomb level spectra because the binding effect due to gluon exchanges can be regarded as Coulombic interaction[2]. Then, the level gaps typically become of the order $\alpha_s^2 m_t \sim 1$ GeV, and the S-wave states and P-wave states are degenerate in this approximation. There will be S-wave states corresponding to the principal quantum number $n = 1, 2, 3, \ldots$, and P-wave states for $n = 2, 3, 4, \ldots$ If we consider the higher order corrections, the QCD potential deviates from the Coulomb potential, and the S-wave states and P-wave states are no longer degenerate, with typical level splitting of the order $\alpha_s^3 m_t \sim 0.1$ GeV.

On the other hand, each resonance state has a width almost twice that of top quark $\Gamma_t \sim G_F m_t^3/8\sqrt{2}\pi$, which grows rapidly as m_t increases. For instance, $\Gamma_t \simeq 0.1$ GeV for $m_t = 100$ GeV, and $\Gamma_t \simeq 1$ GeV for $m_t = 150$ GeV. If we fix the c.m. energy at the $n = 1$ resonance, where no corresponding P-wave resonance exists, the width and the level gap would become comparable for $m_t \gtrsim 150$ GeV. At $n \geq 2$ resonances, there would be larger interference effects. Thus, we anticipate from the above estimation that the interference would be significant at $n \geq 2$ resonances even for a light top quark, where the resonance structures are more distinct, and also at the $n = 1$ resonance for a relatively heavy top quark.

The P-wave amplitude being $O(\beta)$ at the threshold, its interference with S-wave

resonance states gives rise to $O(\beta) \simeq O(\alpha_s)$ correction to the leading S-wave contribution to the cross sections. Since this correction stems from the interference of the vector and axial-vector couplings, it is proportional to $\beta\cos\theta$, or, it gives rise to the FB-asymmetry at $O(\alpha_s)$. Meanwhile the effect of axial coupling to the total cross section is of $O(\alpha_s^2)$, which is beyond our scope [40].

2. The Effect of Final State Interaction Diagrams

As seen above, the effect of VA term increases as the top quark width grows. At the same time we have to consider the effect of FI term, which is also related to the decay of top quark. Here, we state very briefly the effect of this term on the asymmetric distribution.

Even though the FI term is associated only with the S-wave resonances, it contributes to the FB-asymmetry since the decay vertex for $t \to bW$ includes both vector coupling (V_{tbW}) and axial-vector coupling (A_{tbW}). Namely, the state represented by

$$A_{tbW}\, V_{tbW}\, \bar{\psi}\gamma^k\psi \,|\, 0\,\rangle \tag{4.3.5}$$

has the spin-parity $J^P = 1^+$, and hence gives rise to the asymmetric distribution upon interference with the leading S-wave amplitude. The $t\bar{t}$ pair forms S-wave resonances for the time scale $\sim \Gamma_t^{-1}$, when the decay occurs via $V-A$ interaction.

In fact it can be seen from the presence of the factor

$$\kappa = \frac{1-2r}{1+2r} \tag{4.3.6}$$

in eq. (4.3.3) that the FI term includes one A_{tbW} vertex associated with the decay process $t \to bW$. Here, $2r = 2m_W^2/m_t^2$ represents the ratio of the branching fraction of top quark into the transverse W (W_T) to that into longitudinal W (W_L). It is well known that the contribution of W_L dominates the top width for large m_t. As the produced b-quark is left-handed for $m_b = 0$, W_L and W_T project the different spin orientations of parent top quark with respect to the b-quark momentum. Hence, the $W_L + W_T$ is associated with the parity preserving sector, while $W_L - W_T$ is associated with the parity violating sector, in the decay process of non-relativistic top quark; see eq. (3.2.56).

One may note that the VA term is the term which becomes the zeroth order cross section in the open top region ($\beta \gg \alpha_s$), while the FI term remains the $O(\alpha_s)$ correction in this region. Thus, one would expect that even in the threshold region the contribution from the VA term increases as the c.m. energy is raised so that the weight of the FI term decreases comparatively.

Actual calculation of asymmetric distribution shows that, in most cases, the contribution from the FI term is small compared to that from the VA term. This is in part because of the smallness of the factor κ, and in part because the main part in the loop integral in (4.3.2) cancels out by taking the principal value. The decay fractions of top quark into W_L and W_T balance for $m_t \simeq 110$ GeV, and the factor κ vanishes for this top mass. The FI term adds a positive contribution to the FB-asymmetry for $m_t < 110$ GeV and a negative contribution for $m_t > 110$ GeV at the level of $\sim 1\%$, while its energy dependence is weak.

We will give a close examination on the separate contribution from each term of eq. (4.3.2) in Chapter 5. There, all the effects of $O(\alpha_s)$ corrections are investigated separately. Meanwhile, in the next subsection we will concentrate on the total contribution to the asymmetric distribution.

4.3.b FB-Asymmetry and Momentum Distribution

In this subsection we calculate the forward-backward (FB) asymmetry and the momentum distribution of top quark which is proportional to $\cos\theta$ for the process $e^+e^- \to t\bar{t} \to bW^+\bar{b}W^-$. The axial couplings at $t\bar{t}Z^0$ and tbW vertices give rise to the $t\bar{t}$ distribution proportional to $\cos\theta$ at the next-to-leading order, which leads to the forward-backward (FB) asymmetry of the cross section. The FB-asymmetry below threshold (at the resonance peak) increases from 0 to $\sim 4\%$ as m_t is raised from 100 GeV to 200 GeV. The sensitivity to α_s is magnified for larger m_t. For instance, for $m_t = 200$ GeV, the asymmetry at the peak decreases from 5% to 2.5% as α_s is varied from 0.10 to 0.14. Also the asymmetry grows as the c.m. energy increases and exceeds 10% in the continuum

region. As the main contribution to the asymmetric distribution comes from the VA term, $T_1^{(VA)}$, in (4.3.2), it is convenient to interpret the behavior of the cross sections in terms of the S-wave and P-wave interferences in most of the following examples. The Green's functions are evaluated using the 2-loop improved QCD potential given in Appendix C in the Schrödinger equations. We note that all the analyses in this section do not include the effect of the initial state radiation.

Using the differential cross section formula given in eq. (4.3.2) and in Subsection 4.1.a, we may calculate the FB-asymmetry. We define the FB-asymmetry as

$$\Delta_{FB} = \frac{1}{\sigma_{tot}} \int_0^\Lambda d|\mathbf{p}| \left[\int_0^1 d\cos\theta - \int_{-1}^0 d\cos\theta \right] \mathcal{D}_t(E, |\mathbf{p}|, \cos\theta; y_{max}). \tag{4.3.7}$$

Substituting (4.1.3) into the above equation, we find

$$\Delta_{FB} = \int_0^\Lambda d|\mathbf{p}|\ |\mathbf{p}|^2 T_1\, \Gamma_\Theta(E,\mathbf{p}) \Big/ 2\int_0^\Lambda d|\mathbf{p}|\ |\mathbf{p}|^2 T_0\, \Gamma_\Theta(E,\mathbf{p})\Big|_{y=y_{max}}. \tag{4.3.8}$$

Here, we have restricted the $|\mathbf{p}|$-integration within $|\mathbf{p}| < \Lambda$, where the cut-off Λ is taken as

$$\Lambda^2 = \frac{1}{16m_t^2}(9m_t^2 - m_W^2)(m_t^2 - m_W^2). \tag{4.3.9}$$

For $|\mathbf{p}| > \Lambda$, there would be no allowed kinematical configuration such that either one of t or $\bar{t}$ remains on-shell, and that the other has the invariant mass larger than m_W^2, simultaneously. The phase space virtually vanishes in this region for $\sqrt{s} \simeq 2m_t$, or equivalently, the running toponium width vanishes, $\Gamma_\Theta(E,\mathbf{p}) = 0$ [13,41].

The energy dependences of Δ_{FB} together with the total cross sections are shown in Figs. 4.6(a)(b)(c) for $m_t = 100$, 150, and 200 GeV, respectively. In each figure, three curves correspond to $\alpha_s(m_Z) = 0.10, 0.12$, and 0.14. One sees that the FB-asymmetry below threshold (at the peak) almost vanishes for $m_t = 100$ GeV, and increases for larger m_t. This is because the top quark width Γ_t grows rapidly with m_t so that the overlap of S-wave and P-wave resonance states becomes more significant. In each figure, Δ_{FB} grows as E increases from the lowest lying resonance. This is because the interference

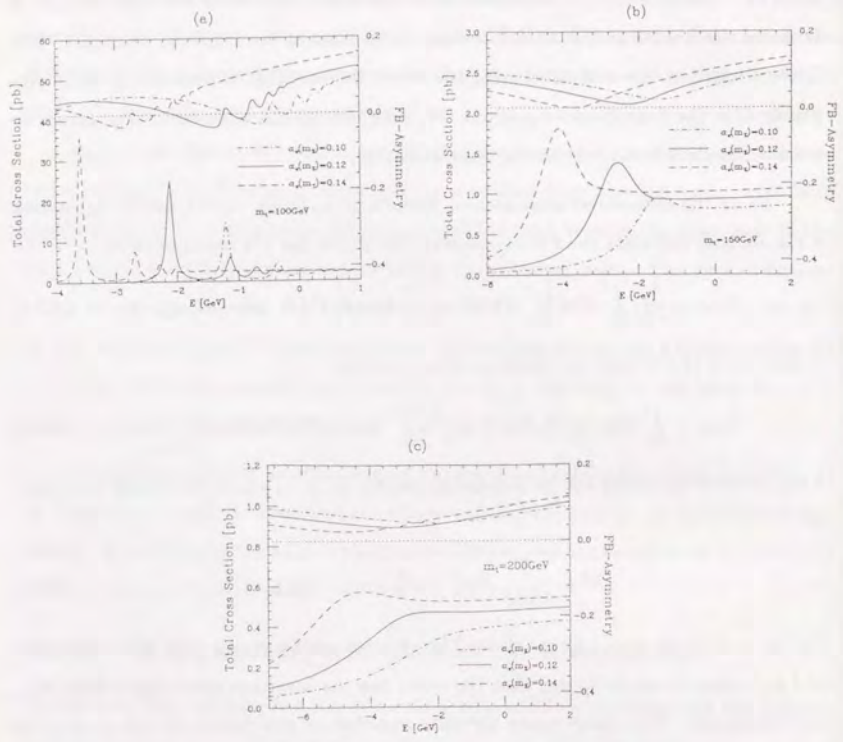

Figure 4.6: The total cross section σ_{tot} and the FB-asymmetry Δ_{FB} versus energy, $E = \sqrt{s} - 2m_t$. The left axis stands for the total cross section, and the right axis is for the FB-asymmetry. The dotted line shows the position of zero for the FB-asymmetry.

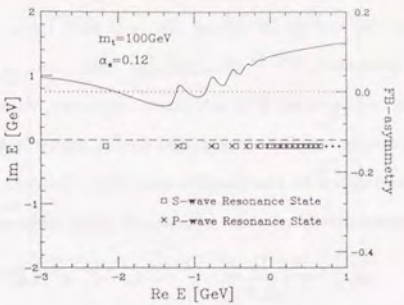

Figure 4.7: The positions of poles of $T_1^{(VA)}$ on the complex energy plane, together with the FB-asymmetry as a function of energy, $E = \sqrt{s} - 2m_t$. The boxes represent S-wave resonances, and the crosses represent P-wave resonances. The right axis is for the FB-asymmetry.

among the resonances becomes more severe in higher energies[2,9], since the resonance levels appear closer to one another. These curves include small contributions from the FI term which is positive for $m_t < 110$ GeV and negative for $m_t > 110$ GeV at the level of $\sim 1\%$. (See the next chapter.)

Fairly complex energy dependence of Δ_{FB} for $m_t = 100$ GeV, as well as milder behaviors for $m_t = 150$ GeV and $m_t = 200$ GeV, can be understood if we note the analytic structure of the VA term in the complex E-plane. In Fig. 4.7, we plot the position of poles of $T_1^{(VA)} \propto Re[\tilde{F}^*(\mathrm{p}; E)\tilde{G}(\mathrm{p}; E)]$ together with Δ_{FB} for $m_t = 100$ GeV and $\alpha_s(m_Z) = 0.12$; see eqs. (4.3.2) and (4.3.8). The squares represent the S-wave resonance states (1S, 2S,...), while the crosses represent P-wave states (1P, 2P,...).[1] P-wave states lie slightly below the corresponding S-wave states due to the running effect of strong coupling constant. P-wave states 'see' the long distance behavior of the QCD potential as compared to S-wave states,[2] and thus gains larger binding energies. The dense spectra above threshold ($E > 0$) give quasi-continuum cross sections[9].

[1] We follow the convention for lighter quarkonium resonances in naming the P-wave states. This differs, however, from the principal quantum number for the Coulomb levels; see subsection 4.3.a

[2] This "long distance" is still much shorter than the infrared QCD region $\sim \Lambda_{QCD}^{-1}$. See Figs. 4.9 and 4.10.

Let us increase the energy E along the real axis from below the lowest lying resonance. As E is increased, $T_1^{(VA)}$ changes sign each time E crosses over above the pole. Therefore, Δ_{FB} oscillates as E is increased. However, when the energy differences of resonance levels become small as compared to Γ_t, many levels begin to contribute, and $T_1^{(VA)}$ tends to be shifted in the positive direction. Indeed, the contribution of the VA term to the FB-asymmetry at some resonance peak behaves as

$$\Delta_{FB}^{(VA)} \propto \left(\frac{\Gamma_t}{\Delta E}\right)^2 \qquad \text{for} \quad \Gamma_t \ll \Delta E, \tag{4.3.10}$$

and

$$\Delta_{FB}^{(VA)} \propto \sqrt{\frac{\Gamma_t}{m_t}} \qquad \text{for} \quad \Gamma_t \gg \Delta E, \tag{4.3.11}$$

where ΔE represents the energy difference of the resonance levels. Eq. (4.3.10) shows that $\Delta_{FB}^{(VA)}$ increases as Γ_t^2 for small m_t. Meanwhile, eq. (4.3.11) implies that asymptotically Δ_{FB} will grow proportionally to m_t, since $\Gamma_t \propto m_t^3$ for $m_t \gg m_W$ [3]. Again, we note that the effect of FI term shifts Δ_{FB} in the positive direction for $m_t < 110$ GeV and in the negative direction for $m_t > 110$ GeV at the level of $\sim 1\%$, while this effect is weakly dependent on the c.m. energy E.

In Fig. 4.8, we show the m_t-dependence of Δ_{FB} evaluated at the c.m. energies corresponding to the position of the lowest lying peak that appears in the total cross section. The three curves are for $\alpha_s(m_Z)$=0.10, 0.12, and 0.14. For larger m_t, the peak tends to dissapear due to the smearing effect by the large top quark width. In this region, Δ_{FB} is evaluated at $E = -1.5, -2.6$, and -4.3 GeV for $\alpha_s(m_Z) = 0.10, 0.12$, and 0.14, respectively, which roughly correspond to the energies where Δ_{FB} is minimal, or, at the "shoulders" of the cross sections. (See Fig. 4.6(c).)

One sees that Δ_{FB} grows from nearly zero to $2 \sim 5\%$ as m_t is increased from 100 GeV to 200 GeV. This is because the top quark width grows rapidly in this m_t region (Γ_t=0.085 GeV for m_t=100 GeV, and Γ_t=2.2 GeV for m_t=200 GeV), so that the S-wave state and the P-wave state start to overlap, which gives rise to the interference term proportional to $\cos\theta$ in eq. (4.3.2). Therefore, Δ_{FB} is enhanced for larger m_t, and

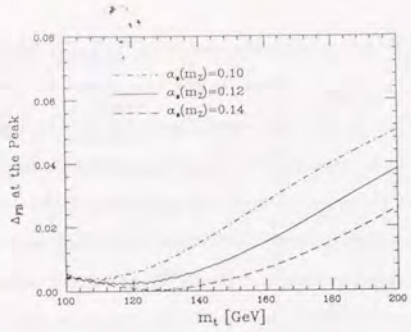

Figure 4.8: The FB-asymmetry evaluated at the first peak of total cross section versus top quark mass, for $\alpha_s(m_Z) = 0.10$ (dotdash), 0.12 (solid), and 0.14 (dash).

more feasible to be measured in experiments, while the total cross section decreases like $\sim 1/m_t^2$, as well as the peak cross section decreases due to the large top quark width.

The FB-asymmetry at the peak is also sensitive to $\alpha_s(m_Z)$: Δ_{FB} decreases as α_s increases. This is because the resonance levels spread apart from one another as well as their widths are reduced[3] for larger α_s, and thus the overlap of the S-wave and P-wave states decreases. Although cross sections are more enhanced for larger α_s, the enhancements tend to cancel in the denominator and numerator for the FB-asymmetry (4.3.7). The noticeable feature here is that the α_s-dependence of Δ_{FB} is magnified for a heavier top quark. (According to eq. (4.3.11), $\Delta_{FB}^{(VA)}$ would become independent of α_s asymptotically as $m_t \to \infty$. Nevertheless one sees that the sensitivity to α_s remains for $m_t \lesssim 200$ GeV.)

We are also concerned with the $t\bar{t}$ distributions, which can be investigated by using the differential cross section formula given by (4.1.3). $t\bar{t}$ distribution is spherical in the leading order, since only S-wave states contribute. The effects of $t\bar{t}Z^0$ and tbW axial-vector vertices give rise to the $\cos\theta$ term at $O(\alpha_s)$. The cuts on the bg and $\bar{b}g$ invariant masses are set as $y = 0.03$ in the following examples.

[3]The $O(\alpha_s)$ correction to the top quark width reduces the zeroth order width by about 10%; see eq. (4.1.7).

We show in Fig. 4.9 the $|\mathrm{p}|$-dependences of $|\mathrm{p}|^2 T_0\, \Gamma_\Theta(E,\mathrm{p})$ and $|\mathrm{p}|^2 T_1\, \Gamma_\Theta(E,\mathrm{p})$ for $m_t = 100$ GeV and $\alpha_s = 0.12$. Three figures correspond to the energies (a)at the first peak ($E = -2.12$ GeV), (b)at the second peak ($E = -1.14$ GeV), and (c)above threshold ($E = 1$ GeV). At $E = -2.12$ GeV, T_1 almost vanishes. T_0 exhibits the shape of the absolute square of the 1S resonance state wave function in the momentum space. At $E = -1.14$ GeV, T_0 shows the square of the 2S state wave function, while T_1 shows the product of the 2S state wave function and the 2P state wave function. At $E = 1$ GeV, where a number of resonance states contribute, the structure of the $t\bar{t}$ distribution is quite smeared, and T_1 is more enhanced. The peak of the distribution is shifted to higher $|\mathrm{p}|$ compared to $E = -2.12$ GeV and $E = -1.14$ GeV, since the kinetic energy of $t(\bar{t})$ is larger.

Similarly, the $|\mathrm{p}|$-dependences of $|\mathrm{p}|^2 T_0$ and $|\mathrm{p}|^2 T_1$ for $m_t = 150$ GeV are shown in Fig. 4.10, at the enregies (a)$E = -2.52$ GeV (first peak), (b)$E = -1$ GeV, and (c)$E = 1$ GeV. The structures of the $t\bar{t}$ distributions are smeared out compared to those of $m_t = 100$ GeV due to the larger top quark width.

Thus, Figs. 4.9 and 4.10 show that the effect of axial-vector couplings modifies the $t\bar{t}$ distribution significantly for large m_t, and at the higher c.m. energies.

In summary, the FB-asymmetry below threshold (at the lowest lying peak of the total cross section for $m_t \lesssim 150$ GeV) 'measures' the degree of overlap of S-wave states and P-wave states. It is essentially determined by the relative magnitude of the widths and the energy differences of the resonance levels, while it is insensitive to the normalization of the cross sections. This suggests that Δ_{FB} would be a stable quantity to the smearing effect by the initial state radiation. Quite generally, Δ_{FB} increases as the resonance widths increase or the binding energy decreases, since the major contribution to the FB-asymmetry stems from the interference of S-wave and P-wave states. The FB-asymmetry is more enhanced for larger m_t. In particular, its dependence on α_s is magnified for $150\mathrm{GeV} \lesssim m_t \lesssim 200$ GeV. This sensitivity may help determination of α_s for a relatively heavy top quark, since much of the resonance structures are smeared

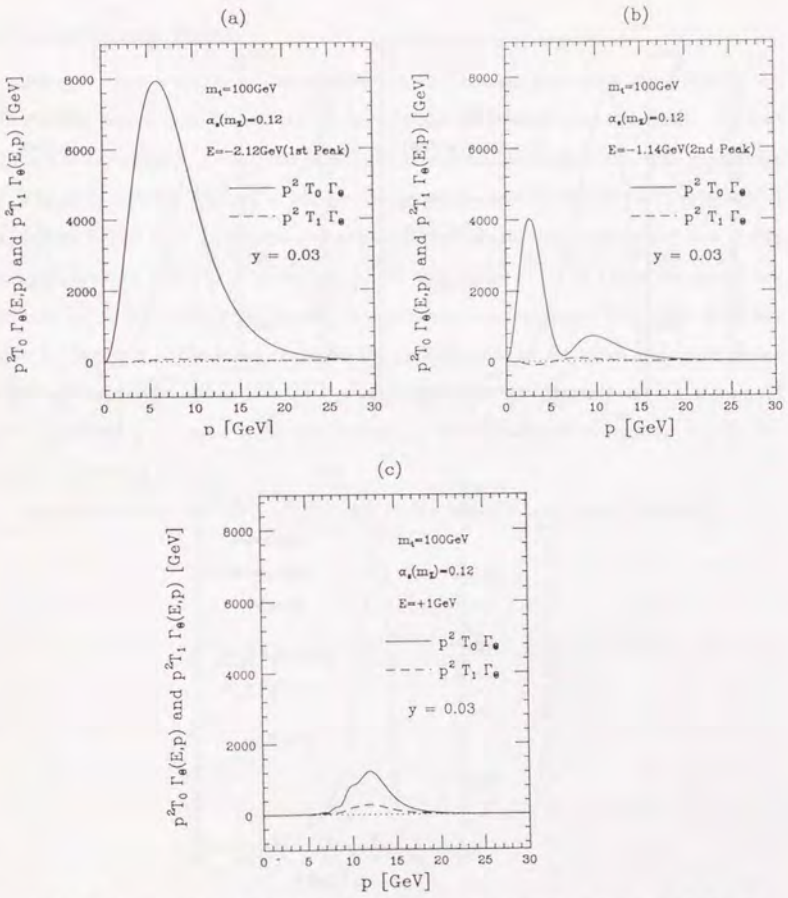

Figure 4.9: The comparison of the spherical distribution (solid) and the $\cos\theta$ distribution (dashed). The dotted line shows the position of zero. In each figure, the energy is taken as (a)$E = -2.12$GeV (at the first resonance peak), (b)$E = -1.14$GeV (at the second resonance peak), and (c)$E = +1$GeV (above threshold).

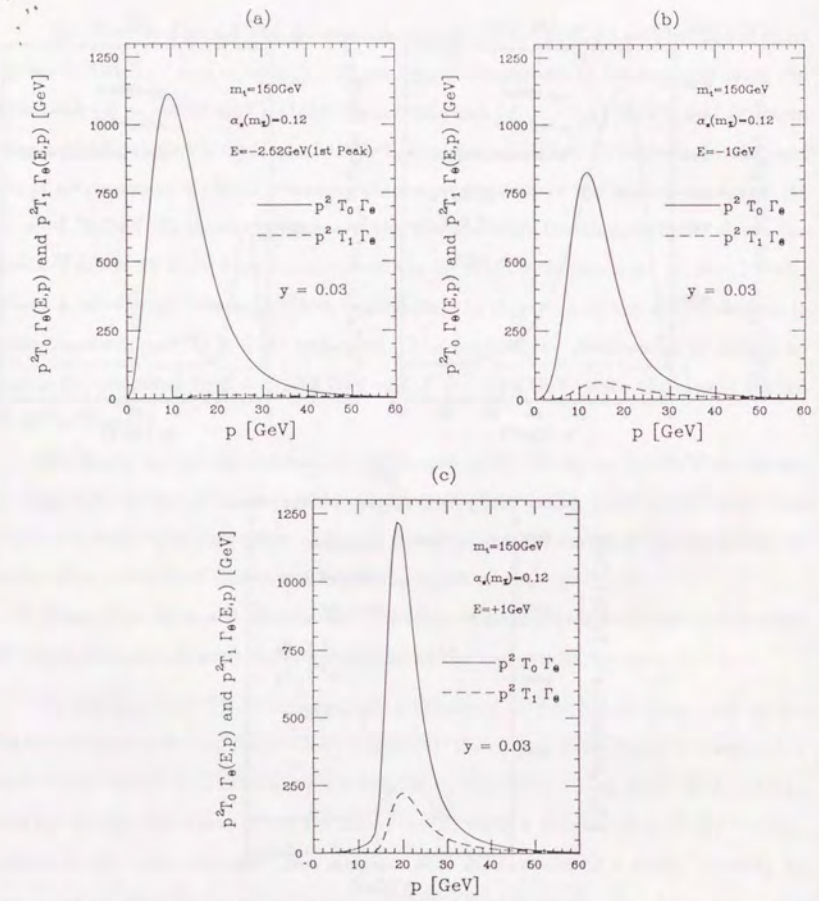

Figure 4.10: The comparison of the spherical distribution (solid) and the $\cos\theta$ distribution (dashed). The dotted line shows the position of zero. In each figure, the energy is taken as (a)$E = -2.12$GeV (at the first resonance peak), (b)$E = -1.14$GeV (at the second resonance peak), and (c)$E = +1$GeV (above threshold).

out in the total cross section.

We may compare the results obtained in this section including the full next-to-leading order corrections with those of the original analyses given in Ref.[16]. We find that the FB-asymmetry at the peak is reduced almost half in magnitude. The sensitivity to α_s is slightly enhanced for $m_t = 150$ GeV, whereas it becomes almost twice as sensitive to α_s for $m_t = 200$ GeV as compared to the original results. One reason for this is due to the inclusion of the $O(\alpha_s)$ correction to the top width Γ_t. The radiative correction reduces Γ_t by $\sim 10\%$ so that the overlap of the resonances decreases. The width becomes smaller for larger α_s. The other reason is the inclusion of the FI term, which decreases the FB-asymmetry for $m_t > 100$ GeV proportionally to α_s. Meanwhile, the change of the FB-asymmetry is found to be less significant in the continuum region, $E > 0$. (cf. eqs. (4.3.10) and (4.3.11).)

We will examine the effect of FI term in the next Chapter more in detail.

Chapter 5

The Effects of the $O(\alpha_S)$ Corrections

In this chapter we investigate the separate contribution to the $O(\alpha_s)$ corrections to the cross sections. In particular, we investigate the effects of the final state interactions in detail, which have not been included in the preceding works [13,14,15,16]. These give non-trivial corrections to the top quark momentum distribution, while the effects on the asymmetric distrtibution are small. The corrections to the total cross section from the final state interactions vanish altogether. Other $O(\alpha_s)$ corrections are also examined. In order to maintain consistency with the analyses in the previous chapter, we use the running toponium width and the two-loop improved potential in our numerical studies; see Section 4.1.

We first look into the effects of the final state interaction diagrams and of $t\bar{t}Z^0$ axial-vector coupling on the top quark 3-momentum distribution, $\mathcal{D}_t(E,|\mathbf{p}|,\cos\theta;y)$, given in Subsection 4.1.a. We parametrize the distribution as follows:

$$\mathcal{D}_t(E,|\mathbf{p}|,\cos\theta;y) = \frac{3\alpha^2}{2m_t^4}\frac{\Gamma_\Theta(E,\mathrm{p})}{2}\cdot|\mathbf{p}|^2(T_0+T_1\cos\theta), \tag{5.0.1}$$

$$T_0 = T_0^{(a)}+T_0^{(b)}, \tag{5.0.2}$$

$$T_1 = T_0^{(VA)}+T_0^{(FI)}, \tag{5.0.3}$$

with the spherical distributions given by

$$T_0^{(a)} = \left[\left(-\frac{2}{3}+\chi g_V^t g_V^e\right)^2+\chi^2(g_V^t)^2(g_A^e)^2\right]$$

$$\times\left\{1-\frac{4C_F\alpha_s}{\pi}-\frac{C_F\alpha_s}{2\pi}\cdot 2h_{bWg}(y;r)\right\}|\tilde{G}(\mathrm{p};E)|^2, \tag{5.0.4}$$

$$T_0^{(b)} = \left[\left(-\frac{2}{3}+\chi g_V^t g_V^e\right)^2+\chi^2(g_V^t)^2(g_A^e)^2\right]$$

$$\times C_F\cdot 4\pi\alpha_s\int\frac{d^3\mathrm{q}}{(2\pi)^3}\frac{1}{|\mathbf{k}|^3}\,2\,\mathrm{Im}[\tilde{G}^*(\mathrm{q};E)\,\tilde{G}(\mathrm{p};E)]\cdot\frac{\pi}{2}, \tag{5.0.5}$$

and the $\cos\theta$ distributions,

$$T_1^{(VA)} = \left(-\frac{2}{3}\chi g_A^e g_A^t+2\chi^2 g_A^e g_V^e g_A^t g_V^t\right)\cdot\frac{|\mathbf{p}|}{m_t}\cdot 2\mathrm{Re}[\tilde{F}^*(\mathrm{p};E)\,\tilde{G}(\mathrm{p};E)], \tag{5.0.6}$$

$$T_1^{(FI)} = 2\chi g_A^e g_V^t\left(-\frac{2}{3}+\chi g_V^e g_V^t\right)\cdot\kappa\cdot C_F\cdot 4\pi\alpha_s$$

$$\times\int\frac{d^3\mathrm{q}}{(2\pi)^3}\frac{1}{|\mathbf{k}|^3}\frac{\mathrm{p}\cdot\mathrm{k}}{|\mathrm{p}|\,|\mathrm{k}|}\,2\,\mathrm{Re}[\tilde{G}^*(\mathrm{q};E)\,\tilde{G}(\mathrm{p};E)]. \tag{5.0.7}$$

Here, the two terms in the spherical distribution, $T_0^{(a)}$ and $T_0^{(b)}$, correspond to the Class (a) and Class (b) diagrams given in Subsection 3.2.d, Figs. 3.7 and 3.8, respectively. Namely, $T_0^{(a)}$ includes the leading S-wave contribution and the radiative corrections to the tbW vertices as well as the corresponding real gluon emission diagrams. $T_0^{(b)}$ corresponds to the final state interaction diagrams together with the real gluon emission diagrams. The origins of the two terms in the asymmetric distribution, $T_1^{(VA)}$ and $T_1^{(FI)}$, are discussed in Subsection 4.3.a. $T_1^{(VA)}$ originates from the interference of the vector and axial-vector $t\bar{t}V$ vertices (VA term), while $T_1^{(FI)}$ stems from the interference of the leading S-wave amplitude and the final state interaction diagrams (FI term).

Figs. 5.1(a)(b)(c) show the $|\mathbf{p}|$-dependences of the above terms $T_0^{(a)}$, $T_0^{(b)}$, $T_0^{(VA)}$ and $T_0^{(FI)}$ multiplied by the phase space factor $|\mathbf{p}|^2\Gamma_\Theta(E,\mathrm{p})$ for the top mass $m_t = 100$, 150, and 200 GeV, respectively, at $E = 0$. We choose $y = 0.03$ for the cut on the bg and $\bar{b}g$ invariant masses in these figures. In all figures in this chapter, we set $\alpha_s(m_Z) = 0.12$. It can be seen that the effects of the final state interactions ($T_0^{(b)}$ and $T_1^{(FI)}$) increase for larger m_t. This is reasonable considering the rapid growth of the top width with m_t, since the final state interaction, which represent the exchange of gluons *after* the decay of resonances, are expected to be significant only for a short-lived top quark.

The contribution of the final state interaction diagrams to the spherical distribution, $|\mathbf{p}|^2T_0^{(b)}\Gamma_\Theta$, has a humpy shape for $m_t = 100$ GeV. (Fig. 5.1(a)) Meanwhile, for

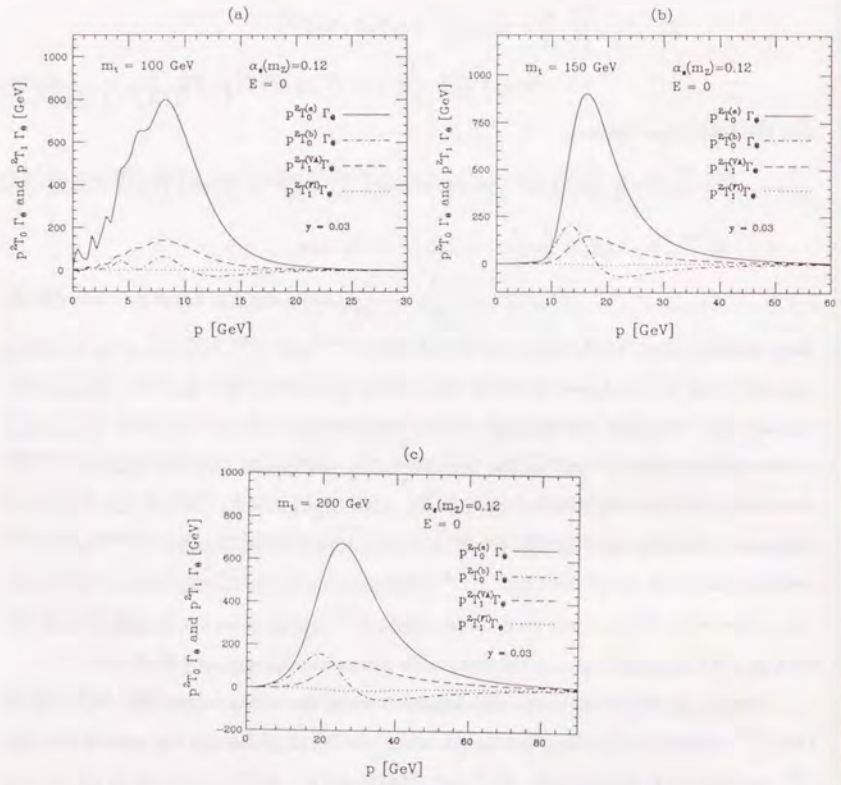

Figure 5.1: (a) The separate contribution to the spherical and $\cos\theta$ distributions versus top momentum $|\mathbf{p}|$, for $m_t = 100$ GeV and $\alpha_s(m_Z) = 0.12$. (b) The same as (a) but for $m_t = 150$ GeV. (c) The same as (c) but for $m_t = 200$ GeV.

$m_t = 150$ GeV and 200 GeV, $T_0^{(b)}$ has a smoother shape, which enhances the momentum distribution T_0 in the low momentum region whereas suppresses the distribution in the high momentum region as seen in Figs. 5.1(b)(c). For instance, this results in the shift of peak position of the momentum distribution, $|\mathbf{p}|_{peak}$, in negative direction at 5% level for $m_t = 150$ GeV. The contribution to the cross section vanishes upon integration over the momentum $|\mathbf{p}|$; see Subsections 3.2.d and 4.1.b.

In each figure, it can be seen that the main contribution to the asymmetric distribution, $|\mathbf{p}|^2 T_1 \Gamma_\ominus$, comes from the VA term $T_1^{(VA)}$. That from the FI term, $T_1^{(FI)}$, is smaller. This smallness is in part due to the smallness of the factor κ, and in part because the main part in the loop integral in (5.0.7) cancels out by taking the principal value. The significance of the VA term at the threshold, $E = 0$, is almost the same in all figures, $m_t = 100$, 150 and 200 GeV. This contrasts with the VA term evaluated at the lowest lying peak below threshold, which measures the overlap of the S-wave and P-wave resonances, and grows rapidly with m_t. See Subsection 4.3.b, Fig. 4.7. The magnitude of FI term increases slightly for larger m_t. It is consistent with the behavior of the other final state interaction term $T_0^{(b)}$.

The dependences of $T_0^{(b)}$ and $T_1^{(FI)}$ on m_t and $|\mathbf{p}|$ reflect the behavior of the S-wave Green's function $\tilde{G}(\mathbf{p}; E)$. We show the $|\mathbf{p}|$-dependences of $\tilde{G}(\mathbf{p}; E)$ on the complex $\tilde{G}$-plane in Figs. 5.2(a)(b)(c) for $m_t = 100$, 150, and 200 GeV, respectively, with the energy fixed at $E = 0$. The Green's function approaches zero as $|\mathbf{p}| \to \infty$ in each figure. For $m_t = 100$ GeV, with a relatively small top width, $\tilde{G}(\mathbf{p}; E)$ oscillates rapidly as $|\mathbf{p}|$ increases. (Fig. 5.2(a).) One can show that $\tilde{G}(\mathbf{p}; E)$ tends to be more oscillatory for larger E [14]. This oscillatory behavior causes the humpy behavior of $T_0^{(b)}$ as well as suppresses $T_0^{(b)}$ and $T_0^{(FI)}$ for $m_t = 100$ GeV. On the other hand, the $|\mathbf{p}|$-dependence of $\tilde{G}(\mathbf{p}; E)$ gets milder for $m_t = 150$ GeV and 200 GeV due to the smearing effect by the large top width Γ_t; see the contours on the complex plane in Figs. 5.2(b)(c). Then one may verify the behavior of $|\mathbf{p}|^2 T_0^{(FI)} \Gamma_\ominus$ in Figs. 5.1(b)(c) by examining the integrand $\propto \mathrm{Im}[\tilde{G}^*(\mathbf{q}; E)\, \tilde{G}(\mathbf{p}; E)]$ in eq. (5.0.5) with the above behaviors of $\tilde{G}(\mathbf{p}; E)$.

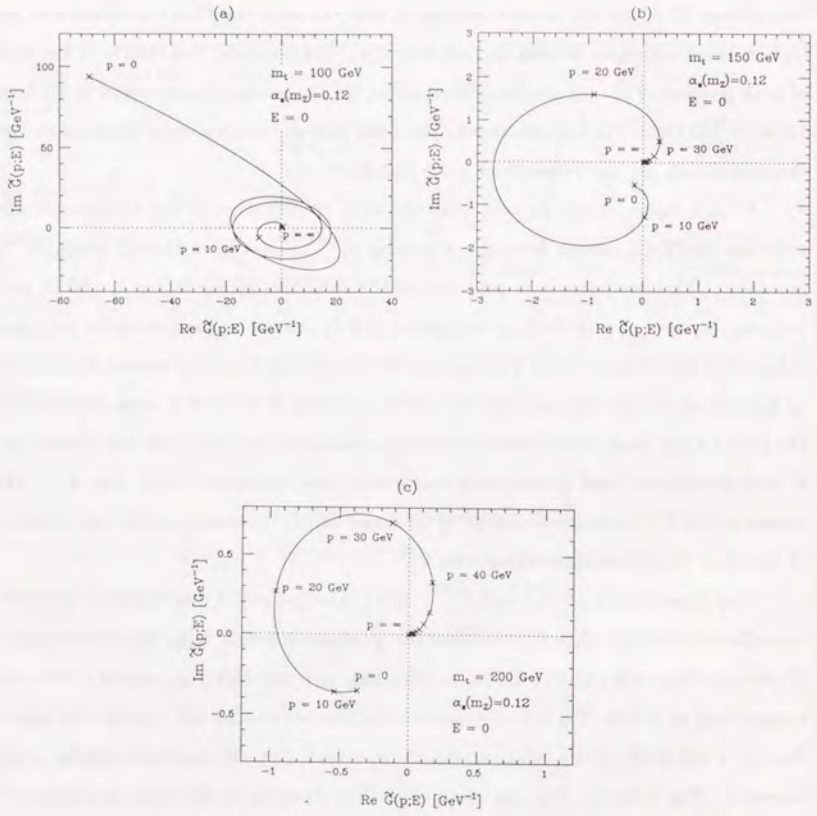

Figure 5.2: (a) The value of Green's function $\tilde{G}(\mathbf{p}; E)$ shown on the complex plane as the top momentum $|\mathbf{p}|$ is varied, for $m_t = 100$ GeV and $\alpha_s(m_Z) = 0.12$. (b) The same as (a) but for $m_t = 150$ GeV. (c) The same as (a) but for $m_t = 200$ GeV.

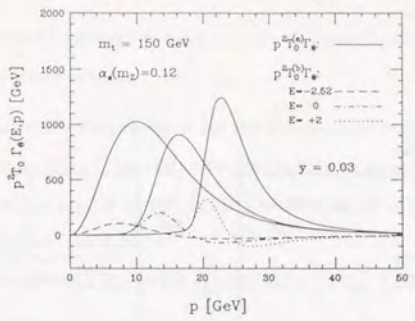

Figure 5.3: The separate contribution to the spherical distribution as a function of top momentum $|\mathbf{p}|$. The three curves correspond to the energies $E = -2.52$ GeV (at the first peak), $E = 0$ GeV, and $E = 2$ GeV from the left-most to the right.

We also show the energy (E) dependences of $|\mathbf{p}|^2 T_0^{(a)} \Gamma_\Theta$ and $|\mathbf{p}|^2 T_0^{(b)} \Gamma_\Theta$ in Figs. 5.3 for $m_t = 150$ and $y = 0.03$. The effect of final state interactions, $T_0^{(b)}$, becomes more significant as the energy is raised. This can be understood if we consider $T_0^{(b)}$ in the narrow width limit $\Gamma_t \to 0$ at the energy corresponding to some resonance peak $E = E_n$ below threshold. Then, the Green's function becomes

$$\tilde{G}(\mathbf{p}; E_n) \to -\frac{\phi_n(\mathbf{p})\psi_n^*(0)}{i\Gamma_t}, \tag{5.0.8}$$

so that the integrand $\propto \mathrm{Im}[\tilde{G}^*(\mathbf{q}; E)\,\tilde{G}(\mathbf{p}; E)]$ vanishes in eq. (5.0.5).[1] Thus, it is expected that $T_0^{(b)}$ is smaller for the narrower resonance widths and also at the lower lying resonances where the resonance levels stand apart from one another. Oppositely, $T_0^{(b)}$ tends to increase in the continuum region where the interferences among the resonances are more severe.

In order to observe the energy dependence of the asymmetric terms, $T_1^{(VA)}$ and $T_1^{(FI)}$, we show in Figs. 5.4(a)(b)(c) the energy dependences of the contributions of these terms to the FB-asymmetry Δ_{FB} for $m_t = 100$, 150 and 200 GeV, respectively. It can be seen that the FB-asymmetry from the FI term is small, decreasing with energy. The

[1] The S-wave resonance wave functions, $\phi_n(\mathbf{p})$ and $\psi_n(\mathbf{x})$, can be chosen real.

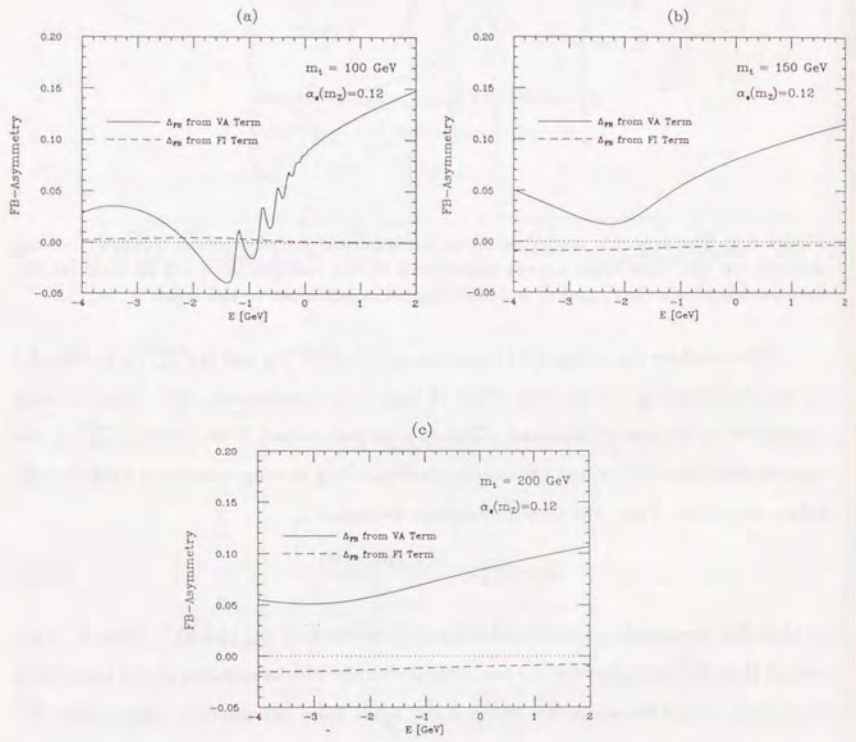

Figure 5.4: The separate contributions to the FB-asymmetry, $\Delta_{FB}^{(VA)}$ and $\Delta_{FB}^{(FI)}$, versus energy, $E = \sqrt{s} - 2m_t$, for $m_t = 100$ GeV. (b) The same as (a) but for $m_t = 150$ GeV. (c) The same as (a) but for $m_t = 200$ GeV.

VA term increases as the energy is raised, since the overlaps of the S-wave and P-wave resonances become more severe.

We now examine the cross section for the kinematical region other than considered above, which is also an $O(\alpha_s)$ correction to the leading cross section. These are the cross sections over the wider region of bW invariant masses, $O(\alpha_s^2) \ll m_{bW}^2 - m_t^2 \lesssim O(\alpha_s)$. See discussion in Subsection 3.2.e.

We are concerned with the cross section given in eq. (3.2.86):

$$\frac{d\sigma_{t\bar{t}g}^{(WA)}}{d|\mathbf{p}|d\cos\theta} = \frac{3\alpha^2\Gamma_t}{2m_t^4}|\mathbf{p}|^2\left[T_0^{(WA)} + T_2^{(WA)}\frac{3\cos^2\theta - 1}{2}\right] \tag{5.0.9}$$

with

$$\begin{aligned} T_0^{(WA)} &= \left[\left(-\frac{2}{3}+\chi g_V^t g_V^e\right)^2 + \chi^2 (g_V^t)^2 (g_A^e)^2\right]\cdot C_F\cdot 4\pi\alpha_s \cdot \int \frac{d^3\mathbf{q}}{(2\pi)^3}\frac{1}{|\mathbf{k}|^3} \\ &\quad \times |\tilde{G}(\mathbf{q};E)|^2\left\{\Phi_{00}(y_0) - \kappa^2\,\Phi_{55}(y_0) + \frac{2}{3}P_0\cdot\kappa^2\,\Phi_{55}(y_0)\right\}, \end{aligned} \tag{5.0.10}$$

$$\begin{aligned} T_2^{(WA)} &= \left[\left(-\frac{2}{3}+\chi g_V^t g_V^e\right)^2 + \chi^2 (g_V^t)^2 (g_A^e)^2\right]\cdot C_F\cdot 4\pi\alpha_s \\ &\quad \times \int \frac{d^3\mathbf{q}}{(2\pi)^3}\frac{1}{|\mathbf{k}|^3}|\tilde{G}(\mathbf{q};E)|^2\left(-\frac{2}{3}P_2\right)\kappa^2\,\Phi_{55}(y_0). \end{aligned} \tag{5.0.11}$$

Figs. 5.5(a)(b)(c) show the distributions, $|\mathbf{p}|^2 T_0^{(WA)}\Gamma_\Theta$ and $|\mathbf{p}|^2 T_2^{(WA)}\Gamma_\Theta$, together with the momentum distribution $|\mathbf{p}|^2 T_0\Gamma_\Theta$ in the region $m_{bW}^2 - m_t^2 \lesssim O(\alpha_s^2)$, at $E = 0$, for $m_t = 100$ GeV, 150 GeV and 200 GeV, respectively. The cut on the bg and $\bar{b}g$ invariant masses is chosen as $y = 0.03$. One sees that the contribution $T_0^{(WA)}$ is larger for a heavier top quark, $\sim 3\%$ for $m_t = 200$ GeV. $T_2^{(WA)}$ is quite small, and can be safely neglected for practical purposes.

As a comparison to the above effects, we also demonstrate the effects of the $O(\alpha_s)$ corrections that are conventionally included in the calculation of $t\bar{t}$ threshold cross sections. In Fig. 5.6 are shown the effects of hard gluon correction[34] and of the radiative correction to the top quark width[30,31,32] on the total cross section for $m_t =$ 150 GeV. The former correction, $(1 - 4C_F\alpha_s/\pi)$, reduces the normalization of the cross

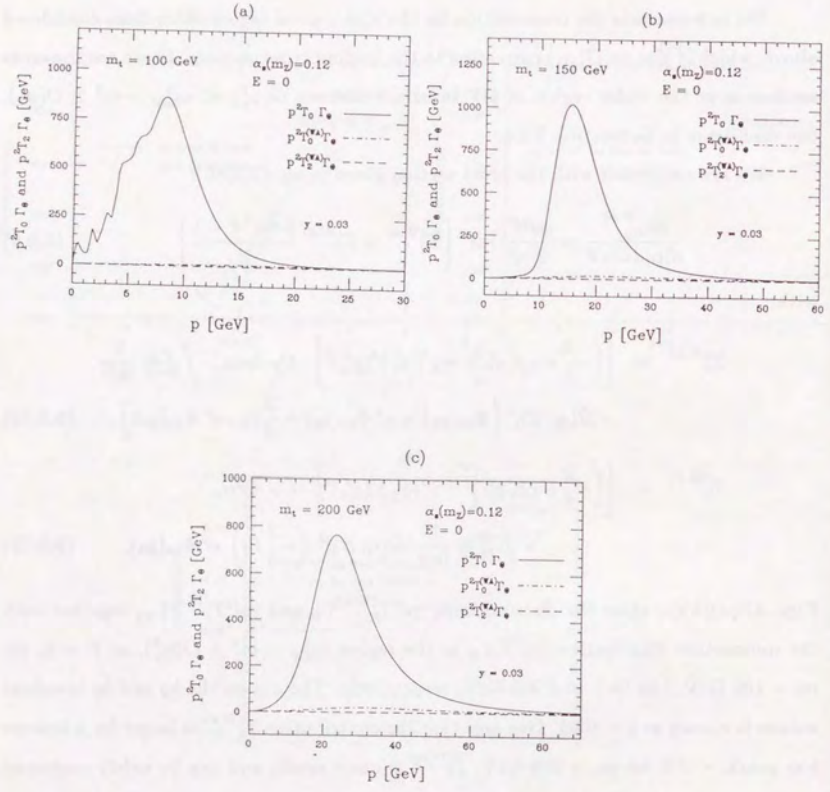

Figure 5.5: (a) The top momentum distribution for the kinematical region, $O(\alpha_s^2) \ll m_{bW}^2 - m_t^2 \lesssim O(\alpha_s)$ for $m_t = 100$ GeV. (b) The same as (a) but for $m_t = 150$ GeV. (c) The same as (a) but for $m_t = 200$ GeV.

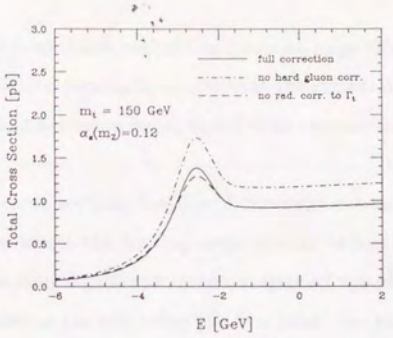

Figure 5.6: The total cross section versus energy, $E = \sqrt{s} - 2m_t$, for $m_t = 150$ GeV and $\alpha_s(m_Z) = 0.12$. The solid curve shows the cross section with full $O(\alpha_s)$ corrections, while the dotdashed (dashed) curve shows that without the hard gluon correction (radiative correction to Γ_t).

section by about 20%. The latter correction reduces the top quark width by about 10%, which enhances the cross section at the peak. This effect becomes more significant for a lighter top quark.

Chapter 6

Discussion

6.1 Other Corrections

The quantitative analyses of the cross sections presented in this paper are by no means exhaustive. There are a number of corrections that should be taken into account before comparing the above results to the real life experiments. In particular, the effects of the initial state radiation and beamstrahlung are known to be important near the resonances. Studies of the $t\bar{t}$ threshold cross sections including these effects have been presented in the literatures [10,15,17,18]. We also plan to give the numerical studies including the effects besides the full $O(\alpha_s)$ corrections to the cross sections in the forthcoming paper[42]. In the following, we list the estimations of other smaller corrections neglected in our numerical studies, which are typically at a few percent level. Some of them are straightforward to include, but some of them are not.

First, let us consider the higher order QCD corrections. The calculation of the complete second order QCD corrections would be a formidable task, where it is necessary to include all $O(\alpha_s^2) \simeq O(\beta^2)$ corrections to the Bethe-Salpeter kernel, top propagators, tbW vertex, etc. It seems that some new technicalities should be developed in order to accomplish such calculations. Nevertheless we may estimate the magnitude of the corrections. We quote below the effect of the running toponium width $\Gamma_\Theta(E, \mathbf{p})$, investigated in detail in Ref.[13], as a measure for the second order QCD corrections.

As we are interested in the cross sections over the entire threshold region, we need

to consider in which kinematical region there may be large $O(\alpha_s^2)$ corrections. One may categorize the kinematical regions by noting that the expansion parameters of the cross sections near threshold are given by α_s and β with respect to the leading contribution $\sum c_n(\alpha_s/\beta)^n$.

For the total cross section, the $O(\alpha_s^2)$ corrections would be relatively small at the resonance peaks where the leading cross section is most enhanced, whereas the corrections would be more significant at the energies off the peaks, especially below the first resonance. Indeed at the tail below the first peak, the effect of the running width exceeds 50% level, while it is $\sim 3\%$ at the peak. Also, in the continuum region, it is expected that the higher order corrections would grow like $\sim \beta^2$ as the c.m. energy is increased. In this region the effect of the running width is found to be $\sim 2\%$ for $\beta \lesssim 0.1$. The matching of the total cross sections in the intermediate region, $\beta \gtrsim \alpha_s$, was first examined by Kwong[9]. He showed the fairly good matching of the total cross section calculated in the threshold region and that calculated in the open top region according to the ordinary perturbation theory by including the $O(\alpha_s)$ corrections. He also showed that the matching can be made even smoother by a reasonable choice of the momentum scale μ in the hard gluon correction factor, $[1 - 2C_F\alpha_s(\mu)/\pi]$, the shift of which corresponds to the inclusion of a part of the $O(\alpha_s^2)$ corrections.

Now we turn to the $O(\alpha_s^2)$ corrections to the differential cross sections. One should note that, in this case, relatively large corrections would be generated not only in the large β region but also in the high momentum region of top quark, since the expansion now involves the powers of $|\mathbf{p}|/m_t$ as well. The effect of running width, which is the inclusion of the phase space voluum for bW's, suppresses the top momentum distribution as $\sim [1 - 3(|\mathbf{p}|/m_t)^2]$ in the highly off-shell region. It is known that, similarly, a large correction exists in the $O(\alpha)$ calculation of orthopositronium decay distribution[43] at the endpoints of the phase space (at the level of $\sim 7\alpha$). This large correction in the highly off-shell region of top quark differential cross section is the very origin of the discrepancy in the total cross sections that calculated via the optical

theorem and that obtained by integrating the differential cross section in the constant width approximation, which is as large as 12% at the peak[13].

These considerations suggest that the total cross section calculated via the optical theorem is more stable as compared to that calculated from the integration of the differential cross section. This is because the total cross section includes only the c.m. energy as the kinematical varable, and hence can be calculated directly from the imaginary part of the photon vacuum polarization without the detailed knowledge of the differential information. In fact the effect of the running width, which restores the unitarity relation, shifts the former cross section by $2 \sim 3\%$, while the correction to the latter exceeds 10%.

In summary, the theoretical prediction for the total cross section calculated directly via the optical theorem is expected to be quite stable for the c.m. energies from above the first resonance to the continuum region, $\beta \lesssim 0.1$. We estimate the $O(\alpha_s^2)$ corrections to be at the level of $\lesssim 5\%$ in this region. Also, the predictions for the differential cross sections would be more stable in the low momentum region, but the $O(\alpha_s^2)$ corrections would grow in the high momentum region proportionally to $(|\mathbf{p}|/m_t)^2$, in addition to the normalization correction as in the total cross section. We estimate its coefficient to be $\lesssim 5$.

Regarding the second order QCD corrections, it should be noted that the FB-asymmetry presented in this paper is already an $O(\alpha_s)$ quantity, always of the order 10%, and the above corrections would appear as a few percent theoretical uncertainty. Therefore it is desirable to have the part of the $O(\alpha_s^2)$ calculations that is relevant to the FB-asymmetry in order to establish the reliable theoretical prediction of this quantity. We believe such calculations will be attained in due time.

Let us now discuss other specific corrections.

Also the electroweak corrections to the leading order amplitude become the $O(\alpha_W) \sim O(\alpha_s^2)$ corrections. These include the radiative corrections to the leading diagram $e^+e^- \to t\bar{t} \to bW^+\bar{b}W^-$ as well as the tree diagrams which are non-resonant near $t\bar{t}$

threshold but include single top pole in the bW-invariant-mass channel. It is straightforward to include the corrections in comparison to the second order QCD corrections. Among them, perhaps the most interesting are the effects of Higgs exchange between t and $\bar{t}$, which causes the threshold enhancement in the light Higgs limit. The Higgs effects are estimated in the literatures [10,15,18] for realistic top and Higgs masses, which give typically $\sim 5\%$ enhancement in the cross sections, but can become more significant for a light Higgs and for a heavy top quark. One may ask that the photon exchange between t and $\bar{t}$ would induce the potential $\sim -\alpha/r$, which is roughly $O(\alpha_s)$ correction to the QCD potential $\sim -\alpha_s/r$. The answer is that it amounts to effectively increasing the strong coupling constant $\alpha_s(\mu = \alpha_s m_t) \simeq 0.15$ by about 3% in the QCD potential when the charge ratio $\frac{3}{4}\left(\frac{2}{3}\right)^2 = \frac{1}{3}$ is taken into account.

As discussed in Subsection 3.1.a, the non-perturbative corrections coming from the low energy QCD is expected to be quite small. A part of such corrections was estimated to be less than 3% for $m_t > 100$ GeV[26], which rapidly diminishes as m_t grows.

The last correction we consider is the finite b-quark mass. We neglected m_b everywhere except in the QCD potential. Other most significant correction from m_b is to the top quark decay width in the leading order. The effect of m_b is largest for a light top quark (4% for $m_t = 100$ GeV) and decreases rapidly with m_t (0.5% for $m_t = 150$ GeV).

6.2 QCD Potential

Although we quoted the conventional QCD potential in Section 3.2, and used the improved potential (given in Appendix C) in our numerical analyses, some cautions should be made regarding these potentials. We intend to compare our analyses with the experiments to extract the value of α_s defined in the $\overline{\text{MS}}$ scheme, which seems to be preferrable in many respects. However, the conventional QCD potentials might differ by a constant shift of the coupling from the potential introduced in our framework, defined using the Bethe-Salpeter kernel as in eq. (3.2.47). The conventional QCD potential, as calculated by the authors of Refs.[35], is obtained by evaluating the Wilson

loop of the quark line and extracting the energy between the quark and anti-quark pair as a function of the distance between them. Hence, it is given gauge invariantly by definition. The potential defined in our framework, however, is not necessarily gauge invariant. Feinberg[6] obtained the similar potential as that in Refs.[35] starting from the Bethe-Salpeter kernel, but he used rather unusual renormalization scheme. So it may happen that the potential as defined in the current work differs by a constant shift of the coupling constant α_s, of $O(\alpha_s^2)$, which corresponds to the different choices of the renormalization scheme at the one-loop level. We are currently re-calculating the QCD potential. The inclusion of the constant shift is straightforward.

Chapter 7

Conclusion

In this thesis, we reported the studies of the cross sections and the underlying physics for the $t\bar{t}$ pair production process in the threshold region at e^+e^- colliders. The numerical studies were performed including the full next-to-leading order corrections, and we confirmed the observation[2,10] that the $t\bar{t}$ threshold cross sections can provide clean tests of QCD. It was found that top quark threshold physics is quite rich in phenomenology. We summarize our achievements below.

7.1 Theory

As discussed through Chapters 1-3 based on the original observation by Fadin and Khoze, one may obtain quite stable theoretical predictions for the total and differential cross sections over the threshold region for the $t\bar{t}$ pair production process in e^+e^- collisions. This is due to the large top mass, which renders the toponium to be Coulombic bound state, and also due to the large top width, which acts as the infra-red cut-off of the gluon momentum. We provided a solid theoretical framework to deal with the toponium resonances in Chapter 3 and in Appendices. In Section 3.1, we explained the basic theoretical concept by translating the above physical intuition into more theoretical form. We saw explicitly in the uncrossed ladder diagrams the appearance of the leading threshold singularities, $\sim (\alpha_s/\beta)^n$, due to the formation of threshold bound states. Also, it was seen that the gluon momentum is cut off in the infra-red region

at the scale $\sim \sqrt{m_t \Gamma_t}$. The calculation of the full $O(\alpha_s)$ corrections to the S-matrix element and the cross sections were presented step by step in Section 3.2, with references to the detailed framework and the necessary tools developed in the Appendices. In effect, we included the $O(\alpha_s)$ corrections to the pole positions, the residues and the regular part of the matrix element.

7.2 Cross Sections

In addition to the total cross section, which has already been studied in Refs.[2,10], we presented the analyses of the top quark momentum distributions and the forward-backward (FB) asymmetry in detail in Chapter 4. We have included the full next-to-leading order corrections to the cross sections. The necessary formulas were summarized in Section 4.1. Also, we examined the effect of each $O(\alpha_s)$ correction on the cross sections separately in Chapter 5.

Total Cross Section and Momentum Distribution

In Section 4.2, we showed the total cross section and top momentum distribution for various values of m_t and α_s. The main structures of these cross sections are determined by the leading Coulombic enhancement together with the smearing effect by the large top quark width. We reproduced the known results for the threshold total cross section, and showed explicitly that it is insensitive to the long distance physics. We also showed that the investigation of differential cross sections will provide us with information independent of that extracted from the total cross sections since we may directly observe the wave function of toponium states in momentum space. The distribution extends over the momentum range $\sim$ (Bohr radius)$^{-1} \simeq \alpha_s m_t$. The peak position of the momentum distribution, $|\mathbf{p}|_{peak}$, is sensitive to α_s since the kinetic energy of top quark varies as the binding energies of resonances are increased or decreased. Therefore, studies of the momentum distribution together with the total cross section would be useful in the determination of the two parameters, m_t and α_s.

Asymmetric Distribution

We have also investigated the asymmetric distribution of top quark in Section 4.3. The asymmetric distribution appears as part of the $O(\alpha_s)$ corrections to the threshold cross section. The major contribution comes from the interference between S-wave and P-wave resonance states, which becomes significant for larger m_t as the widths of the resonances grow rapidly. Therefore, the FB-asymmetry increases with m_t, allowing its experimental study. We also studied the α_s-dependence of the asymmetry, which becomes more sensitive for larger m_t. This is in contrast to the total cross section, which loses sensitivity to α_s due to the large smearing effect as m_t grows. A careful study of the FB-asymmetry at future e^+e^- colliders would allow an efficient cross-check to the measurement of α_s. In spite of the smearing of the resonance structures, there still exist the resonance poles in the amplitude. It is seen that the FB-asymmetry can 'measure' the relative magnitude of the level splittings and the widths of the resonances, while it is insensitive to the normalization of the cross sections. Since the level structure is among the basic quantities of QCD in the threshold region, it is worth emphasizing that a part of the structure is measurable even with the large resonance widths. Appearance of the FB-asymmetry even below threshold reflects the interplay between QCD and electroweak interactions unique to the toponium.

$O(\alpha_s)$ Corrections

The next-to-leading order corrections to the $t\bar{t}$ threshold cross sections introduced by the present author are the contributions from the $t\bar{t}Z^0$ axial-vector coupling[16], those from the final state interaction diagrams, and also those from the relevant real gluon emission process. These corrections, besides other previously known $O(\alpha_s)$ corrections, were studied separtely in Chapter 5, and were found to give rise to the order 10% corrections to the top quark differential cross sections as anticipated. It turned out, however, that the corrections from the final state interaction diagrams, together with the corresponding real emission process, canceled out altogether at $O(\alpha_s)$ in the total

cross section. This justifies the analyses of the total cross section given in Ref.[15] up to the next-to-leading order.

7.3 Other Corrections

There are still other corrections that should be included to the present analyses of the cross sections. They are discussed in Chapter 6. The effects of the initial state radiation and beamstrahlung are most important. It is straightforward to include these effects. It would be difficult to calculate the full second order QCD corrections, which are estimated to give the corrections of typically $\lesssim 5\%$. In addition, the QCD corrections would grow proportionally to $(|\mathrm{p}|/m_t)^2$ in the differential cross sections. Most of other corrections are straightforward to include. Besides these corrections, there is a possible source of the modification of the QCD potential used in our analyses. The calculation is currently underway.

Acknowledgements

The author wishes to thank Prof. T. Eguchi for his special concern on this thesis and for his continuous encouragement during its preparation. The author wishes to express his sincere gratitude to Dr. K. Hagiwara and Dr. K. Hikasa, and also to Dr. K. Fujii and Dr. H. Murayama, who taught the author very basics of the current particle phenomenology, to the very details of the physics in the $t\bar{t}$ pair production process. This thesis consists of the works in collaboration with them, and also with Dr. C.-K. Ng and S. Ishihara. All collaborators helped the author greatly completing the thesis through valuable discussions and by presenting many additional key ideas. Most of the beautiful Feynman diagrams included in this thesis are drawn by S. Ishihara. Also he made many suggestions by which the author could improve the thesis very much. The author deeply appreciates his kind gesture of partnership. The author is also grateful to T. Izubuchi and T. Hotta for reading the manuscript carefully and making useful comments.

Note Added:

After completion of this work, we received a preprint by K. Melnikov and O. Yakovlev[51], where the effects of the final state interactions on the total cross section are calculated as the additional $O(\alpha_s)$ corrections. The method of the calculations are similar to ours, and their conclusion, that these new corrections at $O(\alpha_s)$ vanish in the total cross section, is in agreement with ours. They do not calculate the effects of these corrections on the differential cross sections though.

Appendix A

Perturbative Expansion Near Threshold

As the series representation $\sum c_n(\alpha_s/\beta)^n + ...$ introduced in Section 3.1 is not very efficient for $\sqrt{s} \lesssim 2m_t$, one needs a more systematic treatment of the amplitude for $e^+e^- \to bW^+\bar{b}W^-$ in the threshold region. In this appendix, we explain how in principle the perturbation theory should be constructed in the threshold region (Step 1 $\sim$ 3), and also how the calculation of $O(\alpha_s)$ correction will be performed in practice (Step 3). We note that the main purpose of presenting the former is to meet the theoretical interest; in order to clarify the theoretical basis of our present work and also for completeness. While the prescription would be useful in the case of narrow resonances, it becomes more difficult to apply it for the resonances with relatively large decay widths since the interference among various resonances become significant[9]. In a more practical approach (latter) one numerically evaluates the Green's function which contains the contributions from all resonances[10]. In this manner, however, one cannot truncate the amplitude at some specific order of the perturbative expansion. Part of the higher order contributions cannot be eliminated[29] though all the contributions up to the desired order (leading plus $O(\alpha_s)$ correction) are included.

To begin with, it should be reminded that in the threshold region

$$E = \sqrt{s} - 2m_t \sim O(\alpha_s^2), \tag{A.1}$$

the amplitude tends to exhibit the large leading threshold singularities only for the bW^+

and $\bar{b}W^-$ invariant masses[1] satisfying

$$m^2_{bW^+} - m_t^2 \sim O(\alpha_s^2), \tag{A.2}$$

$$m^2_{\bar{b}W^-} - m_t^2 \sim O(\alpha_s^2), \tag{A.3}$$

according to the power counting presented in Subsection 3.1.a. For off-shell invariant masses $m^2_{bW^+} - m_t^2$, $m^2_{\bar{b}W^-} - m_t^2 \gg \alpha_s^2 m_t^2$, the enhancement of the amplitude disappears.[2] Therefore we will constrain ourselves to the above kinematical region (A.1), (A.2) and (A.3) in the following context. It is often convenient to use the momentum of the center of gravity P and the relative momentum p in describing the $t\bar{t}$ system. i.e. $p_t = P/2 + p$ and $\bar{p}_t = P/2 - p$. At the c.m. frame, $P = (2m_t + E, \mathbf{0})$, and the conditions (A.1), (A.2) and (A.3) are equivalent to

$$P^0 - 2m_t,\ p^0 \sim O(\alpha_s^2), \qquad \mathbf{p} \sim O(\alpha_s). \tag{A.4}$$

Step 1

We first decompose the full S-matrix element by its analytical structure. According to Stuart[29], one should make a Laurent expansion of the S-matrix element about the resonance pole to identify the pole position, the residue of the pole, and the non-resonant background. Then each of these pieces can be expanded as the perturbation series of the coupling constant independently, and can be evaluated order by order in a systematic as well as gauge-invariant manner.[3]

In the threshold region, the S-matrix element for the process $e^+e^- \to bW^+\bar{b}W^-$ can be decomposed in terms of the pole structures of the variables p^0 and P^0 as

$$S_{fi}(p,P) = \frac{R_1(\mathbf{p})}{(P^0-\omega)(p_t^0-\sigma_\mathbf{p})} + \frac{R_2(\mathbf{p})}{(P^0-\omega)(\bar{p}_t^0-\sigma_\mathbf{p})} + \frac{R_3(\mathbf{p},P^0)}{(p_t^0-\sigma_\mathbf{p})(\bar{p}_t^0-\sigma_\mathbf{p})}$$
$$+ \frac{R_4(p^0,\mathbf{p})}{P^0-\omega} + \frac{R_5(\mathbf{p},P^0)}{p_t^0-\sigma_\mathbf{p}} + \frac{R_6(\mathbf{p},P^0)}{\bar{p}_t^0-\sigma_\mathbf{p}} + C(p,P), \tag{A.5}$$

[1] bW invariant mass distribution naturally has the width $\sim m_t\Gamma_t$. In this sense it is reasonable to identify α_s^2 and α_W as the same order quantities.

[2] The amplitude will be suppressed by $\sim \alpha_s^4$ in the very off-shell region $p^0, |\mathbf{p}| \sim O(1)$.

[3] For the case of bound state, not only the powers of α_s but also terms with $\log(\alpha_s^{-1})$ appear due to the long range nature of the interaction[25].

where $p_t^0 = P^0/2 + p^0$ and $\bar{p}_t^0 = P^0/2 - p^0$. We fix the frame to the c.m. frame, and suppressed the dependence on kinematical variables other than p and P. The pole positions of toponium resonance and top propagator on the complex plane are given by ω and $\sigma_{\rm p} \simeq ({\rm p}^2 + m_t^2 - im_t\Gamma_t)^{1/2}$, respectively. We consider the case of one resonance pole in the s-channel for simplicity. In general, one should sum up the contributions from all resonances.

One wishes to determine the pole position (ω and $\sigma_{\rm p}$), the residues ($R_1 \sim R_6$), and the non-resonant part (C) perturbatively. Each component may be expanded in a perturbation series by noting that the variables $p^0, {\rm p}, P^0$ have certain powers of α_s in the kinematical configuration of our interest; see eq. (A.4). (e.g. One may expand the component in terms of α_s after putting $p^0 = \alpha_s^2\xi$, ${\rm p} = \alpha_s\vec{\eta}$, $P^0 - 2m_t = \alpha_s^2\zeta$.)

Step 2

Next we consider how to determine the each component (the pole position, the residue, and the non-resonant part) of the S-matrix element. The full S-matrix element is classified diagramatically into two parts as

$$S_{fi}(p,P) = V_{it}\cdot\mathcal{G}\cdot V_{tf} + C_{if} \tag{A.6}$$

with

$$V_{tf} = V_{tf}^c + V_{tf}^d, \tag{A.7}$$

where the first term of (A.6) represents the diagrams that have $t\bar{t}$ state as the intermediate state, while the second term represents those without $t\bar{t}$ intermediate state; see Fig. A.1.

V_{it} and V_{tf}^c denote the one- as well as two-particle-irreducible[4] (2PI) amputated Green's functions for $e^+e^-t\bar{t}$ and $t\bar{t}\,bW^+\bar{b}W^-$ vertices, respectively, and V_{tf}^d is the disconnected counterpart of V_{tf}^c; see Figs. A.1 and A.2. C_{if} consists of all diagrams without

[4]Diagrams that cannot be disconnected by cutting one t and one $\bar{t}$ internal lines. (= Bethe-Salpeter irreducible)

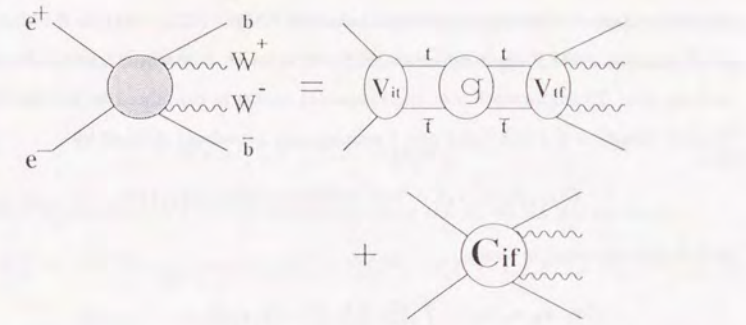

Figure A.1: Diagramatical classification of the S-matrix element for $e^+e^- \to bW^+\bar{b}W^-$. The first and second term on the right-hand-side represent the diagrams with and without the $t\bar{t}$ intermediate state, respectively.

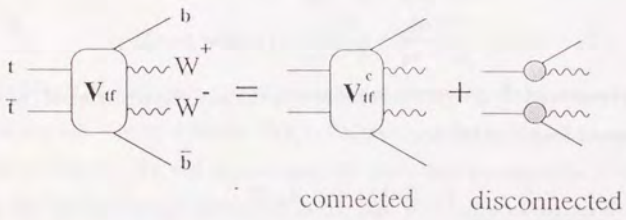

Figure A.2: Diagrams for the $t\bar{t}bW^+\bar{b}W^-$ vertex, V_{tf}. They are separated into the connected part and disconnected part in the t-channel.

$t\bar{t}$ intermediate state for the process $e^+e^- \to bW^+\bar{b}W^-$. The dots in the first term of (A.6) represent the loop integrations of the $t\bar{t}$ relative momenta, contraction of spinor indices, etc. The information of the resonance states is contained in the full $t\bar{t}$ 4-point Green's function $\mathcal{G}$ (with full t and $\bar{t}$ propagators attached) defined by

$$\mathcal{G}(x_1,x_2,x_3,x_4) = \langle 0 \,|\, T\,\psi(x_1)\bar{\psi}(x_2)\bar{\psi}(x_3)\psi(x_4)\,|\,0\,\rangle\,, \tag{A.8}$$

and in the momentum space,

$$\begin{aligned}\mathcal{G}(x_1,x_2,x_3,x_4) = &\int \tfrac{d^4p}{(2\pi)^4}\tfrac{d^4q}{(2\pi)^4}\tfrac{d^4P}{(2\pi)^4}\,\mathcal{G}(p,q,P)\\ &\times \exp\left[-iP\cdot\tfrac{1}{2}(x_1+x_2-x_3-x_4) - ip\cdot(x_1-x_2) + iq\cdot(x_3-x_4)\right].\end{aligned} \tag{A.9}$$

As we will see in Step 3, the 4-point function $\mathcal{G}$ has the structure[5]

$$\begin{aligned}\mathcal{G}(p,q,P) &= \frac{\chi(p)\bar{\chi}(q)}{P^0-\omega} + \frac{r_1(\mathbf{p},\mathbf{q},P^0)}{(p_t^0-\sigma_\mathbf{p})(\bar{p}_t^0-\sigma_\mathbf{p})(q_t^0-\sigma_\mathbf{q})(\bar{q}_t^0-\sigma_\mathbf{q})}\\ &\quad +\ldots+(\text{regular part})\end{aligned} \tag{A.10}$$

with

$$\chi_P(p) = \frac{r_1'(\mathbf{p})}{p_t^0-\sigma_\mathbf{p}} + \frac{r_2'(\mathbf{p})}{\bar{p}_t^0-\sigma_\mathbf{p}} + (\text{regular part}), \tag{A.11}$$

$$\bar{\chi}_P(q) = \frac{\bar{r}_1'(\mathbf{q})}{q_t^0-\sigma_\mathbf{q}} + \frac{\bar{r}_2'(\mathbf{q})}{\bar{q}_t^0-\sigma_\mathbf{q}} + (\text{regular part}), \tag{A.12}$$

so that each term in (A.6) and (A.7) contributes to the analytic structure of the S-matrix element given in Step 1 as follows:

$$V_{it}\cdot\mathcal{G}\cdot V_{tf}^c \;\to\; R_4,\, C \tag{A.13}$$

$$V_{it}\cdot\mathcal{G}\cdot V_{tf}^d \;\to\; R_1\sim R_6,\, C \tag{A.14}$$

$$C_{if} \;\to\; R_5,\, R_6,\, C \tag{A.15}$$

Since there appear three different pole structures, the decomposition of the amplitude is quite cumbersome. We will demonstrate how to determine the components (pole positions, etc.) regarding only the P^0-dependence of the amplitude *à la* Stuart [29]. The inclusion of the remaining structures is straightforward though. Let us decompose the 4-point function as

$$\mathcal{G}(p,q,P) = \frac{r}{P^0-\omega} + D(P^0), \tag{A.16}$$

where $D(P^0)$ is regular as $P^0\to\omega$, and substituting this to eq. (A.6), we obtain

$$S_{fi} = V_{it}(P^0)\cdot\frac{r}{P^0-\omega}\cdot V_{tf}(P^0) + V_{it}(P^0)\cdot D(P^0)\cdot V_{tf}(P^0) + C_{if}(P^0) \tag{A.17}$$

$$\begin{aligned}&= \frac{V_{it}(\omega)\cdot r\cdot V_{tf}(\omega)}{P^0-\omega}\\ &\quad + [V_{it}\cdot r\cdot V_{tf}]^R(P^0) + V_{it}(P^0)\cdot D(P^0)\cdot V_{tf}(P^0) + C_{if}(P^0)\end{aligned} \tag{A.18}$$

with

$$[V_{it}\cdot r\cdot V_{tf}]^R(P^0) = \frac{V_{it}(P^0)\cdot r\cdot V_{tf}(P^0) - V_{it}(\omega)\cdot r\cdot V_{tf}(\omega)}{P^0-\omega}. \tag{A.19}$$

Thus, if the perturbative expansion of $\omega, r, V_{it}(P^0), V_{tf}(P^0)$, and $D(P^0)$ are known, it is possible to make the systematic perturbative expansion of the pole position, the residue, and the non-resonant background.

Step 3

As seen in Step 2, the only non-trivial perturbative expansion of the necessary ingredient is that of the full 4-point function $\mathcal{G}(p,q,P)$, which includes the s-channel resonance poles near threshold. We will demonstrate the perturbative expansion of $\mathcal{G}(p,q,P)$ by applying the Bethe-Salpeter formalism to the case with finite resonance widths.

The 4-point function satisfies the celebrated Bethe-Salpeter equation

$$\begin{aligned}\mathcal{G}(p,p',P) &= S_F(P/2+p)\,S_F(-P/2+p)\,(2\pi)^4\delta^4(p-p')\\ &\quad + \int \tfrac{d^4q}{(2\pi)^4}\,S_F(P/2+p)\,S_F(-P/2+p)\,K(p,q,P)\,\mathcal{G}(q,p',P),\end{aligned} \tag{A.20}$$

where S_F denotes the full top quark propagator. Bethe-Salpeter kernel K is the sum of all 2PI graphs of $\mathcal{G}$ with external legs amputated. (Figs. A.3(a)(b))

[5] Formal derivation of eq. (A.10) in the narrow width limit is given in Ref.[44]. Eqs. (A.11) and (A.12) follow straightforwardly from the definition of Bethe-Salpeter wave functions therein.

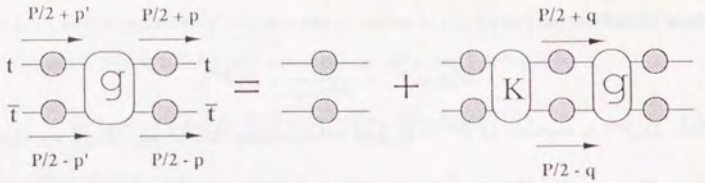

(a)

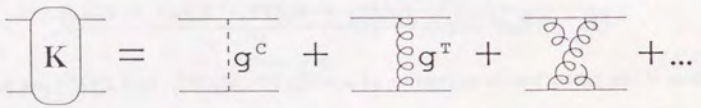

(b)

Figure A.3: (a) A diagrammatical representation of the Bethe-Salpeter equation. (b) Diagrams for the Bethe-Salpeter kernel K.

The leading order 4-point function $\mathcal{G}^0$ is obtained as the sum of leading threshold singularities, $\sum c_n(\alpha_s/\beta)^n$, by taking only the leading term on both sides of eq. (A.20) and solving it. Namely, we replace

$$S_F(p_t) \;\to\; S^0 = \frac{1+\gamma^0}{2}\frac{i}{p_t^0 - \sigma_{\mathbf{p}}^0}, \tag{A.21}$$

$$S_F(-\bar{p}_t) \;\to\; \bar{S}^0 = \frac{1-\gamma^0}{2}\frac{i}{\bar{p}_t^0 - \sigma_{\mathbf{p}}^0}, \tag{A.22}$$

$$K(p,q,P) \;\to\; K^0 = C_F \cdot 4\pi\alpha_s \cdot \gamma^0 \frac{-i}{|\mathbf{p}-\mathbf{q}|^2}\gamma^0, \tag{A.23}$$

in (A.20), to obtain[6]

$$\mathcal{G}^0(p,q,P) = \mathcal{G}_a^0(p,q,P) + \mathcal{G}_b^0(p,q,P), \tag{A.25}$$

with

$$\mathcal{G}_a^0 = \left(\frac{1+\gamma^0}{2} \otimes \frac{1-\gamma^0}{2}\right) i\, B^0(p,P)\, \tilde{G}^0(\mathbf{p},\mathbf{q};E)\, B^0(q,P), \tag{A.26}$$

$$\mathcal{G}_b^0 = \left(\frac{1+\gamma^0}{2} \otimes \frac{1-\gamma^0}{2}\right) \frac{1}{p_t^0 - \sigma_{\mathbf{p}}^0}\frac{1}{\bar{p}_t^0 - \sigma_{\mathbf{p}}^0} \times[-(2\pi)^4\delta^4(p-q) + i(2\pi)^3\delta^3(\mathbf{p}-\mathbf{q})B^0(q,P)]. \tag{A.27}$$

Here,

$$\sigma_{\mathbf{p}}^0 = m_t + \mathbf{p}^2/2m_t - i\Gamma_t^0/2, \tag{A.28}$$

and

$$B^0(p,P) = \frac{1}{p_t^0 - \sigma_{\mathbf{p}}^0} + \frac{1}{\bar{p}_t^0 - \sigma_{\mathbf{p}}^0}. \tag{A.29}$$

We have identified α_s^2 and α_W as the same order quantities in (A.28), and Γ_t^0 denotes the top quark decay width in the lowest order. (Eq. (3.2.7)) $B^0(p,P)$ describes the

[6]This solution may be obtained in the following manner[25]. First consider the equation satisfied by

$$\int \tfrac{dp^n}{(2\pi)}\tfrac{dq^n}{(2\pi)}\,\mathcal{G}^0(p,q,P), \tag{A.24}$$

then it is easy to see that this is just the Green's function of the Schrödinger equation, $\tilde{G}^0(\mathbf{p},\mathbf{q};E)$, multiplied by the trivial spinor structure. One may reconstruct $\mathcal{G}^0(p,q,P)$ by expressing it as the sum of the product of free propagators, the one-gluon-exchange term, and the two-and-more-gluon-exchange term, the last term of which contains eq. (A.24).

propagation of t or $\bar{t}$ after the decay of its counterpart. The resonance state vanishes on the instant of the decay of either t or $\bar{t}$, and the remaining particle propagates as a one-particle state[13]. The product of the free propagators is contained in $\mathcal{G}_b^0$.

At the heart of the leading 4-point function $\mathcal{G}^0$ is the Green's function $\tilde{G}^0(\mathbf{p},\mathbf{q};E)$ of the non-relativistic Schrödinger equation with Coulombic potential:

$$\tilde{G}^0(\mathbf{p},\mathbf{q};E) = \langle \mathbf{p} \,|\, \frac{-1}{E-\hat{H}+i\Gamma_t^0} \,|\, \mathbf{q} \rangle\,, \tag{A.30}$$

$$\hat{H} = \frac{\hat{\mathbf{p}}^2}{m_t} - C_F\frac{\alpha_s}{\hat{r}}. \tag{A.31}$$

Thus, it can be expressed using the Coulomb wave functions $\phi_n(\mathbf{p})$'s as

$$\tilde{G}^0(\mathbf{p},\mathbf{q};E) = -\sum_n \frac{\phi_n(\mathbf{p})\phi_n^*(\mathbf{q})}{E-E_n+i\Gamma_t^0}, \tag{A.32}$$

where n include the continuum states.

The perturbative expansion[7] of the full 4-point function $\mathcal{G}(p,q,P)$ can be expressed using the leading 4-point function $\mathcal{G}^0(p,q,P)$ as[25,43]

$$\mathcal{G} = \mathcal{G}^0 + \mathcal{G}^0\cdot\Delta K\cdot\mathcal{G}^0 + \mathcal{G}^0\cdot\Delta K\cdot\mathcal{G}^0\cdot\Delta K\cdot\mathcal{G}^0 + \ldots \tag{A.33}$$

with

$$\Delta K = (K-K^0) - [S_F^{-1}S_{\bar{F}}^{-1} - (S^0)^{-1}(\bar{S}^0)^{-1}]. \tag{A.34}$$

For a moment, we neglect $\mathcal{G}_b^0$ in (A.25) and set $\mathcal{G}^0 = \mathcal{G}_a^0$. Then we may write

$$\mathcal{G}^0(p,q,P) = i\sum_n \frac{\chi_n^0(p,P)\bar{\chi}_n^0(q,P)}{E-E_n+i\Gamma_t^0}. \tag{A.35}$$

with the wave functions defined by

$$\chi_{n\lambda}^0(p,P) = iB^0(p,P)\phi_n(\mathbf{p})\times|\,\lambda\,\rangle\,, \tag{A.36}$$

$$\bar{\chi}_{n\lambda}^0(q,P) = iB^0(q,P)\phi_n^*(\mathbf{p})\times\langle\,\lambda\,|\,. \tag{A.37}$$

[7]The expansion presented here is incomplete as $\mathcal{G}^0$ includes the projection operator $\left(\frac{1+\gamma^0}{2}\otimes\frac{1-\gamma^0}{2}\right)$. Indeed, residual term with other spinor structure is necessary on the right-hand-side of eq. (A.33), but it is neglected here. Later, when we determine $tt\gamma$-vertex up to $O(\alpha_s)$ correction, the contribution from the residual term will be estimated trivially. (See subsection 3.2.b and Appendix B.) Incidentally, the effect of $[S_F^{-1}S_{\bar{F}}^{-1} - (S^0)^{-1}(\bar{S}^0)^{-1}]$ in ΔK amounts to including the $O(\alpha_s)$ correction to the top decay width Γ_t.

Here, $|\,\lambda\,\rangle = (1,0,0,0)^T\otimes(0,0,1,0)^T$, etc. are the spinor basis satisfying

$$\sum_\lambda |\,\lambda\,\rangle\langle\,\lambda\,| = \frac{1+\gamma^0}{2}\otimes\frac{1-\gamma^0}{2}. \tag{A.38}$$

Substituting this form into eq. (A.33) and making an appropriate resummation, we obtain the 4-point function including the next-to-leading order corrections as

$$\mathcal{G}^1(p,q,P) = i\sum_n \frac{\chi_n^1(p,P)\bar{\chi}_n^1(q,P)}{E-E_n^1+i\Gamma_t^1}, \tag{A.39}$$

where

$$E_n^1(E) - i\Gamma_t^1 = E_n - i\Gamma_t^0 + i\bar{\chi}_n^0\cdot\Delta K\cdot\chi_n^0, \tag{A.40}$$

$$\chi_n^1(p,P) = \chi_n^0(p,P) + i\sum_{m\neq n}\frac{\chi_m^0\bar{\chi}_m^0\cdot\Delta K\cdot\chi_n^0}{E-E_m+i\Gamma_t^1}, \tag{A.41}$$

$$\bar{\chi}_n^1(q,P) = \bar{\chi}_n^0(q,P) + i\sum_{m\neq n}\frac{\bar{\chi}_n^0\cdot\Delta K\cdot\chi_m^0\bar{\chi}_m^0}{E-E_m+i\Gamma_t^1}, \tag{A.42}$$

with Γ_t^1 being the top qurak width including $O(\alpha_s)$ correction, eq. (3.2.6), and replacing $\Gamma_t^0\to\Gamma_t^1$ everywhere in χ_n^0 and $\bar{\chi}_n^0$.

At this stage one may proceed as we did in Step 2; separate the pole part and the regular part of $\mathcal{G}^1(p,q,P)$, make the perturbative expansion of the pole position,[8] the residue, and the non-resonant background. Then we may return to Step 2 and determine all the components of S-matrix element up to $O(\alpha_s)$. It is straightforward to extend the method to higher orders. This is how the perturbation should be performed in principle. For example, because the Coulomb wave function $\phi_n(\mathbf{p})$ contained in the leading wave function χ_n^0 is a function of $|\mathbf{p}|/\alpha_s$, it is easy to see that the shift of

[8]As stressed by Stuart [29], the pole positions of the resonances are directly related to the parameters of the fundamental theory. The defining equation of the pole positions of $\mathcal{G}$ is obtained formally by inverting eq. (A.33):

$$(\mathcal{G}^0)^{-1} - \Delta K = 0. \tag{A.43}$$

What should be compared with this in the case of Z^0 resonance pole is

$$(D^0)^{-1} - \Pi_{ZZ} = 0, \tag{A.44}$$

where Π_{ZZ} is the Z^0 self-energy, and $D^0 = 1/(s-m_Z^2)$ is the zeroth order Z^0 propagator. For example, the gauge invariance of the pole positions of QED bound states is shown in Ref.[25].

resonance pole $i\bar{\chi}^0_n \cdot \Delta K \cdot \chi^0_n(E_n)$ becomes the $O(\alpha_s)$ correction to the leading pole position E_n by identifying ΔK with the $O(\alpha_s)$ or $O(\beta)$ correction to the leading kernel K^0; see Appendix B.

Unfortunately, it becomes outrageously difficult to invoke this prescription when the multi-resonance structure is involved. Therefore we should adopt an alternative, more practical approach, which correctly includes all the corrections up to the desired order, but give up the elimination of higher order contributions as attained by splitting the pole part and regular part of $\tilde{G}^0(\mathrm{p},\mathrm{q};E)$ [29].

From eq. (A.39) and the definitions of χ^0_n and $\bar{\chi}^0_n$, it is clear that the next-to-leading order 4-point function $\mathcal{G}^1(p,q,P)$ can be expressed using the Green's function of Schrödinger equation which does *not* depend on the relative time variables, p^0 and q^0:

$$\mathcal{G}^1(p,q,P) = \left(\frac{1+\gamma^0}{2} \otimes \frac{1-\gamma^0}{2}\right) i\, B^1(p,P)\, \tilde{G}^1(\mathrm{p},\mathrm{q};E)\, B^1(q,P) \tag{A.45}$$

with

$$\tilde{G}^1(\mathrm{p},\mathrm{q};E)_{\lambda\lambda'} = \langle \mathrm{p},\lambda \,|\, \frac{-1}{E-\hat{H}-\Delta\hat{V}+i\Gamma^1_t} \,|\, \mathrm{q},\lambda' \rangle\,, \tag{A.46}$$

$$B^1(p,P) = \frac{1}{p^0_t - \sigma^1_{\mathrm{p}}} + \frac{1}{\bar{p}^0_t - \sigma^1_{\mathrm{p}}}, \tag{A.47}$$

and

$$\sigma^1_{\mathrm{p}} = m_t + \mathrm{p}^2/2m_t - i\Gamma^1_t/2. \tag{A.48}$$

Here, the perturbative potential ΔV is energy- and spin-dependent,[9] in general, and given in terms of ΔK as

$$\Delta V(\mathrm{p},\mathrm{q};E) = \left(\frac{1+\gamma^0}{2} \otimes \frac{1-\gamma^0}{2}\right) \times \int \tfrac{dp^0}{(2\pi)} \tfrac{dq^0}{(2\pi)} [-iB^1(p,P)\Delta K(p,q,P)B^1(q,P)] \left(\frac{1+\gamma^0}{2} \otimes \frac{1-\gamma^0}{2}\right). \tag{A.49}$$

[9]The explicit calculation shows, however, that ΔV is energy- and spin-independent at $O(\alpha_s)$. See Subsection 3.2.d.

It is possible to find the graphs of ΔK that contributes to the $O(\alpha_s)$ correction by the power counting method as described in Appendix B.

Now we include $\mathcal{G}^0_b$ and see how $\mathcal{G}^1$ changes. As $\mathcal{G}^0_b$ has no s-channel pole, we find

$$\mathcal{G}^1 = (1+\mathcal{G}^1_b \cdot \Delta K)\cdot \mathcal{G}^1_a \cdot (1+\Delta K \cdot \mathcal{G}^1_b) + \mathcal{G}^1_b + \mathcal{G}^1_b \cdot \Delta K \cdot \mathcal{G}^1_b, \tag{A.50}$$

with

$$\mathcal{G}^1_a(p,q,P) = \left(\frac{1+\gamma^0}{2} \otimes \frac{1-\gamma^0}{2}\right) i\, B^1(p,P)\, \tilde{G}^1(\mathrm{p},\mathrm{q};E)\, B^1(q,P). \tag{A.51}$$

$$\mathcal{G}^1_b(p,q,P) = \left(\frac{1+\gamma^0}{2} \otimes \frac{1-\gamma^0}{2}\right) \frac{1}{p^0_t - \sigma^1_{\mathrm{p}}} \frac{1}{\bar{p}^0_t - \sigma^1_{\mathrm{p}}} \times [-(2\pi)^4\delta^4(p-q) + i(2\pi)^3\delta^3(\mathrm{p}-\mathrm{q})B^1(q,P)]. \tag{A.52}$$

Again, the dots in (A.50) represent the loop integrations of the $t\bar{t}$ relative momenta, contraction of spinor indices, etc. The 4-point function $\mathcal{G}^1(p,q,P)$ obtained in this manner includes all contributions up to $O(\alpha_s)$ with the spinor structure $\left(\frac{1+\gamma^0}{2} \otimes \frac{1-\gamma^0}{2}\right)$. Then we return to step 2, and insert $\mathcal{G}^1(p,q,P)$ into eq. (A.6). The S-matrix will be obtained, which includes all $O(\alpha_s)$ corrections correctly by construction. The result can be found in Subsection 3.2.c.

One may find the instructions of the renormalization prescription in the bound state problems in Ref.[43].

Appendix B

Power Counting Method

We demonstrate the power counting method of the diagrams for the process $e^+e^- \to t\bar{t} \to bW^+\bar{b}W^-$. This is presented in the context of two specific problems concerned in the calculation of $O(\alpha_s)$ corrections:

(1) Determination of the spinor structure of the $t\bar{t}V$ vector vertex Λ_V^k, and,

(2) Identification of the diagrams which contribute to the Bethe-Salpeter kernel at $O(\alpha_s)$.

We will first explain the power counting method applied to the diagrams for $e^+e^- \to t\bar{t} \to bW^+\bar{b}W^-$ in step (0). Then using the result, we will work out the above problems (1) and (2). The conclusions to be drawn are

(1) The $t\bar{t}V$ vector vertex has the spinor structure

$$\Lambda_V^k \propto (\not{p}_t + m_t)\gamma^k(-\not{\bar{p}}_t + m_t) + O(\beta^2), \tag{B.1}$$

and

(2) The diagrams which contribute to the Bethe-Salpeter kernel are shown in Figs. B.7, B.8 and B.9.

We fix the gauge to the Coulomb gauge throughout this appendix.

(0) Power Counting of Diagrams

Let us first neglect the decay of top quark and develop the power counting of the diagrams for the process $\gamma^* \to t\bar{t}$. (Fig. B.1)

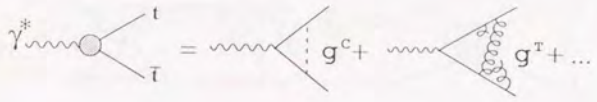

Figure B.1: Diagrams for $\gamma^* \to t\bar{t}$, neglecting the decay of top quark. Dashed line represents the Coulomb gluon, and the curly line is for the transverse gluon.

(0-1) Leading Threshold Singularities

We show by power counting that a diagram for the process $\gamma^* \to t\bar{t}$ has the behavior $\sim \alpha_s^n/\beta^m$ with

$$m = n - V_3 - 2V_4 \tag{B.2}$$

near $t\bar{t}$ threshold. Here, V_3 and V_4, respectively, represent the number of the 3-point and 4-point gluon self-vertices contained in the diagram. The power counting has been performed under the following three conditions:

(A) The kinematical configuration is constrained to the specific non-relativistic region,

$$p_t^0 - m,\ \bar{p}_t^0 - m \sim O(\beta^2), \qquad \mathbf{p}_t = -\bar{\mathbf{p}}_t \sim O(\beta), \tag{B.3}$$

$$k^0 \sim O(\beta^2), \qquad \mathbf{k} \sim O(\beta), \tag{B.4}$$

where, p_t, $\bar{p}_t$ and k represent the internal momenta of t, $\bar{t}$ and the gluon, respectively, in the c.m. frame.

(B) The diagrams with internal fermion loops are ignored, and only those with internal gluons and $t\bar{t}$ lines connected to the external lines are considered. (Quenched diagrams)

(C) The diagrams with ghosts are ignored.

We note that the singularities will be suppressed for the diagrams including transverse gluons (g^T), and in eq. (B.2), m decreases by two for the each transverse gluon contained in the diagram. This is because the couplings of g^T to the top quark and to other gluons are suppressed by β.

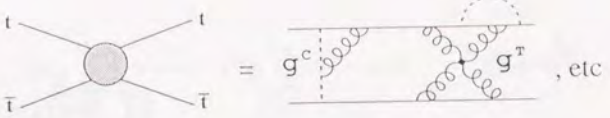

Figure B.2: An example of the diagram for $t\bar{t} \to t\bar{t}$, neglecting the decay of top quark.

[Explanation of Eq. (B.2)]

As the singularities $\sim (1/\beta)^m$ stem from the non-relativistic region of the loop momenta, we perform the power counting in this region. The gluon 3-point self-coupling is proportional to the gluon momenta, so that it is accompanied by β. The gluon 4-point self-vertex appears in the loop with less number of internal lines, so the number of singularities from the propagators gets reduced. Here, we have not considered the power counting of $\log\beta$'s.

[Proof of Eq. (B.2)]

For the kinematical configurations given by (B.3) and (B.4), $t(\bar{t})$ and gluon propagators are counted as $\sim 1/\beta^2$, and the measure for the each loop integration $d^4k/(2\pi)^4$ as $\sim \beta^5$. Let us consider any $O(\alpha_s^n)$ diagram for the process $t\bar{t} \to t\bar{t}$. (Fig. B.2) Then n is given by

$$n = \frac{1}{2}V_3 + V_4 + \frac{1}{2}v_3, \tag{B.5}$$

where v_3 denotes the number of $t\bar{t}g$ vertices contained in the diagram. Meanwhile, the number of the loop integrations (the number of independent momenta) L is given by

$$L = I - V_3 - V_4 - v_3 + 1, \tag{B.6}$$

where I represents the number of the internal lines (propagators). Then the power of $1/\beta$ of the diagram is expressed as

$$m' = 2I - 5L - V_3, \tag{B.7}$$

and using the relation

$$2I + 4 = 3V_3 + 4V_4 + 3v_3, \tag{B.8}$$

we obtain

$$m' = n + 1 - V_3 - 2V_4. \tag{B.9}$$

Therefore, the behavior $\sim \alpha_s^n/\beta^m$ of the diagram for $\gamma^* \to t\bar{t}$ is given by

$$m = n - V_3 - 2V_4 \tag{B.10}$$

if the phase space factor $\propto \beta$ is taken into account.

[Leading Singularities]

According to eq. (B.2), the leading singularities ($m = n$) reside in the diagrams with only Coulomb gluons where $V_3 = V_4 = 0$. One can show[25] that, among these diagrams, the additional suppression factor β^2 is associated with those diagrams where $t(\bar{t})$ has to propagate backward in time when the each Coulomb propagator is identified as connecting the points at equal time, for each of such $t(\bar{t})$ propagator. This is because the contribution to the loop integral comes from the negative energy pole of the $t(\bar{t})$ propagator:

$$\frac{1}{\beta^2 m_t^2} \to \frac{1}{m_t^2}. \tag{B.11}$$

Therefore, we may conclude that the leading threshold singularities reside only in the uncrossed ladder diagrams[1]; see Figs. B.3(a)(b).

(0-2) Relaxing the Conditions (A)-(C)

We examine how the power counting will change if we remove the conditions (A)-(C) in the above argument.

(A') It would be formidable to extend the argument to the general kinematical configurations. Here, we examine an example which seems to exhibit the most singular power

[1]This can be shown in other gauges as well[33].

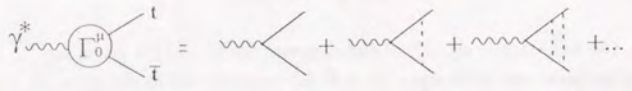

(a)

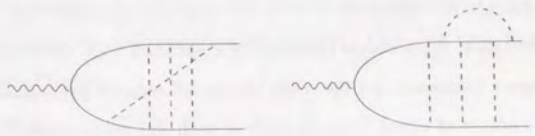

(b)

Figure B.3: (a) The uncrossed ladder diagrams with Coulomb gluons, which exhibit the leading threshold singularities. (b) The diagrams which are composed of only $t\bar{t}$ and Coulomb gluons, but which are associated with additional suppression factors.

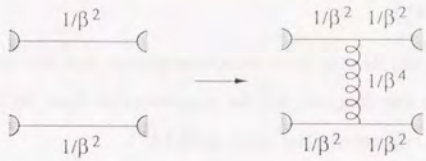

Figure B.4: Diagrams representing the attachment of a gluon propagator (Coulomb or transverse), with k^0, $\mathrm{k} \sim O(\beta^2)$, to any two internal lines of a diagram considered in (0-1). The powers of β show the singularities of the propagators in the diagram.

count other than the above kinematical region, considering that the $1/\beta$ singularities stem from the non-relativistic regime of the loop integrations. Let us take a diagram considered in (0-1) for the kinematical configurations given by (B.3) and (B.4). Suppose we attach a gluon propagator with momentum,

$$k^0 \sim O(\beta^2) \quad \text{and} \quad \mathrm{k} \sim O(\beta^2), \tag{B.12}$$

to any two internal lines of this diagram, see Fig. B.4. In this case, there appear three additional propagators as compared to the original diagram, and the power count of the new propagators will be $\sim 1/\beta^2, 1/\beta^2$, and $1/\beta^4$. The integration measure for the new loop integral will be $\sim \beta^8$. As a result, the power count of the diagram becomes $O(\alpha_s)$ as compared to the original one.

(A") On the other hand, if one considers the loop integrations over the relativistic region of any diagram, these are not accompanied by the enhancement factor $1/\beta$.

(B') How does the power count change if there are internal fermion loops? First, if there is a top loop, the diagram will be suppressed by β^2 on account of the energy conservation. Secondly, consider a diagram with loops of light fermions. In the non-relativistic region, one should replace the gluon propagators with the fermion propagators, $\not{p}^{-1}$, in the discussion given in (0-1). Hence, the diagram will be suppressed at least by β^2 as it includes two or more fermion propagators. The contribution from the relativistic regions

are the same as in (A").

(C') The ghost fields couple only with transverse gluons, and the coupling is proportional to the momenta. So the diagram will be suppressed at least by β^2. The contribution from the relativistic regions are the same as in (A").

(0-3) $O(\alpha_s)$ Corrections

We may conclude that the $O(\alpha_s)$ corrections to the leading singularities, α_s^{n+1}/β^n, stem solely from the relativistic corrections to the vertices and the propagators of the leading diagrams (uncrossed Coulomb ladders) as long as the decay of top quark is neglected. This can be seen as follows. According to the discussion developed so far, there are two possibilities for the $O(\alpha_s)$ corrections from other sources. One is the case $V_3 = 1$ in eq. (B.2). However, since there is no gluon 3-point self-vertex with only Coulomb gluons, transverse gluons will always be involved, and hence it becomes the $O(\alpha_s^2)$ correction. The other possibility is the contribution from the non-relativistic configuration of the gluon discussed in (0-2), (A'). Again the transverse gluon is accompanied by the additional suppression factors, while the effect of Coulomb gluon for this kinematical configuration is already incorporated in the uncrossed ladder diagrams.

(0-4) Inclusion of the Decay of Top Quark

Now we include the decay of top quark. A new feature as compared to the non-decay diagrams is that gluons can be attached to the b-quark. In this case, the coupling of the transverse gluon to b-quark is *not* suppressed by β. Also, if the soft gluon with momentum k is attached to b-quark, the b propagator behaves as $\sim 1/k$.

We have examined the diagrams and the kinematical configurations for the process $\gamma^* \to t\bar{t} \to bW^+\bar{b}W^-$ which give rise to the $O(\alpha_s)$ corrections to the leading singularities other than those considered above. We find the diagrams shown in Fig. B.5 for those which give contributions from the non-relativistic region. Γ_0^μ represents the sum of uncrossed Coulomb ladder diagrams. There are two relevant kinematical regions of the

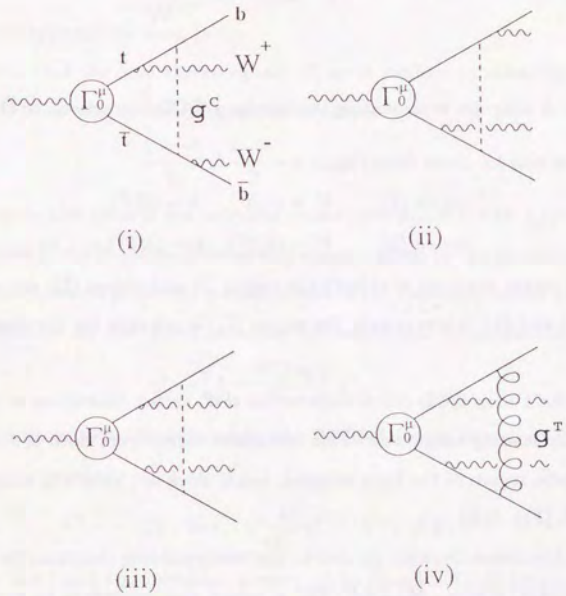

Figure B.5: Diagrams relevant to the decay of top quark, which contribute to the $O(\alpha_s)$ corrections to the leading singularities for $e^+e^- \to bW^+\bar{b}W^-$. These are the diagrams which give contribution from the non-relativistic regime.

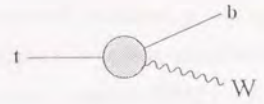

Figure B.6: A diagram representing the one-loop QCD corrections to the tbW vertex.

gluon momentum for these diagrams,

$$\begin{aligned} &\text{region (I)} \quad : \quad k^0 \sim O(\beta^2), \quad \mathbf{k} \sim O(\beta), \\ &\text{region (II)} \quad : \quad k^0 \sim O(\beta^2), \quad \mathbf{k} \sim O(\beta^2). \end{aligned} \tag{B.13}$$

One sees by power counting that both the region (I) and region (II) are relevant for the diagrams (i) and (ii), whereas only the region (II) is relevant for the diagrams (iii) and (iv).

Also, the 1-loop QCD corrections to the tbW vertex contribute to the $O(\alpha_s)$ correction to the leading amplitude. This correction stems from both the non-relativistic and relativistic region of the loop integral, but it does not have any enhancement near $t\bar{t}$ threshold. (Fig. B.6)

These two corrections are related to the corresponding diagrams for the real gluon emission process, $e^+e^- \to t\bar{t} \to bW^+\bar{b}W^-g$, which also contribute to the $O(\alpha_s)$ corrections to the $t\bar{t}$ cross section.

(1) Spinor Structure of Λ_V^k

Here we show that the spinor structure of the $t\bar{t}V$ vector vertex including the $O(\alpha_s)$ corrections is given by

$$\Lambda_V^k \propto (\not{p}_t + m_t)\gamma^k(-\not{p}_t + m_t) + O(\beta^2), \tag{B.14}$$

in two steps.[2] The definition of Λ_V^k can be found in Subsection 3.2.b.

[2]We neglect the effect of the one-insertion of the non-instantaneous kernel, which gives an additional contribution to the spinor structure of Λ_V^k. Namely we are concerned only with the first term in eq. (3.2.13).

(1-1) Amputated $t\bar{t}V$ Vector Vertex

We first show that the amputated $t\bar{t}V$ vector vertex Γ^k has the spinor sturcuture

$$\Gamma^k = \gamma^k + \left(\frac{1+\gamma^0}{2}\gamma^k\frac{1-\gamma^0}{2}\right) f + O(\beta^2), \tag{B.15}$$

where f is some appropriate form factor.

It is trivial that the tree vertex equals γ^k, so it suffices to show that the 1-loop and higher loop diagrams all have the spinor structure

$$\frac{1+\gamma^0}{2}\gamma^k\frac{1-\gamma^0}{2} + O(\beta^2). \tag{B.16}$$

According to the general perturbation framework presented in Appendix A, the amputated vertex Γ^k up to the next-to-leading order is given by the sum of "ladder-like" diagrams. Namely, we make certain modifications to the Coulomb ladder diagram. The $t\bar{t}\gamma$ vertex is replaced by the vertex including the relativistic correction[34]:

$$\gamma^k \to \left(1 - \frac{2C_F\alpha_s}{\pi}\right)\gamma^k. \tag{B.17}$$

The Coulomb propagators are replaced by the Bethe-Salpeter kernel up to $O(\alpha_s)$ (see step (2) of this Appendix):

$$K^0 = -iC_F \cdot 4\pi\alpha_s \cdot \gamma^0\frac{1}{|\mathbf{k}|^2}\gamma^0 \to K^0 + \Delta K. \tag{B.18}$$

We should use the t and $\bar{t}$ propagators correct up to $O(\alpha_s) = O(\beta)$ for connecting the above pieces:

$$S_F(P/2+p) \quad \to \quad \left(\frac{1+\gamma^0}{2} - \frac{p^k\gamma^k}{2m_t}\right)\cdot\frac{i}{E/2 + p^0 - \mathbf{p}^2/2m_t + i\Gamma_t} \tag{B.19}$$

$$S_F(-P/2+p) \quad \to \quad \left(\frac{1-\gamma^0}{2} - \frac{p^k\gamma^k}{2m_t}\right)\cdot\frac{i}{E/2 - p^0 - \mathbf{p}^2/2m_t + i\Gamma_t} \tag{B.20}$$

As we will see in step (2) of this Appendix, the Bethe-Salpeter kernel $K + \Delta K$ is spin-independent in the subspace represented by $\left(\frac{1+\gamma^0}{2} \otimes \frac{1-\gamma^0}{2}\right)$, after the appropriate time integral introduced in the course of perturbative expansion.

One may notice that the vertex Γ^k would have the spinor structures other than those given in (B.16) at $O(\beta)$ if the $p^k\gamma^k$ terms of the above propagators give contributions. Considering that the term $p^k\gamma^k/2m_t$ is $O(\beta)$ in itself, all other components of the

diagram should contribute at the leading order form. Writing the term $p^k\gamma^k/2m_t$ with the spinor structures of the vertices and the propagators on both sides, we find

$$\frac{1+\gamma^0}{2}\gamma^0\frac{p^k\gamma^k}{2m_t}\gamma^0\frac{1+\gamma^0}{2}=0, \quad \text{etc.}\ , \tag{B.21}$$

so that this term cannot give contribution to the spinor structure of Γ^k.

(1-2) $t\bar{t}V$ **Vector Vertex**

Note the spinor structure,

$$\frac{\not{p}_t+m_t}{2m_t}\left(\frac{1+\gamma^0}{2}\gamma^k\frac{1-\gamma^0}{2}\right)\frac{-\not{p}_t+m_t}{2m_t}=\frac{\not{p}_t+m_t}{2m_t}\gamma^k\frac{-\not{p}_t+m_t}{2m_t}+O(\beta^2). \tag{B.22}$$

Then by attaching the propagators to the amputated vertex Γ^k, one finds

$$\Lambda_V^k\propto(\not{p}_t+m_t)\gamma^k(-\not{p}_t+m_t)+O(\beta^2), \tag{B.23}$$

for the spinor structure of the $t\bar{t}V$ vector vertex.

(2) Bethe-Salpeter Kernel at $O(\alpha_s)$

The leading order Bethe-Salpeter kernel is given by the Coulomb propagator

$$K^0=-iC_F\cdot 4\pi\alpha_s\cdot\gamma^0\frac{1}{|\mathrm{k}|^2}\gamma^0, \tag{B.24}$$

as it is the very part which contributes to the leading threshold singularities. Here, we will find the diagrams which contribute to the Bethe-Salpeter kernel at $O(\alpha_s)$ $(=\Delta K)$.

First consider the spinor structure of ΔK. As it is already an $O(\alpha_s)$ quantity itself, the contributions from the $t(\bar{t})$ propagators which connect the kernels come only from their leading structures. Therefore, it suffices to consider the spinor structures of the kernel ΔK which survive when sandwitched by $\left(\frac{1+\gamma^0}{2}\otimes\frac{1-\gamma^0}{2}\right)$ on both sides.

In the case when only the QCD interaction is taken into account, those diagrams that contribute to ΔK are the hard corrections[3] to the Coulomb propagator and the $t\bar{t}g^c$ vertices according to the discussion in (0-3). These are shown in Fig. B.7. The

[3]The correction factor which stems from the relativistic region of the loop integration, which is not accompanied by the singularity $1/\beta$.

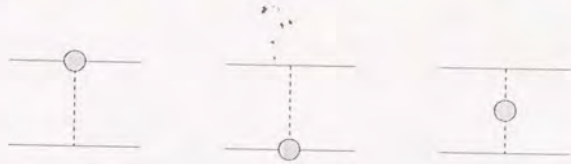

Figure B.7: Diagrams representing the one-loop hard QCD corrections to the leading Bethe-Salpeter kernel.

QCD potential at 1-loop level has been calculated[35,36], which corresponds to

$$\begin{aligned}\Delta K_{QCD} &= -iC_F\cdot 4\pi\alpha_s\cdot\gamma^0\frac{1}{|\mathrm{k}|^2}\gamma^0 \\ &\quad\times\frac{\alpha_s}{4\pi}\left[C_A\left\{\tfrac{11}{3}\log\left(\tfrac{\mu^2}{k^2}\right)+\tfrac{31}{9}\right\}-n_f\left\{\tfrac{2}{3}\log\left(\tfrac{\mu^2}{k^2}\right)+\tfrac{10}{9}\right\}\right]\end{aligned} \tag{B.25}$$

in terms of α_s defined in the $\overline{\mathrm{MS}}$ scheme.[4] Here, n_f denotes the number of light quarks probed by the $t\bar{t}$ system.

Taking into account of the electroweak interaction, it is expected from the discussion in (0-4) that the absorptive part of the diagrams shown in Figs. B.8 and B.9 contribute to the absorptive part of the kernel ΔK_{abs}. Here, the Class (a) diagrams represent the $O(\alpha_s)$ corrections to the absorptive part of the top quark self-energy, that is, the $O(\alpha_s)$ corrections to the top quark width. The diagrams belonging to Class (b) represent the absorptive part of the 1-loop electroweak corrections to the $t\bar{t}g^c$ vertex.

We are led to calculate the absorptive potential ΔV_{abs} corresponding to these diagrams according to the framework given in Appendix A:

$$\begin{aligned}\Delta V_{abs} &= \left(\frac{1+\gamma^0}{2}\otimes\frac{1-\gamma^0}{2}\right) \\ &\quad\times\int\tfrac{dp^0}{(2\pi)}\tfrac{dq^0}{(2\pi)}[-iB(p,P)\Delta K_{abs}(p,q,P)B(q,P)]\left(\frac{1+\gamma^0}{2}\otimes\frac{1-\gamma^0}{2}\right) \qquad \text{(B.26)} \\ &= -i\,\Delta\Gamma_t\,\delta^3(\mathrm{p}-\mathrm{q})\left(\frac{1+\gamma^0}{2}\otimes\frac{1-\gamma^0}{2}\right) \qquad \text{(B.27)}\end{aligned}$$

It turns out that only the contributions from Class (a) diagrams survive, which amount

[4]See, however, the discussion in Section 6.2.

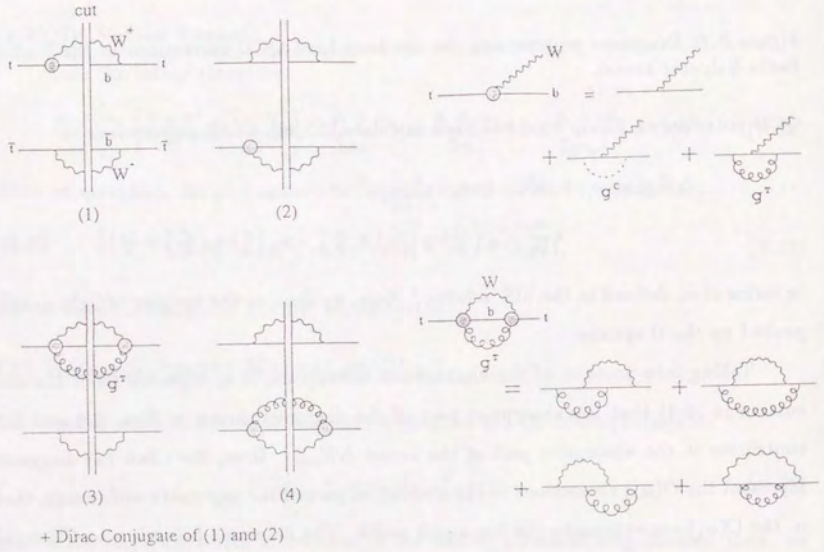

Figure B.8: Class (a) diagrams of the cut-diagrams that contribute to the absorptive kernel ΔK_{abs} up to the next-to-leading order.

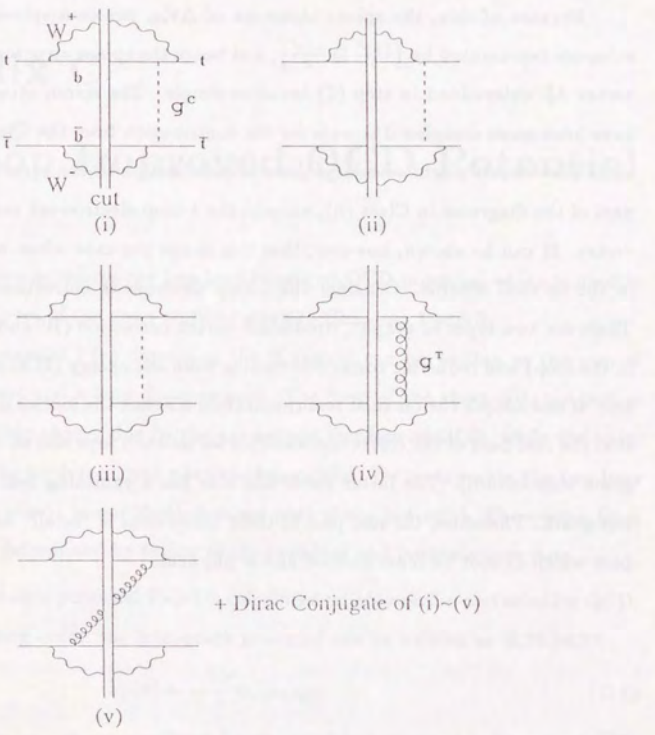

Figure B.9: Class (b) diagrams of the cut-diagrams that contribute to the absorptive kernel ΔK_{abs} at the next-to-leading order.

to $O(\alpha_s)$ correction to the top width ($= \Delta\Gamma_t$), while those from the Class (b) diagrams vanish altogether; see subsection 3.2.d.

Because of this, the spinor structure of ΔV_{ab_s} becomes spin-independent in the subspace represented by $\left(\frac{1+\gamma^0}{2} \otimes \frac{1-\gamma^0}{2}\right)$, and hence the spinor structure of the $t\bar{t}V$ vector vertex Λ_V^k determined in step (1) becomes simple. The spinor structure of Λ_V^k would have been more complex if it were for the contribution from the Class (b) diagrams.

The readers might wonder if there is contribution to the kernel ΔK from the real part of the diagrams in Class (b), namely, the 1-loop electroweak corrections to the $t\bar{t}g$ vertex. It can be shown, however, that this is not the case when we renormalize ΔK in the on-shell scheme. Consider the 1-loop electroweak correction to the $t\bar{t}g$ vertex. There are two types of graphs, irreducible vertex correction (W and two b propagators in the loop) and reducible correction coming from self-energy (Wb) insertion on the top line. If one adopts the on-shell renormalization scheme, the former is renormalized such that the real part of the correction vanishes for on-shell tops and at $k^2 \to 0$ (k being the gluon momentum). The latter correction also has a vanishing real part for a on-shell top quark. Therefore, the real part of these corrections is "small" unlike the imaginary part which cannot be renormalized and is physical.

Appendix C

Two-Loop Improved QCD Potential

In this appendix, we introduce the two-loop improved QCD potential which is used in the numerical analyses of the cross sections given in Chapters 4 and 5.

The QCD potential $V(r)$ describing the $t\bar{t}$ system can be written as the sum of a short-distance part and a long-distance part. The form of the short-distance part is given by perturbation theory due to the asymptotic freedom of QCD, while the long-distance part has to be determined phenomenologically. We incorporate the two-loop perturbative QCD effects in our short-distance part of the potential. The overall form of the potential is determined by fitting to charmonium and bottomonium data.

The short-distance potential $V_P(r)$ is calculated reliably in the perturbative QCD. In the next-to-leading order, the interquark potential can be written as [6,35,36,37]

$$V_P(r) = -\frac{C_F}{r}\alpha_s(\mu_1)_{\overline{\rm MS}} \tag{C.1}$$

where the coupling, α_s, is renormalized by the modified minimal subtraction ($\overline{\rm MS}$) scheme and where we have made a choice of the renormalization scale [45]

$$\mu_1 = \frac{1}{r}\exp\left(-\frac{A(r)}{b_0}\right) \tag{C.2}$$

with

$$b_0 = \frac{11}{6}C_A - \frac{2}{3}n_f T_F, \tag{C.3}$$

$$A(r) = b_0\gamma_E + \frac{31}{37}C_A + \frac{2}{3}T_F\sum_{q=1}^{n_f}[\gamma_E + \log(m_q r) - {\rm Ei}(-e^{5/6}m_q r)]. \tag{C.4}$$

Here $\gamma_E = 0.5772...$ is Euler's constant; $T_F = 1/2$, $C_F = 4/3$ and $C_A = 3$ are color factors; n_f is the number of quark flavors and $\mathrm{Ei}(-x)$ is the exponential integral

$$\mathrm{Ei}(-x) = -\int_x^\infty \frac{dt}{t} e^{-t}, \tag{C.5}$$

which parametrizes accurately the quark mass dependence of the perturbative potential [37]. In the massless quark limit, the next-to-leading order correction factor $A(r)$ reduces to the well-known result [36,7]

$$A(r) \to b_0\gamma_E + \frac{31}{37}C_A - \frac{5}{9}n_f T_F \quad (\text{as } m_q r \to 0). \tag{C.6}$$

It should be stressed, however, that the charm and bottom quark masses cannot be neglected at distances

$$r m_q \sim 1. \tag{C.7}$$

The running coupling constant $\alpha_s(\mu)$ is fixed by the μ-independent QCD scale parameter

$$\Lambda_{\overline{\mathrm{MS}}}^{(n_f)} = \mu \exp\left\{-\frac{\pi}{b_0\alpha_s(\mu)} + \frac{b_1}{b_0^2}\log\left[\frac{2}{b_0}\left(\frac{\pi}{\alpha_s(\mu)} + \frac{b_1}{b_0}\right)\right]\right\} \tag{C.8}$$

with

$$b_1 = \frac{17}{12}C_A^2 - \frac{5}{6}C_A n_f T_F - \frac{1}{2}C_F n_f T_F, \tag{C.9}$$

which can easily be solved iteratively.

The contribution of a heavy top quark loop to the toponium potential can always be neglected due to the asymptotic freedom of QCD [46] and the decoupling theorem [47], because the top quark mass is much larger than the inverse of the toponium size of order $\alpha_s m_t$ for $\alpha_s \ll 1$. In the zero width approximation for toponium, the bottom quark loop contribution to the quarkonium potential can also be neglected for $m_t \lesssim 100$ GeV [20]. Therefore, the effective four flavor ($n_f = 4$) theory with $m_u = m_d = m_s = 0$ and $m_c = 1.5$ GeV (fixed) can give a good description of the short distance potential for a wide range of inter-quark distance ($r \gtrsim 1/m_b$). When the top quark is heavier and the decay width of the $t\bar{t}$ system is as high as a few GeV, the

short distance potential should be more accurately described by the effective five flavor ($n_f = 5$) theory. Thus, we fix $n_f = 5$ for the QCD potential and retain the charm and bottom quark finite masses. The next-to-leading order correction factor $A(r)$ in eq. (C.4) is then

$$A(r) = b_0\gamma_E + \frac{31}{37}C_A + \frac{2}{3}T_F\left[-\frac{5}{2} + \gamma_E + \log(m_c r) - \mathrm{Ei}(-e^{5/6}m_c r)\right.$$
$$\left. + \gamma_E + \log(m_b r) - \mathrm{Ei}(-e^{5/6}m_b r)\right] \tag{C.10}$$

which is obtained by setting $n_f = 5$ in b_0 and $m_u = m_d = m_s = 0$. We set $m_c = 1.5$ GeV and $m_b = 5$ GeV, whose values are fixed throughout the paper irrespective of the values of m_c and m_b that appear in the fitting of the charmonium and bottomonium data.

The μ-independent QCD scale parameter $\Lambda_{\overline{\mathrm{MS}}}^{(n_f)}$ for $n_f = 4$ and $n_f = 5$ theories are related through the matching condition [48]

$$\alpha_s^{(4)}(\mu = m_b)_{\overline{\mathrm{MS}}} = \alpha_s^{(5)}(\mu = m_b)_{\overline{\mathrm{MS}}}. \tag{C.11}$$

Since we work in the $n_f = 5$ theory, the perturbative QCD potential is completely determined once $\Lambda_{\overline{\mathrm{MS}}}^{(5)}$ is fixed. Since the definition of the $\Lambda_{\overline{\mathrm{MS}}}^{(n_f)}$ parameters are somewhat arbitrary,[1] we use the magnitude of the $\overline{\mathrm{MS}}$ coupling constant at $\mu = m_Z$ (=91.17 GeV), $\alpha_s(m_Z)_{\overline{\mathrm{MS}}}$, to parametrize the strength of the QCD interactions. The value of $\Lambda_{\overline{\mathrm{MS}}}^{(5)}$ in our definition is then obtained directly from eq. (C.8). The corresponding $\Lambda_{\overline{\mathrm{MS}}}^{(4)}$ value is obtained from the matching condition (C.11) at $m_b = 5$ GeV. The values of $\Lambda_{\overline{\mathrm{MS}}}^{(4)}$ and $\Lambda_{\overline{\mathrm{MS}}}^{(5)}$ for $\alpha_s(m_Z)_{\overline{\mathrm{MS}}} = 0.10$ to 0.14 are given in Table C.1.

While it is justified to neglect dynamical quark mass effects in the potential at small distances ($r m_q \ll 1$), they have to be taken into account at larger distances ($r m_q \sim 1$). In Fig. C.1, we show distributions of $-C_F/rV_P(r) = 1/\alpha_s(\mu_1)_{\overline{\mathrm{MS}}}$ as functions of r for the massive $n_f = 5$ theory and the corresponding $n_f = 5$ and $n_f = 4$ massless quark theories for $\alpha_s(m_Z)_{\overline{\mathrm{MS}}} = 0.10$ and 0.12. For $r \ll 1/m_b$, the effective $n_f = 5$ (solid lines)

[1] If we use the approximate expressions presented by the Particle Data Group [38], the values of $\Lambda_{\overline{\mathrm{MS}}}^{(n_f)}$ become as follows: $\Lambda_{\overline{\mathrm{MS}}}^{(5)} = (0.068, 0.140, 0.253, 0.416)$ GeV and $\Lambda_{\overline{\mathrm{MS}}}^{(4)} = (0.111, 0.212, 0.362, 0.565)$ GeV for $\alpha_s(m_Z)_{\overline{\mathrm{MS}}} = (0.10, 0.11, 0.12, 0.13)$, respectively. These values are about 6–7% larger than the values quoted in Table C.1.

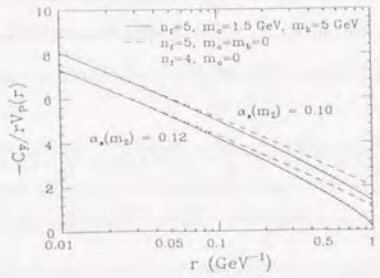

Figure C.1: $-C_F/rV_P(r) = 1/\alpha_s(\mu_1)_{\overline{\rm MS}}$ versus r. Solid lines are for $n_f = 5$, $m_u = m_d = m_s = 0$, $m_c = 1.5$ GeV, and $m_b = 5$ GeV; dashed (dotted) lines are for the $n_f = 5$ ($n_f = 4$) massless theory.

and the massless $n_f = 5$ (dashed lines) theories agree with each other perfectly, showing that quark mass effects can be neglected at those distances ($r \lesssim 0.05$ GeV^{-1}). At these short distances $r \lesssim 0.05$ GeV^{-1}, the $n_f = 4$ theory deviates appreciably from the $n_f = 5$ theory and hence the $n_f = 5$ theory should be used in this region. On the other hand, for $r \gtrsim 0.2$ GeV^{-1} where most of the interesting charmonium and bottomonium data are sensitive, the $n_f = 5$ massless theory ($m_c = m_b = 0$) is incorrect since there the finite charm and bottom quark masses are non-negligible. Thus, in order to describe as accurately as possible the short distance potential for a wide range of inter-quark distance, we adopt the effective $n_f = 5$ theory with finite charm and bottom quark masses.

At intermediate and long distances, non-perturbative effects of QCD become more important. The inter heavy quark potential in the region

$$0.5 \text{ GeV}^{-1} \lesssim r \lesssim 5 \text{ GeV}^{-1} \tag{C.12}$$

is known [7] to be constrained well by the charmonium and bottomonium data, which is roughly consistent with the logarithmic potential of Quigg and Rosner [8]. At long distances, the potential may rise linearly reflecting the quark confinement. We therefore

parametrize our phenomenological potential as follows:

$$\begin{aligned} V(r) &= V_P(r) && \text{at } r < r_0, \\ &= c_0 + c_1 \ln \tfrac{r}{r_0} e^{-r/r_1} + ar && \text{at } r > r_0. \end{aligned} \tag{C.13}$$

We require that the potential $V(r)$ and its first derivative $V'(r)$ be continuous at $r = r_0$:

$$c_0 = -ar_0 + V_P(r), \tag{C.14}$$

$$c_1 = e^{r_0/r_1}[-a + V_P'(r_0)]. \tag{C.15}$$

The above two conditions fix c_0 and c_1 in terms of the remaining three free parameters r_0, r_1 and a, for a given $\alpha_s(m_Z)_{\overline{\rm MS}}$ value. The derivative of the perturbative potential is given exactly by using the two-loop renormalization group equation as

$$\begin{aligned} V_P'(r) &= -\frac{V_P(r)}{r}\{1 - \frac{\alpha_s(\mu_1)_{\overline{\rm MS}}}{\pi} \\ &\quad \times [b_0 + b_1 \frac{\alpha_s(\mu_1)_{\overline{\rm MS}}}{\pi}](1 + \frac{2 - \exp(-e^{5/6} m_c r) - \exp(-e^{5/6} m_b r)}{3b_0})\}, \end{aligned} \tag{C.16}$$

where the scale $\mu_1(r)$ is given by eq. (C.2). It is worth noting here that the term multiplying the two-loop beta function factor $[b_0 + b_1 \frac{\alpha_s}{\pi}]$ is unity at short distances $m_c r$, $m_b r \ll 1$, whereas in the long distance limit $m_c r$, $m_b r \gg 1$, it reduces to the factor

$$\frac{b_0 + \frac{2}{3}}{b_0}. \tag{C.17}$$

This is nothing but the ratio of the coefficient (C.3) of the effective three flavor theory, $b_0(n_f = 3) = b_0(n_f = 5) + \frac{2}{3}$, and that of our effective five flavor theory, exhibiting the decoupling of heavy quarks at long distances.[2]

By varying the free parameters r_0, r_1 and a together with the constituent charm and bottom quark masses, m_c and m_b, this potential gives a good description of the properties of the bottomonium and charmonium data [38] for a range of fixed $\alpha_s(m_Z)_{\overline{\rm MS}}$ values. Note that the dynamical charm and bottom quark masses in the short distance

[2] In order to obtain the perturbative potential where the second coefficient b_1 also exhibits the decoupling of heavy quarks, we need to use the two-loop β function in the momentum subtraction scheme [49], which can only be solved numerically. We used the $\overline{\rm MS}$ coupling constant for convenience since the effect of the running of the coefficient b_1 has been found to be negligibly small [50].

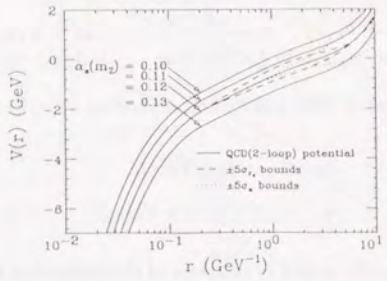

Figure C.2: The solid lines are our phenonenological QCD potential $V(r)$. The dashed (dotted) lines show the range of the potential accepted by the 5σ variation of the parameter r_0 (a) from its best fit value at $\alpha_s(m_Z)_{\overline{\rm MS}} = 0.12$.

part of the potential are fixed at $m_c = 1.5$ GeV and $m_b = 5$ GeV, respectively (see eq. (C.10)). The results of the χ^2 fit to data for a range of $\alpha_s(m_Z)_{\overline{\rm MS}}$ values are listed in Table C.1. The overall χ^2 is found to be very stable to changes in $\alpha_s(m_Z)_{\overline{\rm MS}}$ for the range $0.10 \lesssim \alpha_s(m_Z)_{\overline{\rm MS}} \lesssim 0.14$. In fact, because of the steady changes of parameters with respect to $\alpha_s(m_Z)_{\overline{\rm MS}}$, the parameters of the QCD potential can be very well parametrized by a polynomial in $\alpha_s(m_Z)_{\overline{\rm MS}}$ in this range. The fitted values of the constituent charm and bottom quark masses are slightly low at $\alpha_s(m_Z)_{\overline{\rm MS}} = 0.10$ while they are a little too large at $\alpha_s(m_Z)_{\overline{\rm MS}} = 0.14$. The mass difference $m_b - m_c$ is almost independent of $\alpha_s(m_Z)_{\overline{\rm MS}}$. We note here, however, that a relatively small value $\alpha_s(m_Z)_{\overline{\rm MS}} \sim 0.105$ is inferred from the recent studies of the charmonium and bottomonium spectra in Lattice QCD [39].

In Fig. C.2, we show by solid lines our resulting QCD motivated potential for $\alpha_s(m_Z)_{\overline{\rm MS}} = 0.10$, 0.11, 0.12 and 0.13. The optimal potential as obtained by our parametrization is found to be purely perturbative at $r \lesssim 0.2$ GeV^{-1} ($r_0 \sim 0.2$ GeV^{-1} in Table C.1), logarithmic in the region 0.3 GeV$^{-1} \lesssim r \lesssim 4$ GeV^{-1}, and starts linearly rising at longer distances. As anticipated [8,7], the slopes of the logarithmic parts are common ($c_1 = 0.875 \pm 0.010$) to all $\alpha_s(m_Z)_{\overline{\rm MS}}$. In order to show the degree of constraints

coming from the onium data, we show in Fig. C.2 by dashed and dotted lines the region allowed by the five standard deviation shifts of the parameters r_0 and a, respectively, from their best fit values that are listed in Table C.1. The one-sigma ranges obtained by the MINUIT program are

$$\begin{aligned} r_0 &= 0.235 \pm 0.010, \\ a &= 0.357 \pm 0.025, \end{aligned} \qquad \text{(C.18)}$$

for $\alpha_s(m_Z)_{\overline{\rm MS}} = 0.12$.

$\alpha_s(m_Z)_{\overline{\rm MS}}$	0.10	0.11	0.12	0.13	0.14
$\Lambda^{(5)}_{\overline{\rm MS}}$ (GeV)	0.064	0.131	0.237	0.390	0.598
$\Lambda^{(4)}_{\overline{\rm MS}}$ (GeV)	0.104	0.198	0.339	0.533	0.783
m_c (GeV)	1.105	1.298	1.550	1.898	2.375
m_b (GeV)	4.556	4.728	4.956	5.279	5.731
r_0 (GeV^{-1})	0.208	0.233	0.235	0.207	0.168
r_1 (GeV^{-1})	3.962	3.808	3.740	3.745	3.749
a (GeV^2)	0.359	0.354	0.357	0.373	0.401
χ^2	16.57	17.98	19.30	20.38	20.87

Table C.1

Parameters of the QCD motivated potential fitted to the charmonium and bottomonium data, together with the corresponding minimal χ^2. The $\Lambda^{(5)}_{\overline{\rm MS}}$ values are fixed by the definition (C.8) with $m_Z = 91.17$ GeV, and the corresponding $\Lambda^{(4)}_{\overline{\rm MS}}$ values are calculated by the matching condition (C.11) at $m_b = 5$ GeV. The remaining five parameters m_c, m_b, r_0, r_1 and a have been fitted to the data which are listed in Table C.2.

		QCD					
		0.11		0.12		0.13	
$\alpha_s(m_Z)_{\overline{\rm MS}}$			χ^2		χ^2		χ^2
$c\bar{c}$ data:							
$m(1S)$	3068±2	3068	0	3068	0	3068	0
$m(1P)-m(1S)$	457±10	429	8.1	425	10.2	423	11.7
Γ_2/Γ_1	0.432±0.06	0.496	1.2	0.472	0.5	0.448	0.1
$b\bar{b}$ data:							
$m(1S)$	9452±2.5	9452	0	9452	0	9452	0
$m(2S)-m(1S)$	567±3	569	0.7	570	0.8	570	1.0
$m(3S)-m(1S)$	900±2.5	902	0.9	902	0.9	902	0.8
$m(1P)-m(1S)$	448±2.5	447	0.3	447	0.3	447	0.3
$m(2P)-m(1S)$	809±6	796	4.5	797	4.3	797	4.2
Γ_2/Γ_1	0.439±0.03	0.397	1.9	0.399	1.8	0.399	1.8
Γ_3/Γ_1	0.328±0.03	0.307	0.5	0.307	0.5	0.306	0.5
$\chi^2_{\rm tot}$			18.0		19.3		20.4

Table C.2

The optimum fits to charmonium and bottomonium data for our two-loop improved QCD potential. The contribution of each data point to χ^2 and their sum are also given. Masses are given in the MeV units. The QCD motivated potential has the two-loop improved short distance behavior for a given value of $\alpha_s(m_Z)_{\overline{\rm MS}}$. The parameters of the fitted potentials are listed in Table C.1 and in the text. $\Gamma_{\rm n}$'s are the leptonic widths of the nS states. Only their ratios have been fitted because of the large perturbative QCD correction to the width. The mass difference $m(2S) - m(1S)$ for the charmonium has not been fitted since $m(2S)$ is affected by the mixsing to the $D\overline{D}$ channel.

Appendix D

Calculation of Absorptive Potential

We present an explicit calculation of the absorptive potential $V_{abs}(\mathrm{p},\mathrm{q};E)$ in this appendix. The contribution from the cut-diagram (iii) (See Fig. 3.8) to the absorptive potential is shown as an example.

The definition of the perturbative potential is given in eq. (A.49):

$$\Delta V(\mathrm{p},\mathrm{q};E) = \Big(\frac{1+\gamma^0}{2}\otimes\frac{1-\gamma^0}{2}\Big) \times\int\tfrac{dp^0}{(2\pi)}\tfrac{dq^0}{(2\pi)}[-iB(p,P)\Delta K(p,q,P)B(q,P)]\Big(\frac{1+\gamma^0}{2}\otimes\frac{1-\gamma^0}{2}\Big). \quad \text{(D.1)}$$

Here, $P=(2m_t+E,\mathbf{0})$ is the momentum of the center of gravity, and

$$B(p,P) = \frac{1}{E/2+p^0-\mathrm{p}^2/2m_t+i\Gamma_t}+\frac{1}{E/2-p^0-\mathrm{p}^2/2m_t+i\Gamma_t}. \quad \text{(D.2)}$$

We may use the Cutkosky relation to evaluate the contribution from cut-diagram (iii) to ΔK_{abs}:[1]

$$-2i\Delta V_3(\mathrm{p},\mathrm{q};E) = \int\tfrac{dp^0}{(2\pi)}\tfrac{dq^0}{(2\pi)}\sum_{spin,color}\int d\Phi_2(bW^+)d\Phi_2(\bar{b}W^-)\,B(p,P)B^*(q,P) \times\Big(\frac{1+\gamma^0}{2}\otimes\frac{1-\gamma^0}{2}\Big)(M_3N_3^\dagger)\Big(\frac{1+\gamma^0}{2}\otimes\frac{1-\gamma^0}{2}\Big), \quad \text{(D.3)}$$

where

$$M_3 = -\Big(\frac{g_W}{\sqrt{2}}\Big)^2\bar{u}(p_b)\,\not{\epsilon}_{W^+}(p_W)\frac{1-\gamma_5}{2}\otimes\not{\epsilon}_{W^-}(\bar{p}_W)\frac{1-\gamma_5}{2}v(\bar{p}_b), \quad \text{(D.4)}$$

[1] We have $B^*(q,P)$ instead of $B(q,P)$ in eq. (D.3) since the corresponding part of the diagram is on the right of the cut.

$$N_3 \simeq -i\left(\frac{g_W}{\sqrt{2}}\right)^2 g_s^2\,\bar{u}(p_b)\,\not{\epsilon}_{W^+}(p_W)\frac{1-\gamma_5}{2}\otimes\not{\epsilon}_{W^-}(\bar{p}_W)\frac{1-\gamma_5}{2}v(\bar{p}_b)$$
$$\times\frac{1}{(k^0-\mathrm{n}_b\cdot\mathrm{k}+i\epsilon)(k^0-\bar{\mathrm{n}}_b\cdot\mathrm{k}-i\epsilon)|\mathrm{k}|^2}. \tag{D.5}$$

Here, the unit vector in direction of b ($\bar{b}$) 3-momentum is denoted as n_b ($\bar{\mathrm{n}}_b$); $k=q-p$ is the gluon momentum; $d\Phi_2(bW^+)$ and $d\Phi_2(\bar{b}W^-)$ are the two-body phase space of bW^+ and $\bar{b}W^-$, respectively, fixing t and $\bar{t}$ momenta $p_b+p_W=P/2+p$ and $\bar{p}_b+\bar{p}_W=P/2-p$. On the right-hand-side of eq. (D.5), we replaced the b- and $\bar{b}$-propagators by the eikonal factors noting that the relevant kinematical region of the exchanged gluon momentum is

$$k^0,\quad \mathrm{k}\sim O(\alpha_s^2). \tag{D.6}$$

Taking the spin sum of b-quarks, eq. (D.3) reduces to

$$-2i\Delta V_3(\mathrm{p},\mathrm{q};E)$$
$$\simeq -iC_F\left(\frac{g_W}{\sqrt{2}}\right)^4 g_s^2\int\tfrac{dp^0}{(2\pi)}\tfrac{dq^0}{(2\pi)}\sum_{W\,spin}\int d\Phi_2(bW^+)d\Phi_2(\bar{b}W^-)\;B(p,P)B^*(q,P)$$
$$\times\left[\frac{1+\gamma^0}{2}\not{\epsilon}_{W^+}\frac{1-\gamma_5}{2}\not{p}_b\not{\epsilon}_{W^+}\frac{1-\gamma_5}{2}\frac{1+\gamma^0}{2}\right]\otimes\left[\frac{1-\gamma^0}{2}\not{\epsilon}_{W^-}\frac{1-\gamma_5}{2}\not{\bar{p}}_b\not{\epsilon}_{W^-}\frac{1-\gamma_5}{2}\frac{1-\gamma^0}{2}\right]$$
$$\times\frac{1}{(k^0-\mathrm{n}_b\cdot\mathrm{k}-i\epsilon)(k^0-\bar{\mathrm{n}}_b\cdot\mathrm{k}+i\epsilon)|\mathrm{k}|^2}. \tag{D.7}$$

for the color singlet $t\bar{t}$ pair. We keep only the part that contributes to the desired order. Namely, we should take only the leading part on the right-hand-side of eq. (D.7), since the final-state-interaction contribution is already an $O(\alpha_s)$ quantity compared to the leading threshold singularities.

The bW^+ and $\bar{b}W^-$ phase space in the $t\bar{t}$ *c.m. frame* can be expressed in the leading order as

$$d\Phi_2(bW^+) \simeq \frac{1-r}{32\pi^2}\,d\Omega_{\mathrm{n}_b}\Big|_{p_b^0=\frac{1-r}{2}m_t} \tag{D.8}$$
$$d\Phi_2(\bar{b}W^-) \simeq \frac{1-r}{32\pi^2}\,d\Omega_{\bar{\mathrm{n}}_b}\Big|_{\bar{p}_b^0=\frac{1-r}{2}m_t} \tag{D.9}$$

with $r=m_W^2/m_t^2$. These expressions coincide with the phase space in the bW^+ *and* $\bar{b}W^-$ *c.m. frame*, respectively, since the velocity of virtual t or $\bar{t}$ is small:

$$\frac{\mathrm{p}}{P^0/2\pm p^0}\sim O(\alpha_s). \tag{D.10}$$

We may take the spin sum of W polarization vectors, and in the leading order

$$\sum_{W^+\,spin}\not{\epsilon}_{W^+}\frac{1-\gamma_5}{2}\not{p}_b\not{\epsilon}_{W^+}\frac{1-\gamma_5}{2} \simeq \frac{(1-r)(1+2r)}{2r}m_t\left[\gamma^0+\kappa n_b^i\gamma^i\right]\frac{1-\gamma_5}{2} \tag{D.11}$$
$$\sum_{W^-\,spin}\not{\epsilon}_{W^-}\frac{1-\gamma_5}{2}\not{\bar{p}}_b\not{\epsilon}_{W^-}\frac{1-\gamma_5}{2} \simeq \frac{(1-r)(1+2r)}{2r}m_t\left[\gamma^0+\kappa\bar{n}_b^i\gamma^i\right]\frac{1-\gamma_5}{2} \tag{D.12}$$

with $\kappa=(1-2r)/(1+2r)$. Therefore, we have

$$-2i\Delta V_3(\mathrm{p},\mathrm{q};E)$$
$$\simeq -iC_F\left(\frac{g_W}{\sqrt{2}}\right)^4 g_s^2\left[\frac{(1-r)^2(1+2r)}{64\pi^2 r}m_t\right]^2\frac{1}{|\mathrm{k}|^2}\int\tfrac{dp^0}{(2\pi)}\tfrac{dq^0}{(2\pi)}\;B(p,P)B^*(q,P)$$
$$\times\int d\Omega_{\mathrm{n}_b}d\Omega_{\bar{\mathrm{n}}_b}\left[\frac{1+\gamma^0}{2}\left(\gamma^0+\kappa n_b^i\gamma^i\right)\frac{1+\gamma^0}{2}\right]\otimes\left[\frac{1-\gamma^0}{2}\left(\gamma^0+\kappa\bar{n}_b^j\gamma^j\right)\frac{1-\gamma^0}{2}\right]$$
$$\times\frac{1}{(k^0-\mathrm{n}_b\cdot\mathrm{k}-i\epsilon)(k^0-\bar{\mathrm{n}}_b\cdot\mathrm{k}+i\epsilon)}. \tag{D.13}$$

Next we perform the integration $\int\frac{dp^0}{(2\pi)}$, $\int\frac{dq^0}{(2\pi)}$, $\int d\Omega_{\mathrm{n}_b}$ and $\int d\Omega_{\bar{\mathrm{n}}_b}$. Let us define

$$\int\tfrac{dp^0}{(2\pi)}\tfrac{dq^0}{(2\pi)}\,B(p,P)B^*(q,P)\,\frac{1}{(k^0-\mathrm{n}_b\cdot\mathrm{k}-i\epsilon)(k^0-\bar{\mathrm{n}}_b\cdot\mathrm{k}+i\epsilon)}$$
$$=\frac{-1}{(\mathrm{n}_b-\bar{\mathrm{n}}_b)\cdot\mathrm{k}+i\epsilon}\left[\frac{1}{\mathrm{k}\cdot(\mathrm{p}+\mathrm{q})/2m_t-\bar{\mathrm{n}}_b\cdot\mathrm{k}+i\Gamma_t}+\frac{1}{\mathrm{k}\cdot(\mathrm{p}+\mathrm{q})/2m_t+\mathrm{n}_b\cdot\mathrm{k}+i\Gamma_t}\right]$$
$$\simeq\frac{-1}{(\mathrm{n}_b-\bar{\mathrm{n}}_b)\cdot\mathrm{k}+i\epsilon}\left(\frac{1}{-\bar{\mathrm{n}}_b\cdot\mathrm{k}+i\Gamma_t}+\frac{1}{\mathrm{n}_b\cdot\mathrm{k}+i\Gamma_t}\right) \tag{D.14}$$
$$\equiv\mathcal{F}(\mathrm{n}_b,\bar{\mathrm{n}}_b,\mathrm{k}). \tag{D.15}$$

Then one may readily check the following formulas:

$$\int d\Omega_{\mathrm{n}_b} d\Omega_{\bar{\mathrm{n}}_b} \mathcal{F}(\mathrm{n}_b, \bar{\mathrm{n}}_b, \mathrm{k}) = 2\lambda^{-1} \frac{(4\pi)^2}{|\mathrm{k}|^2} A_3, \tag{D.16}$$

$$\int d\Omega_{\mathrm{n}_b} d\Omega_{\bar{\mathrm{n}}_b} \mathrm{n}_b \mathcal{F}(\mathrm{n}_b, \bar{\mathrm{n}}_b, \mathrm{k}) = 2i\lambda^{-1} \frac{(4\pi)^2}{|\mathrm{k}|^2} \frac{\mathrm{k}}{|\mathrm{k}|} A_4, \tag{D.17}$$

$$\int d\Omega_{\mathrm{n}_b} d\Omega_{\bar{\mathrm{n}}_b} \bar{\mathrm{n}}_b \mathcal{F}(\mathrm{n}_b, \bar{\mathrm{n}}_b, \mathrm{k}) = -2i\lambda^{-1} \frac{(4\pi)^2}{|\mathrm{k}|^2} \frac{\mathrm{k}}{|\mathrm{k}|} A_4, \tag{D.18}$$

$$\int d\Omega_{\mathrm{n}_b} d\Omega_{\bar{\mathrm{n}}_b} \mathrm{n}_b \otimes \bar{\mathrm{n}}_b \mathcal{F}(\mathrm{n}_b, \bar{\mathrm{n}}_b, \mathrm{k}) = -2\lambda^{-1} \frac{(4\pi)^2}{|\mathrm{k}|^2} \frac{\mathrm{k} \otimes \mathrm{k}}{|\mathrm{k}|^2} A_5, \tag{D.19}$$

where

$$\begin{aligned} A_3 &= \frac{1}{2}\lambda \left[\pi \tan^{-1}\left(\frac{1}{\lambda}\right) - \int_0^1 dx \, \frac{x}{x^2+\lambda^2} \log\left(\frac{1+x}{1-x}\right) \right] \\ &= \frac{1}{2}\lambda \tan^{-1}\left(\frac{1}{\lambda}\right) \left[\pi - \tan^{-1}\left(\frac{1}{\lambda}\right) \right], \end{aligned} \tag{D.20}$$

$$A_4 = \frac{1}{2}\lambda \tan^{-1}\left(\frac{1}{\lambda}\right), \tag{D.21}$$

$$A_5 = -\frac{1}{2}\left[1 - \lambda \tan^{-1}\left(\frac{1}{\lambda}\right) \right] \left[\pi\lambda + 1 - \lambda \tan^{-1}\left(\frac{1}{\lambda}\right) \right], \tag{D.22}$$

and $\lambda = \Gamma_t/|\mathrm{k}|$. [2]

Using

$$\Gamma_t \simeq \left(\frac{g_W}{\sqrt{2}}\right)^2 \frac{(1+2r)(1-r)^2}{32\pi r} m_t, \tag{D.23}$$

we finally obtain

$$\begin{aligned} -2i\Delta V_3(\mathrm{p}, \mathrm{q}; E) \simeq\ & 2C_F \frac{4\pi\alpha_s}{|\mathrm{k}|^2} \frac{\Gamma_t}{|\mathrm{k}|} \times \left(\frac{1+\gamma^0}{2} \otimes \frac{1-\gamma^0}{2}\right) \Big[iA_3 (\mathbf{1} \otimes \mathbf{1}) \\ & + \kappa A_4 \left(\mathbf{1} \otimes \frac{k^i\gamma^i}{|\mathrm{k}|}\gamma_5 + \frac{k^i\gamma^i}{|\mathrm{k}|}\gamma_5 \otimes \mathbf{1} \right) + i\kappa^2 A_5 \left(\frac{k^i\gamma^i}{|\mathrm{k}|}\gamma_5 \otimes \frac{k^j\gamma^j}{|\mathrm{k}|}\gamma_5 \right) \Big] \left(\frac{1+\gamma^0}{2} \otimes \frac{1-\gamma^0}{2} \right). \end{aligned} \tag{D.24}$$

[2] Note that $A_4 \to \frac{1}{2}$ for $\epsilon \ll |\mathrm{k}| \ll \Gamma_t$, while $A_4 \to 0$ for $|\mathrm{k}| \ll \epsilon$, since $\mathcal{F}$ tends to pure real in eqs. (D.17) and (D.18). This fact is related to taking the principal value in the integral in the top quark momentum distribution, eq. (4.1.11).

References

[1] D. Kennedy and P. Langacker, *Phys. Rev. Lett.* **65**, 2967 (1990);
G. Altarelli, R. Barbieri, and S. Jadach, *Nucl. Phys.* **B369**, 3 (1992); *ibid*, **B376**, 444 (1992);
LEP Collaborations, *Phys. Lett.* **276B**, 247 (1992).

[2] V.S. Fadin and V.A. Khoze, *JETP Lett.* **46**, 525 (1987); *Sov. J. Nucl. Phys.* **48**, 309 (1988).

[3] K. Fujikawa, *Prog. Theor. Phys.* **61**, 1186 (1979).

[4] Y. Dokshitzer, V. Khoze, and S. Troyan, in *Perturbative Quantum Chromodynamics*, ed. A. Mueller (World Scientific, 1989).

[5] T. Appelquist and H. Politzer, *Phys. Rev. Lett.* **34**, 43 (1975); *Phys. Rev.* **D12**, 1404 (1975).

[6] F. Feinberg, *Phys. Rev. Lett.* **39**, 316 (1977); *Phys. Rev.* **D17**, 2659 (1978).

[7] W. Buchmüller, S.-H.H. Tye, *Phys. Rev.* **D24**, 132 (1981);
W. Buchmüller, G. Grunberg and S.-H.H. Tye, *Phys. Rev. Lett.* **45**, 103, 587(E) (1980).

[8] C. Quigg and J. L. Rosner, *Phys. Rep.* **56**, 167 (1979).

[9] W. Kwong, *Phys. Rev.* **D43**, 1488 (1991).

[10] M. Strassler and M. Peskin, *Phys. Rev.* **D43**, 1500 (1991).

[11] S. Komamiya, in *Research Directions for the Decade, Proceedings of the 1990 Summer Study on High Energy Physics*, Snowmass, Colorado, 1990, edited by E. Berger (World Scientific, Singapre, 1992), p.459.

[12] K. Fujii, *Proceedings of the 2nd Workshop on JLC* (1990), KEK Proceedings 91-10, p.271.

[13] Y. Sumino, K. Fujii, K. Hagiwara, H. Murayama, and C.-K. Ng, *Phys. Rev.* **D47**, 56 (1993).

[14] M. Jeżabek, J. Kühn, and T. Teubner, *Z. Phys.* **C56**, 653 (1992); see also Ref.[15].

[15] W. Bernreuther, et al., DESY 92-123A, 255 (1992) in e^+e^- *Collisions at 500 GeV: The Physics Potential, Part A.*

[16] H. Murayama and Y. Sumino, *Phys. Rev.* **D47**, 82 (1993).

[17] K. Fujii, in *Physics and Experiments with Linear Colliders*, Saariselka, Finland, 11991, edited by R. Orava, P. Elrola and M. Nordbey (World Scientifi, Singapore, 1992), vol. I, p. 203.

[18] K. Fujii, Talk presented at *the Workshop on Studies of Top Quarks at Colliding-Beam Facilities* (Madison, WI, 1992), KEK preprint, KEK-92-159 (1992).

[19] J. Schwinger, *"Particles, Sources, and Fields"*, Vol. 2 (Addison–Wesley, New York 1973), Chap. 5-4.

[20] K. Hagiwara, K. Kato, A. D. Martin and C.-K. Ng, *Nucl. Phys.* **B344**, 1 (1990).

[21] J.H. Kühn and P.M. Zerwas, *Phys. Rep.* **167**, 321 (1988).

[22] J.H. Kühn, *Acta Physica Austriaca Suppl.* **24**, 203 (1982).

[23] I. Bigi, Y. Dokshitzer, V. Khoze, J.H. Kühn and P.M. Zerwas, *Phys. Lett.* **B181**, 157 (1986).

[24] M. Braun, *Sov. Phys. JETP* **27**, 652 (1968)

[25] G. Bodwin and D. Yennie, *Phys. Rep.* **43**, 267 (1978).

[26] V. Fadin and Yakovlev, *Sov. J. Nucl. Phys.* **53**, 688 (1991).

[27] M. Veltman, *Physica* **29**, 186 (1963).

[28] E.C. Poggio, H.R. Quinn, and S. Weinberg, *Phys. Rev.* **D13**, 1958 (1976).

[29] R. Stuart, *Phys. Lett.* **B262**, 113 (1991).

[30] M. Jeżabek and J. Kühn, *Phys. Lett.* **B207**, 91 (1988); *Nucl. Phys.* **B320**, 20 (1989); *Nucl. Phys.* **B314**, 1 (1989).

[31] A. Czarnecki, M. Jeżabek and J. Kühn, *Nucl. Phys.* **B351**, 70 (1991).

[32] A. Czarnecki, *Phys. Lett.* **B252**, 467 (1990);

[33] S. Love, *Ann. Phys.* (N.Y.) **113**, 153 (1978).

[34] R. Barbieri, R. Gatto, R. Kögerler and Z. Kunszt, *Phys. Lett.* **57B**, 455 (1975); W. Buchmüller, S.-H.H. Tye, *Phys. Rev.* **D24**, 132 (1981); see also Ref.[9].

[35] T. Appelquist, M. Dine and I.J. Muzinich, *Phys. Lett.* **69B**, 231 (1977); W. Fischler, *Nucl. Phys.* **B129**, 157 (1977).

[36] A. Billoire, *Phys. Lett.* **92B**, 343 (1980).

[37] K. Hagiwara, S. Jacobs, M.G. Olsson and K.J. Miller, *Phys. Lett.* **130B**, 209 (1983).

[38] Review of Particle Properties, Particle Data Group, *Phys. Lett.* **B239**, 1 (1990).

[39] A. X. El-Khadra, G. Hockney, A. Kronfeld and P. Mackenzie, *Phys. Rev. Lett.* **69**, 729 (1992);
C. Davies, B. Thacker and P. Lepage, Cornell Univ. preprint (1992).

[40] V.S. Fadin and V.A. Khoze, *Yad. Fiz.* **54**, 1118 (1991).

[41] I.I. Bigi, V.S. Fadin and V. Khoze, *Nucl. Phys.* **B377**, 461 (1992);

[42] K. Fujii, T. Matsui, and Y. Sumino, in preparation.

[43] G. Adkins, *Ann. Phys.* (N.Y.) **146**, 78 (1983).

[44] D. Lurié, A. MacFarlane, and Y. Takahashi, *Phys. Rev.* **140B**, 1091 (1965).

[45] G. Grunberg, *Phys. Lett.* **95B**, 70 (1980).

[46] D. J. Gross and F. Wilczek, *Phys. Rev. Lett.* **30**, 1343 (1973);
H. D. Politzer, *ibid,* **30**, 1346 (1973).

[47] T. Appelquist and J. Carazzone, *Phys. Rev.* **D11**, 2856 (1975).

[48] S. Weinberg, *Phys. Lett.* **91B**, 51 (1980);
L. Hall, *Nucl. Phys.* **B178**, 75 (1981).

[49] T. Yoshino and K. Hagiwara, *Z. Phys.* **C24**, 185 (1984).

[50] K. Hagiwara, A. D. Martin and A. W. Peacock, *Z. Phys.* **C33**, 135 (1986).

[51] K. Melnikov and O. Yakovlev, Novosibirsk State University preprint.